SIMULATION, DESIGN, AND ANALYSIS OF THE HYBRID MAGNETIC ATTITUDE AND THERMAL CONTROL SYSTEMS FOR THE VIOLET NANOSATELLITE MISSION

by

Alexander Maurice Pietro DiTommaso

Bachelor of Science in Engineering (Mechanical Engineering, Mechatronics)
University of New Brunswick, 2019

A THESIS SUBMITTED IN PARTIAL FULFILLMENT OF THE REQUIREMENTS FOR THE DEGREE OF

Master of Science in Mechanical Engineering

In the Graduate Academic Unit of Mechanical Engineering

Supervisors:	Tiger Jeans, Ph.D., Mechanical Engineering
	Brent Petersen, Ph.D., Electrical and Computer Engineering
Examining Board:	Mohsen Mohammadi, Ph.D., Mechanical Engineering
	Andy Simoneau, Ph.D., Mechanical Engineering
	Richard Langley, Ph.D., Geodesy and Geomatics Engineering

This thesis is accepted by the
Dean of Graduate Studies

THE UNIVERSITY OF NEW BRUNSWICK

November, 2021

Abstract

Due to the accelerating growth of the nanosatellite industry, there is a gap to fill for more innovative, cost-effective attitude and thermal control solutions. Passive Magnetic Attitude Control (PMAC) systems are capable of aligning a spacecraft within ten degrees of the local geomagnetic field vector and have minimal mechanical complexity. The VIOLET CubeSat (2U), requires a solution with more pointing options due to the area of the ionosphere to be imaged by the Spectral Airglow Structure Imager (SASI) payload. A novel and cost-effective solution has been developed, named the Hybrid Magnetic Attitude Control (HMAC) system. This system utilizes PMAC components with the addition of five air-core magnetic torque coils aligned with the body-fixed axes of the nanosatellite. The attitude dynamics of VIOLET are simulated by the Smart Nanosatellite Attitude Propogator (SNAP) Simulink® tool box, which all relevant environmental and orbital conditions are considered. VIOLET is unique in the fact that it is a 2U, dual payload nanosatellite with an unusually high thermal output of its communications system. The small form factor coupled with high thermal output is a critical problem to solve to achieve mission success. Siemens NX Space Systems Thermal is being utilized to create a Finite Element Model (FEA) to properly model the thermal behavior of the nanosatellite for both Worst Case Hot (WCH) and Worst Case Cold (WCC) scenarios. The design of the Thermal Control System (TCS) progressed concurrently with the analyses to define heat paths throughout VIOLET, to ensure sub-system components will not exceed their acceptable temperature ranges.

Table of Contents

List of Tables

List of Figures

Abbreviations

ACS Attitude Control System

ADCS Attitude Determination and Control System

AIT Assembly Integration and Testing

CCP Canadian CubeSat Project

CSA Canadian Space Agency

CSSWE Colorado Student Space Weather Experiment

DCM Direction Cosine Matrix

DoF degree of freedom

EAOP EGSE ADCS OBC Prototype

ECEF Earth Centered Earth Fixed

ECI Earth Centered Inertial

EGSE Electrical Ground Support Equipment

EM Engineering Model

EPS Electrical Power System

FDM finite difference method

FEA Finite Element Analysis

FEM Finite Element Model

FM Flight Model

FVM finite volume method

GFV Geomagnetic Field Vector

GMST Greenwich Mean Sidereal Time

GNSS Global Navigation Satellite System

GRIPS GNSS Receiver for Ionospheric and Position Studies

HMAC Hybrid Magnetic Attitude Control

HQP highly qualified personnel

IGRF International Geomagnetic Reference Field

IR infrared

ISS International Space Station

LEO Low Earth Orbit

LGVI Lie Group Variational Integrator

LMB Linear Microwave Board

MEKF Multiplicative Extended Kalman Filter

NOAA National Oceanic and Atmospheric Administration

NRCSD NanoRacks CubeSat Deployer

OBC On Board Computer

PCB printed circuit board

PMAC Passive Magnetic Attitude Control

RFD request for deviation

RMS root mean square

SASI Spectral Airglow Structure Imager

SASI-C Spectral Airglow Structure Imager Controller

SASI-O Spectral Airglow Structure Imager Optics

SCP SDR Communications Platform

SDR Software Defined Radio

SFL Space Flight Laboratory

SNAP Smart Nanosatellite Attitude Propagator

SRP Solar Radiation Pressure

TCS Thermal Control System

TGP time in good pointing

TLE Two Line Element

TRXVU Very High Frequency Ultra High Frequency Transceiver

TVAC Thermal Vacuum

UHF Ultra High Frequency

UNB University of New Brunswick

USAF United States Air Force

VHF Very High Frequency

WCC Worst Case Cold

WCH Worst Case Hot

WMM2020 World Magnetic Model 2020

ZTB Z Torquer Board

Nomenclature

The following symbols described are related to the design and analysis of the Attitude Control System (ACS) and TCS, all of which will be referenced throughout this document.

X - Scalar $\vec{X}$ - Vector

$\hat{X}$ - Unit vector $\mathbb{X}$ - Matrix

ACS Parameters and Calculated Values

$\vec{B}$	Geomagnetic Field Vector, (Tesla)
β	Beta angle, (deg)
Z_R	Body-fixed roll/imaging axis
Y_P	Body-fixed pitch axis
X_Y	Body-fixed yaw axis
ρ	Atmospheric fluid density, (kg/m^3)
C_D	Drag coefficient of a 2U CubeSat
A_{proj}	Projected windward surface area of VIOLET, (m^2)
$\hat{u}_v$	Unit velocity vector
$\hat{s}_{cp}$	Vector from center of pressure to center of mass

μ Earth's standard gravitational parameter, (m^3/s^2)

R Average radius of Earth, (m)

$\hat{u}_e$ Unit vector pointing from VIOLET's center of mass to Nadir

H_o Earth's magnetic dipole strength, (A$\cdot m^2$)

$\hat{u}_m$ Unit vector aligned with Earth's magnetic dipole

$\hat{u}_x$ Unit position vector at location of magnetic field calculation

$\vec{B}_{hys}$ Magnetic flux of hysteresis material, (Tesla)

$\vec{H}$ Magnetizing field of Earth at local GFV, (A/m)

μ_0 Permeability of space, (N/A^2)

T_{RMS} RMS of all environmental disturbance torques at flight altitude, (N$\cdot m^2$)

B_{min} Minimum magnetic flux at flight altitude, (Tesla)

β_{max} Desired average angle from body-fixed roll axis to local GFV, (deg)

$\vec{m}_{hys}$ Magnetic dipole of hysteresis material, (A$\cdot m^2$)

m_{min} Minimum magnetic moment, ($A \cdot m^2$)

B_{max} Maximum allowable magnetic field strength, (Gauss)

ACS Simulation Inputs

$\vec{m}'$ Resulting magnetic dipole from HMAC actuation, ($A \cdot m^2$)

m_{sat} Mass of Satellite, (kg)

$\mathbb{J}_{rpy}$ Mass Moment Inertia Matrix, (kg$\cdot m^2$)

$\vec{m}$ PMAC magnetic moment, ($A \cdot m^2$)

$\cancel{V}_{hys}$ Volume of hysteresis material, (cm^2)

H_c Ferromagnetic Coercivity, (A/m)

B_r Ferromagnetic Resistivity, (Tesla)

B_s Ferromagnetic Saturation, (Tesla)

t_{sim} Simulation duration, (hours)

$e_{\delta i}$ Acceptable inclination error, (deg)

ACS Simulation Outputs

$\vec{\omega}_0$ Initial rotation rates, (deg/s)

$\vec{M}_{gg}$ Gravity gradient torque, (N$\cdot m$)

$\vec{M}_{hys}$ Magnetic hysteresis torque, (N$\cdot m$)

$\vec{M}_{mag}$ Magnetic moment torque, (N$\cdot m$)

$\vec{M}_{aero}$ Aerodynamic torque, (N$\cdot m$)

$\vec{M}_T$ Total torque, (N$\cdot m$)

$\vec{X}_{ECI}$ ECI orbital position, (m)

$\dot{\vec{X}}_{ECI}$ ECI orbital velocity, (m/s)

$\ddot{\vec{X}}_{ECI}$ ECI orbital acceleration, (m/s^2)

$\vec{\omega}$ Rotational rates, (deg/s)

$\phi_{1,2,3}$ Body-fixed Euler angles, (deg)

$\theta_{R,P,Y}$ Body-fixed axes to GFV, (deg)

t_{ss} HMAC settling time, (hours)

δ_{img} Imaging inclination, (deg)

e_δ Inclination error, (deg)

e_β Beta angle error, (deg)

β_A Actual beta angle, (deg)

$t_{gp,n}$ Time in good pointing at latitude range, (sec)

t_{pd} Post-deployment settling time, (hours)

TCS Parameters and Calculated Values

$R_{ts,n}$ Thermal resistance of n^{th} tie rod/spacer joint, (K/W)

$R_{h,n}$ Thermal resistance of n^{th} PC104 header joint, (K/W)

$R_{ps,n}$ Thermal resistance of n^{th} solar panel to structure joint, (K/W)

$R_{sc,n}$ Thermal resistance of n^{th} surface contact joint, (K/W)

TCS Simulation Inputs

h Altitude, (km)

T_0 Initial (steady state) temperature, ($^\circ C$)

t_f Simulation duration, (hours)

N_t Number of time steps

N_R Number of results

α_{albedo} Earth albedo coefficient

ϕ_{IR} Infrared flux, (W/mm^2)

ϕ_{sol} Solar flux, (W/mm^2)

P_{ss} Power state of component or sub-system, (Watts)

ε_n Emissivity of n^{th} surface

α_n Absorptivity of n^{th} surface

TCS Simulation Outputs

T_{ss} Temperature of component or sub-system, ($^{\circ}C$)

Chapter 1

Introduction

1.1 Canadian CubeSat Project

The Canadian CubeSat Project (CCP), announced in April 2017, provides students in post-secondary institutions with an opportunity to take part in the design, analysis, and integration of systems for a real space mission. Through this national initiative, selected teams of students and mentoring professors are offered the unique opportunity to design and build a CubeSat [1]. The over-arching goal of this project is to educate and train the next generation of highly qualified personnel (HQP) for the Canadian space sector. In May 2018, the Canadian Space Agency (CSA) announced the selection of the winning proposals and awarded a total of 15 grants. Overall, 37 organizations are participating in the CCP, thanks to several interregional, interprovincial and international collaborations that include universities from Europe, Australia and the USA. Student teams across Canada are now hard at work to design and build their CubeSats [1]. Once tested and ready for space, the CubeSats will be launched to and deployed from the International Space Station (ISS) during two separate launches. The student teams will then operate their satellites and conduct science according to the objectives of their missions, which range from 3 to 24 months in duration.

1.2 VIOLET

Space Weather Exploration Mission

CubeSatNB is an innovative partnership between the New Brunswick Community College, the Université de Moncton, and the University of New Brunswick. The CubeSat, named VIOLET, is planned for deployment from the ISS, at an altitude of approximately 400 km, by on-board astronauts in 2022. VIOLET has two scientific payloads: GNSS Receiver for Ionospheric and Position Studies (GRIPS), and the Spectral Airglow Structure Imager (SASI). Both payloads will be studying Earth's ionosphere to give scientific insight into how space weather affects orbital and terrestrial communications signals. The VIOLET CubeSat, with labelled sub-systems, is shown in Figure 1.1.

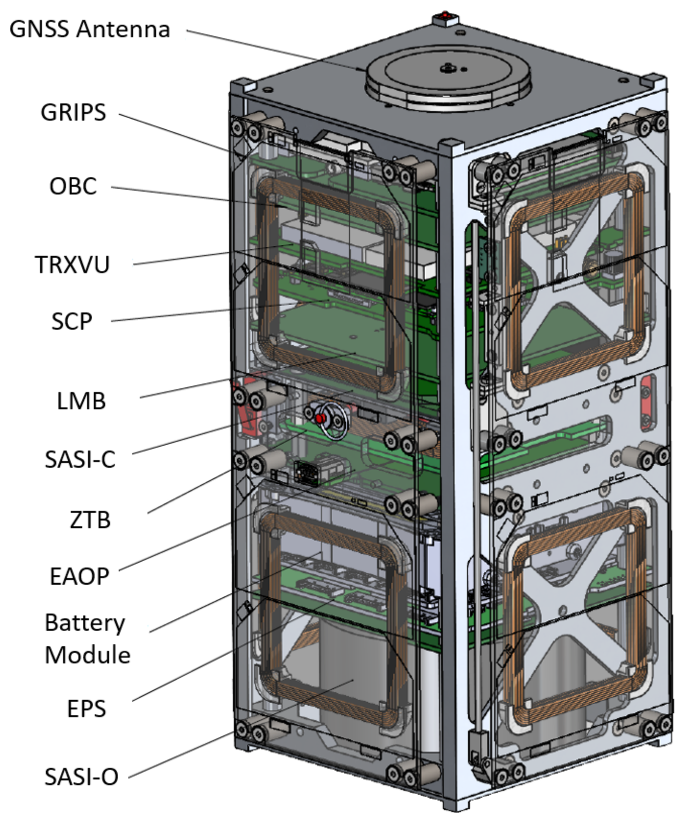

Figure 1.1: VIOLET model with labelled sub-system components.

1.3 The Hybrid Magnetic Attitude Control System

For the VIOLET mission, the Attitude Control System (ACS) main purpose is to enable the SASI payload, a spectral imager, to image the ionosphere across a latitude range of ±52° with the SASI imaging axis pointed -12° from tangent to the Earth's surface. This attitude cannot be achieved across the mentioned latitude range using a Passive Magnetic Attitude Control (PMAC) system alone, however it can meet basic mission requirements and is an excellent redundancy for the Hybrid Magnetic Attitude Control (HMAC) system. This is due to the passive nature of the PMAC system, it will have adequate attitude for imaging only at magnetic field inclinations of -12°±5°, primarily near the equator. A map of the Earth's magnetic inclinations at 400 km altitude is shown in figure 1.2.

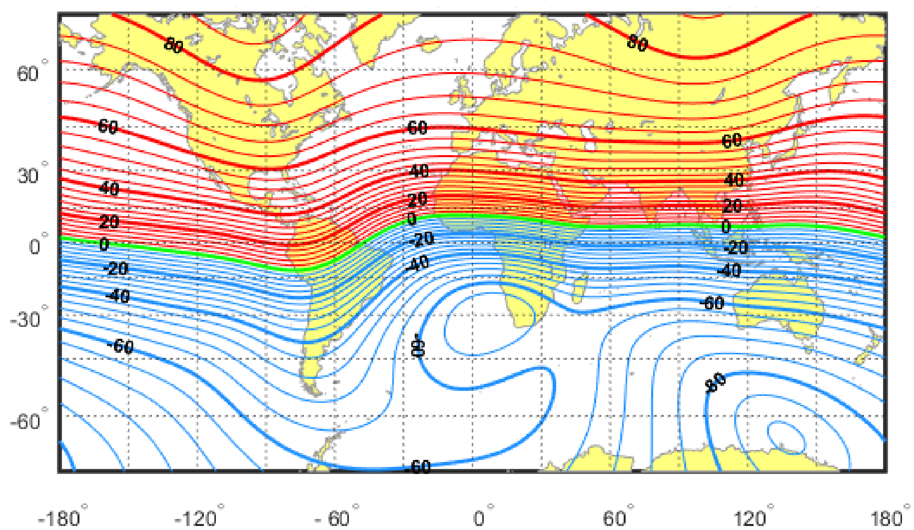

Figure 1.2: Earth magnetic inclinations at 400 km altitude, generated in MATLAB using the World Magnetic Model 2020.

The PMAC system is a predictable, stable system, suited well for space weather missions; however, for the mission requirements of VIOLET, a more dynamic, novel solution is required. The mission requirements are used to guide the development of the HMAC sub-system requirements [1], which can be found in Appendix A. As per sub-system requirement R-SYS-1150, the maximum rate of rotation per axis is 1.5 deg/s and a post-deployment settling time of less than 7 days. Additionally, sub-system requirement R-SYS-1140 defines a requires a pointing accuracy of at least 15° relative to the Earth's local geomagnetic field vector. The process of characterization of these parameters is outlined in Chapter 3 [2].

By utilizing a permanent magnet, ferromagnetic hysteresis rods, and magnetic torque coils, the magnetic dipole of the spacecraft can be changed, or deflected from its default position, aligned with the Z-axis. VIOLET, with its labelled magnetic and body-fixed axes is shown in figure 1.3. The magnetic dipoles created, orthogonal to the permanent magnet, will create this angular offset of the magnetic dipole. After a phase of transience, VIOLET will reach a relatively steady state attitude, at which time it will be at the required offset relative to the local Geomagnetic Field Vector (GFV) to allow SASI to begin imaging operations. Additionally, the Z-axis torque coil can either increase or null out a portion of the permanent magnet's dipole, by changing its polarity. This results in an increase of X and Y torque coil control authority as well as a larger Beta angle, which is the angle between the body-fixed Z axis and the resultant magnetic dipole, $\vec{m}'$, which is shown in Figure 1.3. However, an increase in Beta angle comes at the cost of higher steady state rates of rotation and less predictable attitude dynamics.

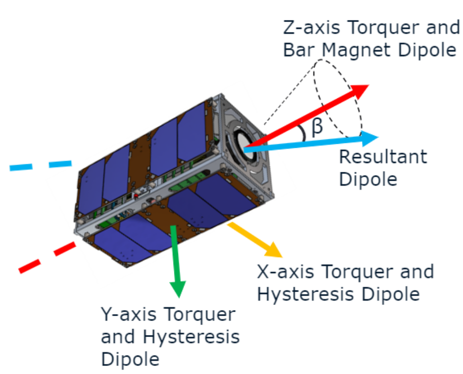

Figure 1.3: Magnetic axes of the VIOLET CubeSat.

1.4 Research Objectives

1.4.1 HMAC System Analysis and Design

The development of the HMAC system is of critical importance to a successful mission outcome. Due to the limited options for pointing that accompany a PMAC system, the concept of a hybrid system has been developed to give the mission more options for imaging the Earth's ionosphere. The high-level research objectives of this thesis, relating to the VIOLET ACS are to simulate, design, and analyze the HMAC system. To achieve the overall objectives, the work can be divided into the following sub-objectives:

- A PMAC system will be developed to ensure predictable and consistent attitude dynamics, even with the failure of active magnetic components. The attitude dynamics of the PMAC system will be analyzed under various deployment conditions to determine the effect on de-tumble time, steady state pointing error and body-fixed axial rates.

- The strength of the permanent magnet will be selected to suit mission requirements. Additionally, the volume of hysteresis material per X and Y axes will be optimized to ensure adequate damping of the system.

- The performance of the HMAC system will be analyzed via Smart Nanosatellite Attitude Propagator (SNAP) at various ranges of latitude. The optimal Beta angle yielding the longest and most consistent times in good pointing attitude will be determined for each latitude range. Distributions of time in good pointing attitude for each latitude range and corresponding optimal Beta angle will be determined.

- The body-fixed axes relative to the local GFV, body-fixed axial rates, magnetic torques, and hysteresis torques will be analyzed across all Beta angles to investigate the effect of Beta angle magnitude on the attitude dynamics of VIOLET.

1.4.2 Thermal Design and Analysis

Due to budgetary constraints, Thermal Vacuum (TVAC) chamber testing mat not be possible for VIOLET; this further underscores the importance of proper analysis. A passive control system has been chosen for this mission because of the volume, mass, power, and budgetary constraints inherent to a CubeSat mission. A passive system can be implemented with minimal hardware and power usage and can be easily adapted to sub-system design changes. Similar to the research objectives pertaining to the HMAC system, the high level research objectives of this thesis are to simulate, design, and analyze the thermal control system. The work can be divided into the following sub-objectives:

- VIOLET's thermal behavior will be simulated using Siemens NX Space Systems Thermal, a Finite Element Analysis (FEA) tool.
- VIOLET is a 2U nanosatellite, with an uncommon dual payload design. Additionally, VIOLET's S-band transceiver has a uniquely high thermal output. The thermal FEA results will drive the design of the passive thermal control system to ensure all components will fall within their temperature ranges, for Worst Case Hot (WCH) and Worst Case Cold (WCC) cases.
- To ensure the Finite Element Model (FEM) is not sensitive to mesh size, mesh sensitivity analyses will be conducted for transient board-to-board conduction as well as orbital radiation. For each analysis, three models will be used, with standard element size, fine mesh size and coarse mesh size.

1.5 Reference Frames

The three reference frames which apply to the orbital mechanics and attitude dynamics of VIOLET are the satellite body-fixed, the Earth Centered Inertial (ECI) and the Earth Centered Earth Fixed (ECEF) frames.

The satellite body-fixed frame has an origin at the centroid of the spacecraft [3]. The reference frame is shown in Figure 1.4. Unit vectors that describe the principal axes of the spacecraft are denoted as X, Y and Z, matching the NanoRacks CubeSat Deployer (NRCSD) reference frame [2]. The axes are defined by:

- X and Y are orthogonal and normal to the side panels of the spacecraft.
- Z aligns with the longitudinal axis of the spacecraft.
- The Z, Y, and X axes are aligned with the roll, pitch, and yaw axes, respectively.

The ECI frame origin is placed at the geometric center of the Earth, and is fixed independently from the rotation of the planet [3]. The ECI reference frame is shown in Figure 1.4. The axes can be denoted as X_{ECI}, Y_{ECI} and Z_{ECI} and are defined by:

- X_{ECI}-axis aligns with the Vernal Equinox.
- Y_{ECI}-axis is planar and orthogonal to X_{ECI}.
- Z_{ECI}-axis aligns with true north along the Earth's rotational axis.

The ECEF frame origin is at the geometric center of the Earth and its frame rotates with the planet. The axes are fixed to points on the surface of the Earth and do not change with respect to time [3]. The ECEF reference frame is shown in Figure 1.4. The axes can be denoted as X_{ECEF}, Y_{ECEF} and Z_{ECEF} and are defined by:

- X_{ECEF}-axis intersects the surface of Earth at 0° longitude, 0° latitude.
- Y_{ECEF}-axis is planar and orthogonal to X_{ECEF}.

- Y_{ECEF}-axis points true north along Earth's rotational axis.

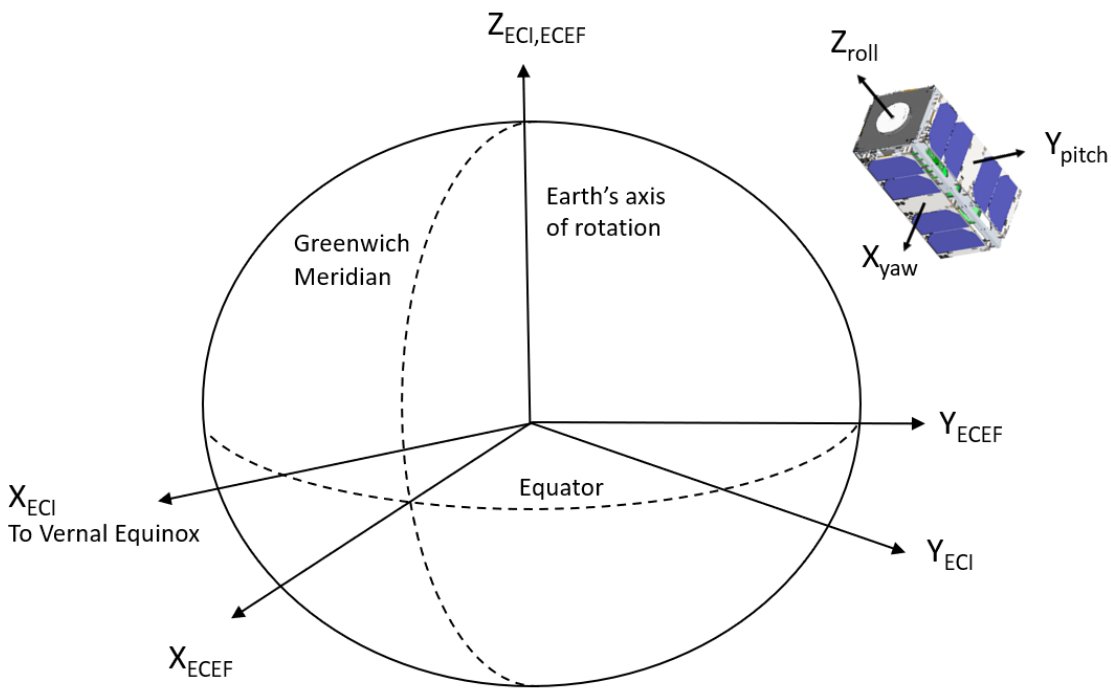

Figure 1.4: Inertial and fixed reference frames relevant to the simulation and analysis of the HMAC system.

Chapter 2

Literature Review

2.1 CubeSats Utilizing Magnetic Attitude Control

PMAC systems are a cheap and reliable option for coarse attitude control but are complicated by the complexity of modelling the non-linearity of hysteresis damping. More recently, active magnetic components such as magnetic torque coils have been utilized to give CubeSats more fine pointing and faster detumble than passive systems, by applying frequent, under-actuated torques to change attitude [4]. This method is also complicated by the complexity of the control algorithm and requires accurate, and usually expensive attitude determination systems. The HMAC system is a hybrid of the PMAC and active magnetic systems. In this section, a brief mission history of these methods applied to nanosatellite missions will be discussed.

2.1.1 Passive Magnetic Attitude Control

PMAC systems are an attractive option to many nanosatellite missions that do not require fine pointing. They are relatively cheap, do not need control electronics, are low mass and take up little volume. Additionally, the implementation of attitude determination is up to the other sub-system requirements, as it is not necessary for PMAC systems to control attitude.

The Colorado Student Space Weather Experiment (CSSWE) CubeSat was launched into an elliptical, 480 x 790 km, 65° inclination orbit in 2012. The nanosatellite included a PMAC system developed by students at the University of Colorado. Researchers saw the lack of literature pertaining to the modelling and development of the critical, non-linear hysteresis damping for these systems [5]. The CSSWE ADCS team set out to improve and better characterize PMAC performance. The consequences of incorrectly modelling the non-linearity of hysteresis damping can include long de-tumbling and settling times as well as stability issues, which can directly lead to mission failure. These consequences echo the importance of properly understanding and modelling PMAC systems. CSSWE utilized an 0.8 A·m^2 permanent magnet along with a total of six HyMu-80 hysteresis rods placed along the X and Y axes [5]. The CSSWE nanosatellite, moments after deployment, is shown in figure 2.1

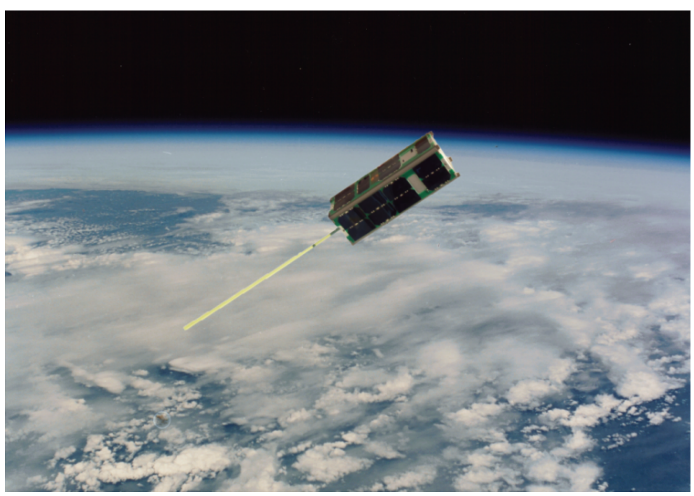

Figure 2.1: The CSSWE nanosatellite, directly after deployment from the ISS [5].

The CSSWE ADCS research team made excellent progress with characterizing hysteresis damping by analyzing both the magnetizing effect from the Earth's geomagnetic field and the energy dissipation of the hysteresis rods. Custom numerical simulations were developed utilizing different solvers to compare and contrast results. Detailed in a post-deployment paper [6], the CSSWE CubeSat's PMAC system performed as expected, de-tumbling after seven days converging to $\pm 15°$, from the local GFV. The spacecraft did not have on-board processing data however ground-based processing was performed with a Multiplicative Extended Kalman Filter (MEKF), which was developed specifically for CSSWE. The detailed technical design of the CSSWE PMAC system and its success makes this project a great resource for the research of the VIOLET HMAC system. After compiling over 3.5 million data points over two years, the CubeSat's mission ended due to battery failure [7].

The Radio Aurora Explorer (RAX-2) nanosatellite, launched in 2010 to an altitude of 650 km at a 71.97° inclination, was the first mission sponsored by the National Science Foundation. The RAX nanosatellite is shown in figure 2.2. Developed by the University of Michigan, RAX employed a PMAC system to accomplish its attitude requirements for studying space weather [8]. RAX, a 3U CubeSat, utilized an uncommonly strong permanent magnet, with a dipole moment of 3.2 A·m^2.

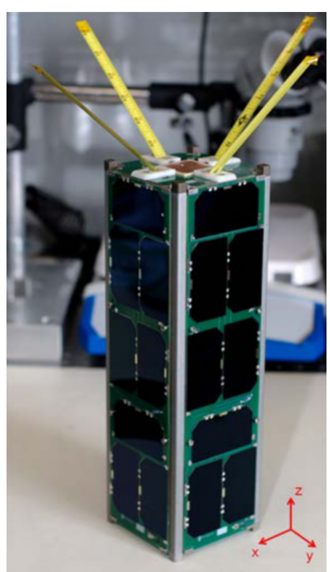

Figure 2.2: The RAX-2 nanosatellite [8].

The RAX team worked to predict the attitude dynamics of the spacecraft through use of a dynamic numerical model, named the Lie Group Variational Integrator (LGVI). A closed magnetic circuit was used to simulate hysteresis damping, which resulted in unrealistic damping performance predictions. Some factors overlooked in the design of the ACS were the saturation effect of the permanet magnet on the hysteresis rods, as the rods were placed on the same printed circuit board (PCB) as the magnet, the effect of saturation was significant. These design choices led to a predicted settling time of seven days converging to $\pm 15°$ from the local GFV [9]. Post flight data revealed the settling time was over 2 months, with a convergence to $\pm 20°$ from the local GFV. This discrepancy further highlights the importance of proper analysis as well as characterization and placement of magnetic components within a spacecraft.

2.1.2 Active Magnetic Attitude Control

With the increase in manufacturing and affordability of micro-electronics components, the implementation of active magnetic attitude control systems in nanosatellites was made possible. Missions have used active magnetic systems for de-tumble upon deployment, and more recently to achieve fine pointing throughout their mission [4][5]. The caveat of deploying an active magnetic system to achieve fine pointing is the high complexity of the control algorithm and cost of attitude determination sensors.

The MOVE-II CubeSat, developed by the Technical University of Munich, utilized an active magnetic ADCS with PCB integrated magnetic torquers, magnetometer and sun sensors. MOVE-II, a 1U CubeSat, has 2 ADCS modes: de-tumble and sun pointing [4]. The team highlighted the non-triviality of the control system implementation, as the torquers produce under-actuated torques, which interact with the quickly changing geomagnetic field. The CubeSat launched in 2018 and as of May 2020, is still operational.

The MOVE-II flight model is shown in figure 2.3.

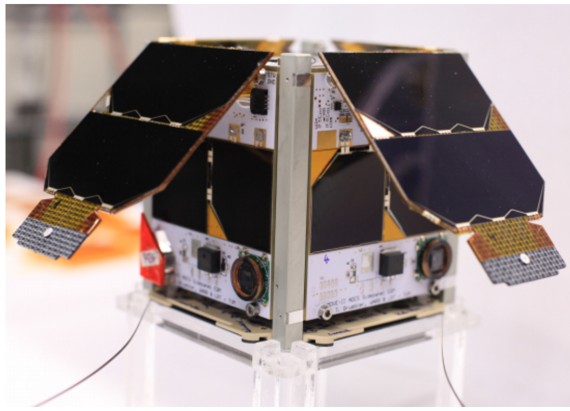

Figure 2.3: The MOVE-II nanosatellite [10].

The MOVE-II team has had major issues relating to very high rotational rates (310 deg/s) about the body Z-axis. In 2019, the MOVE-II team was able to stabilize the Z-axis rate to 10 deg/s by consistently switching from safe, to de-tumble mode [10]. The unexpected spike in spin rate further underscores the complexity of implementing a standalone active magnetic system, where the use of low resolution magnetometers and a novel control algorithm can have a large effect on mission success.

Compass-1, developed by the by the University of Applied Sciences, Achen, Germany, was launched in 2008 to an altitude of 590 km at a 97.6° inclination. The 1U nanosatellite utilized magnetic torque coils about each body-fixed axis, as the sole means of attitude actuation. The main attitude requirements of the mission were to be nadir pointing with a pointing error of 10°, which was to be achieved by Linear Quadratic Regulator, which drives the attitude quaternion and the rates of change into the required reference frame [11]. The magnetic dipole produced by each torque coil was a maximum of 0.08 A·m^2; however, under different thermal extremes, this value could vary up to 27%. Upon deployment, the nanosatellite was able to de-tumble using the coils and a B-dot control algorithm. Unfortunately, a flip of the X axis and a Y axis offset of the on board magnetometer made attitude determination for COMPASS-1 unreliable and therefore resulted in the magnetic torque coils not being able to function properly to satisfy the nadir pointing requirements [12]. The COMPASS-1 nanosatellite is shown in figure 2.4.

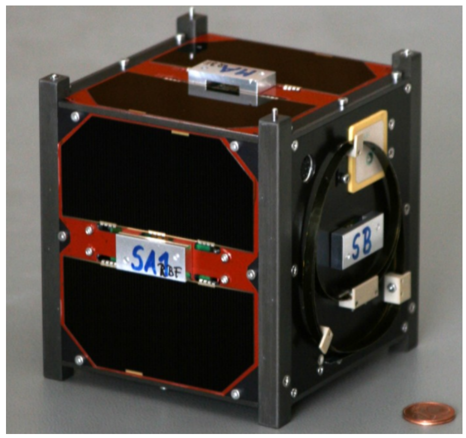

Figure 2.4: The COMPASS-1 nanosatellite [11].

2.2 Passive Thermal Control Mission History

For low cost, educational CubeSat missions, the utilization of passive thermal control systems is very common. With the small form factor and volumetric constraints inherent to CubeSats, they tend to run hot, therefore heat paths must be created using passive techniques. The following section will outline passive thermal control utilization in previous CubeSat missions.

2.2.1 CanX-7

The CanX-7 3U nanosatellite was developed by the University of Toronto's Space Flight Laboratory (SFL) and was launched in 2016 to an altitude of 700 km at a 98.1° inclination. CanX-7 employed a passive thermal control system using thermal gap pads, thermal tapes and structural modifications such as material selection and part modifications to change heat flow paths throughout the bus. The thermal control methods and FEA were ultimately verified by a thermal vacuum test conducted at SFL facilities [13]. After a successful 7 month mission, the drag sails were deployed, resulting in a significantly shortened time to de-orbit. The flight model of CANX-7 is shown in figure 2.5.

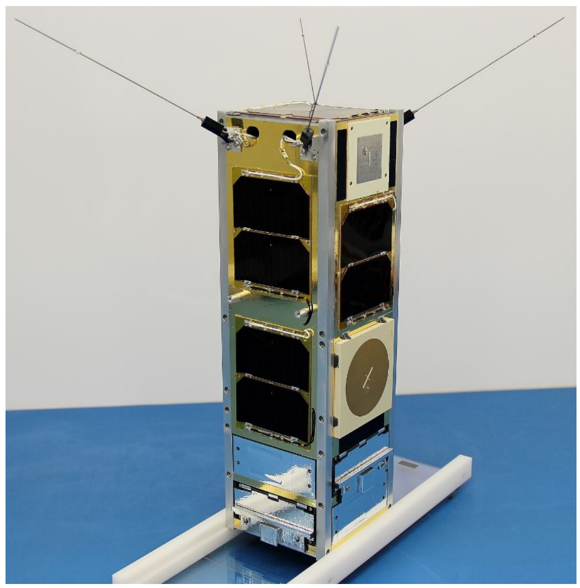

Figure 2.5: The CANX-7 nanosatellite [13].

2.2.2 CanX-1

CanX-1, a 1U nanosatellite, developed at SFL was launched to a 900 km, sun-synchronous orbit, in 2003. This nanosatellite was the first in an innovative program that helped start the small satellite revolution in Canada. As with other nanosatellite missions, constraints relating to form factor and power dictate the methods of thermal control employed. CanX-1 used a passive thermal control system to move heat throughout the satellite bus and ensure components stayed within their operational and survival limits [14]. Additionally, if problems regarding thermal ranges occurred in analysis, than mitigating steps such as the addition of thermal coatings or paints would be used. A multi-nodal thermal model of CanX-1 was developed, including transient analysis to characterize the various thermal conditions the spacecraft would experience during its mission. The transient internal power dissipation for the spacecrafts sub-systems was also included in the model to further its accuracy. These analyses were conducted using the IDEAS TMG software [14]. Unfortunately, deployment failure resulted in loss of mission. The flight model of CANX-1 is shown in figure 2.6.

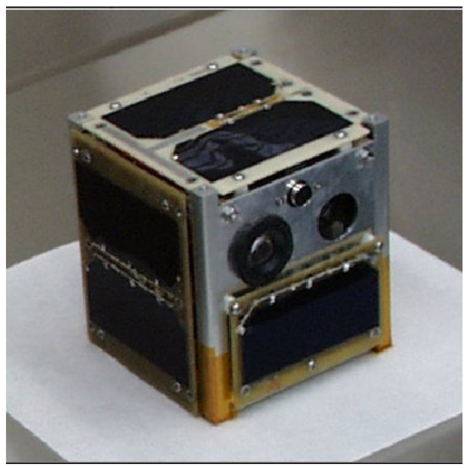

Figure 2.6: The CANX-1 nanosatellite [14].

Chapter 3

Attitude Control System Development Methodology

This chapter will focus on the methodology of the research and development of the HMAC Attitude Control System. The environmental conditions in Low Earth Orbit (LEO) will be outlined, along with defining the numerical models that make up SNAP. Validation of software tools will be discussed as well as important concepts pertaining to magnetic component selection, actuation, hysteresis damping, orbital propagation, and dynamics. Critical symbols relevant to the HMAC system can be found in figure 3.1.

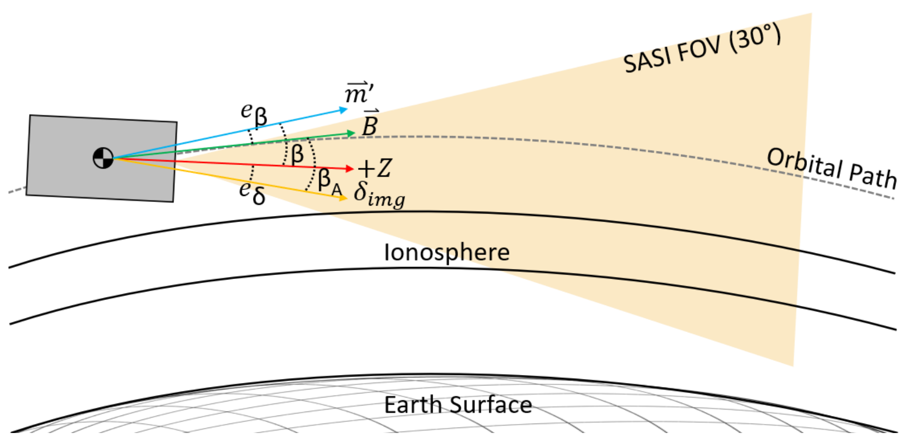

Figure 3.1: Critical symbols related to the HMAC system.

During passive operation of the ACS, the Z (roll) axis of VIOLET will be constantly tracking the local GFV. The angle between the Z axis and the inclination angle for imaging, δ_{img}, is described as inclination error, e_δ. Inclination error is determined by calculating the difference of the Z axis and the spacecraft's velocity vector. In the case of HMAC operations, for a desired imaging latitude, the torque coils will be powered to develop the optimal angle between the Z axis and HMAC magnetic dipole vector, $\vec{m}'$, described as the Beta angle, β. $\vec{m}'$ will not be perfectly aligned with the local GFV, $\vec{B}$. This error is described as Beta error, e_β. The actual Beta angle, β_A is the angle between $\vec{B}$ and the Z axis. For passive operation, the spacecraft's magnetic moment will be aligned with the Z axis, the error describing the spacecraft's imaging axis to acceptable imaging inclination is e_δ. The Beta angle ideally equals zero during passive operations.

3.1 Attitude Dynamics Simulations

The SNAP is the resource being utilized to simulate the ACS system for the VIOLET nanosatellite [15]. SNAP is a MATLAB® Simulink toolbox that utilizes numerical models and the Ode45, fifth order, Runge Kutta solver to propagate the attitude dynamics, and orbit of a nanosatellite over a selected time period [16]. This section will outline the mathematical models that SNAP uses as well as the design and analysis methodology for the ACS system.

3.1.1 Environmental Disturbance Torques

While a nanosatellite is orbiting the Earth, it will be acted upon by various environmental disturbance torques. These torques vary in magnitude and must be quantified to ensure that the spacecraft has adequate control authority for actuation and adequate attitude control. The disturbance torques that are modelled in SNAP include; aerodynamic and gravity gradient. Solar Radiation Pressure (SRP) is considered negligible for nanosatellites orbiting Earth at an altitude of 400 km [17]. All disturbance and internal torques are calculated at each time step.

While in LEO a spacecraft will still encounter the effects of aerodynamic drag, primarily from atomic oxygen. The analytical model for determining the aerodynamic torque vector, $\vec{M}_{aero}$, acting on the spacecraft was derived from fluid mechanics principles and is defined as [17],

$$\vec{M}_{aero} = \frac{1}{2}\rho V^2 C_D A_{proj}(\hat{u}_v \times \hat{s}_{cp}) \tag{3.1}$$

where ρ is the fluid density, V is the spacecraft velocity magnitude, C_D is the drag coefficient, A_{proj} is the projected area orthogonal to the velocity unit vector, $\hat{u}_v$ is the unit velocity vector and $\hat{s}_{cp}$ is the vector from center of pressure to center of mass.

SNAP utilizes this equation, however to accurately define aerodynamic torques applied to the spacecraft, a point cloud model is used. The function plots the 3 dimensional outer geometry of the nanosatellite, after which, atmospheric densities are determined using a look up table and the current attitude dynamics and velocity vector are applied to the model. The drag coefficient is set as 2, for a rectangular box [18]. This model yields the aerodynamic disturbance torque about the pitch and yaw axes only.

In real applications, a spacecraft will likely not have its center of gravity aligned with its center of geometry. The consequence of this is gravity gradient torque. An asymmetric body in a gravitational field will be acted upon by a torque, which will attempt to align the axis of least inertia with the field direction. Alternatively, if one of the principal axes of the spacecraft is aligned with the local vertical, then there is no gravity gradient torque affecting the spacecraft. SNAP utilizes a 2-body gravitational model to numerically create the effects of gravity gradient torque and propagate them throughout the simulation. The basic equation is defined as [17],

$$\vec{M}_{gg} = \frac{3\mu}{R^3} \hat{u}_e \times \mathbb{J}_{rpy} \hat{u}_e \tag{3.2}$$

where $\vec{M}_{gg}$ is the torque vector being applied to the spacecraft due to gravity gradient, μ is the Earth's gravitational constant, R is Earth's radius, $\hat{u}_e$ is the unit vector pointing nadir, and $\mathbb{J}_{rpy}$ is the spacecraft's moment of inertia matrix.

3.1.2 Magnetic Field Model

SNAP calculates magnetic field variables from the L-Shell magnetic field model, an idealized dipole model for Earth [19]. This model is quite useful for the purpose of reducing computational time for a simulation; however its simplification could offer "best case scenario" results to the user. The Earth's magnetic field is created by a dynamo effect in the planet's core, which creates a far from symmetric magnetic field that is not aligned with the Earth's spin axis. Using the L-Shell method, the magnetic field at a specific location can be calculated in vector form as [19],

$$\vec{B} = \frac{R^3 H_0}{||\vec{X}_{ECI}||^3} [3(\hat{u}_m \cdot \hat{u}_x)\hat{u}_x - \hat{u}_m] \tag{3.3}$$

where H_0 is the magnetic dipole strength of the Earth, $\hat{u}_m$ is the unit vector aligned with the magnetic dipole and $\hat{u}_x$ is the unit position vector where the magnetic field strength is being calculated, and $\vec{X}_{ECI}$ is the position of the spacecraft in ECI. The torque created from a magnetic dipole about each of the axes can then be calculated as,

$$\vec{M}_{mag} = \vec{m} \times \vec{B} \tag{3.4}$$

where $\vec{m}$ is the magnetic dipole vector of the spacecraft and $\vec{B}$ is the magnetic flux density of the local GFV [19]. To calculate the magnetic torque induced by the HMAC system, $\vec{m}$ is substituted with $\vec{m}'$.

3.1.3 Magnetic Hysteresis Model

A ferromagnetic material has a non-zero magnetization. This magnetization changes when the material is exposed to an external magnetizing field. When a magnetic field, *H*, is applied, the magnetic domains will begin to align with the applied field. To characterize the hysteresis parameters in a ferromagnetic material, a varying magnetizing field is applied, and the magnetic flux density, *B*, is measured [20]. Plotting *B* versus *H* yields the hysteresis loop. The theoretical magnetic hysteresis loop is shown in Figure 3.2.

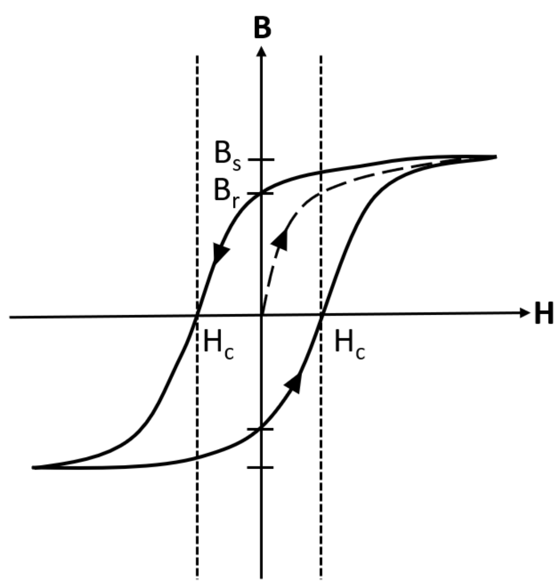

Figure 3.2: Theoretical magnetic hysteresis curve.

Some important parameters to consider when implementing hysteresis damping are coercivity, remanence, and saturation, denoted as Hc, Br, and Bs, respectively. Coercivity is measured in A/m, it is the intensity of the applied magnetic field necessary to reduce the magnetization of the material to zero after the magnetization of the sample has been reduced to zero. Thus, coercivity is the resistance of a ferromagnetic material to becoming demagnetized. Remanence is measured in tesla and is the remaining magnetic flux held within the material when the magnetizing field is decreased to zero or has been removed. Saturation is measured in tesla. It is the state reached when an increase in applied external magnetic field, H, cannot increase the magnetization of the material further [20]. Saturation occurs when all magnetic domains align, thus there is no more magnetization potential. When analyzing a hysteresis loop, it important to note that the point on the curve when B_s starts to increase with slope of μ_o is the saturation flux density. On the same plot, the area under the curve is the energy absorbed by the material, per unit volume, by cycle [20].

For stable flight and adequate damping, it is of critical importance for a PMAC system to accurately model and approximate the hysteresis loop. This can be done with the Flatley model, which adds time variance to the numerical model. With the addition of time variance, minor hysteresis loops can be modelled within the full loop as the hysteresis material experiences different magnetizing field cycle amplitudes. The Flatley model can be defined by the following, based on the sign of the magnetizing field time derivative [21], If $\frac{d\vec{H}}{dt} \geq 0$,

$$\dot{\vec{B}}_{hys} = \left[\frac{1}{2H_c}\left(\vec{H} - \frac{1}{k}\tan\left(\frac{\pi\vec{B}_{hys}}{2B_s}\right) + H_c\right)^p \left(\frac{2kB_s}{\pi}\right)\cos^2\left(\frac{\pi\vec{B}_{hys}}{2B_s}\right)\right]\frac{d\vec{H}}{dt} \tag{3.5}$$

If $\frac{d\vec{H}}{dt} < 0$,

$$\dot{\vec{B}}_{hys} = \left[\frac{1}{2H_c}\left(\vec{H} - \frac{1}{k}\tan\left(\frac{\pi\vec{B}_{hys}}{2B_s}\right) - H_c\right)^p \left(\frac{2kB_s}{\pi}\right)\cos^2\left(\frac{\pi\vec{B}_{hys}}{2B_s}\right)\right]\frac{d\vec{H}}{dt} \tag{3.6}$$

where the constant, k, is defined by,

$$k = \frac{1}{H_c}\tan\left(\frac{\pi}{2}\frac{B_r}{B_s}\right) \tag{3.7}$$

and p is a constant, usually set to 2 for hysteresis modelling for PMAC systems. The variable k is an arbitrary constant calculated at $\vec{H} = 0$. The magnetizing field, $\vec{H}$ is calculated as $\vec{H} = \vec{B}_{hys}/\mu_0$, with μ_0 being the permeability of space. For this model, the magnetic flux density differentiated by time, $\dot{\vec{B}}_{hys}$, is dependent on $\vec{B}$, $\vec{H}$, $\frac{d\vec{H}}{dt}$, H_c, B_r, and B_s. The main benefit of this model is that it is possible to integrate it into a six Degree of Freedom (DOF) dynamic model including simulated magnetizing fields seen in orbit. Hysteresis loops of varying magnetizing field cycle amplitudes created using the Flatley model are shown in Figure 3.3. With a higher magnetization potential and applied magnetizing field, the area in a hysteresis loop and its energy dissipation per cycle and unit volume, will be greater, resulting in more damping [21].

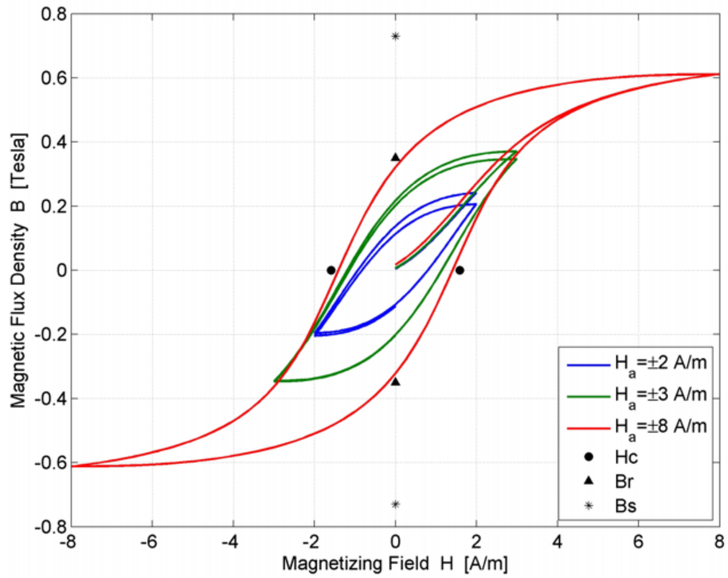

Figure 3.3: Multiple hysteresis loops with varying field cycle amplitudes, generated with the Flatley hysteresis model [5].

3.1.4 Orbital Propagation

The Keplerian elements of a spacecraft define its orbit at a specified epoch. These elements can be found in a Two Line Element (TLE) file, consistently updated by the United States Air Force (USAF). SNAP takes a TLE file as an input to generate the initial conditions of a spacecraft's orbit, specifically, initial position, $\vec{X}_0$, and initial velocity, $\dot{\vec{X}}_0$, in ECI. An example TLE file used to simulate the VIOLET ACS is shown in Figure 3.4.

```
ISS (ZARYA)
1 25544U 98067A   21020.53488036  .00016717  00000-0  10270-3 0  9054
2 25544  51.6423 353.0312 0000493 320.8755  39.2360 15.49309423 25703
```

Figure 3.4: Two Line Element file used in SNAP simulations, ISS (Zarya).

To determine the force of gravity acting on the axes of the spacecraft, $\vec{F}_g$, SNAP utilizes the 2-body gravitation model. At each time step, it is calculated based on position in orbit. The modelled force of gravity acting on a spacecraft can be described by the following [16],

$$\vec{F}_g = -\frac{G m_E m_s}{\vec{X}_{ECI} \cdot \vec{X}_{ECI}} \hat{u}_N \tag{3.8}$$

where G is the Newtonian gravitational constant, m_E is the mass of Earth, m_s is the spacecraft mass, $\vec{X}_{ECI}$ is the spacecraft position, and $\hat{u}_N$ is the unit vector pointing Nadir. From the calculated gravitational force, the spacecraft acceleration is then determined by,

$$\ddot{\vec{X}}_{ECI} = \frac{\vec{F}_g}{m_s} \tag{3.9}$$

SNAP then calculates the velocity, $\dot{\vec{X}}_{ECI}$ by integrating acceleration. The spacecraft position vector is then determined by integrating the velocity vector. The position, velocity and acceleration of the spacecraft are calculated at each time step. The orbital propagation model accounts for the first six state variables, the next sub-section will discuss how the remaining 6 state variables are calculated.

3.1.5 Attitude Dynamics Model

SNAP takes advantage of the Simulink 6-DoF dynamics block to model the spacecraft's attitude dynamics at each time step of the simulation. The Ode45 solver is utilized in SNAP and will be discussed later in this section. The 6-DoF dynamics model takes inputs applied torque from environmental and internal sources. The model outputs Euler angles, rotational rates as well as converted attitude from ECI to body-fixed. The 6-DoF attitude dynamics model can be found in Appendix B.

The previously mentioned reference frames; ECEF, ECI and body-fixed are all used in the numerical simulations to describe the motion of Earth as well as VIOLET. To transform between these reference frames, rotation matrices are used [22]. The rotation between these frames can be accomplished by use of the Direction Cosine Matrix (DCM), a 3 by 3 matrix which describes the rotations between reference frames. The order of rotation is important as a different sequence will result in a different final state of the rigid body. The transformation between two frames can be separated into rotations about each body-fixed axis as,

$$\mathbb{R}_1(\phi_1) = \begin{bmatrix} 1 & 0 & 0 \\ 0 & \cos(\phi_1) & \sin(\phi_1) \\ 0 & -\sin(\phi_1) & \cos(\phi_1) \end{bmatrix} \tag{3.10}$$

$$\mathbb{R}_2(\phi_2) = \begin{bmatrix} \cos(\phi_2) & 0 & -\sin(\phi_2) \\ 0 & 1 & 0 \\ \sin(\phi_2) & 0 & \cos(\phi_2) \end{bmatrix} \tag{3.11}$$

$$\mathbb{R}_3(\phi_3) = \begin{bmatrix} \cos(\phi_3) & \sin(\phi_3) & 0 \\ -\sin(\phi_3) & \cos(\phi_3) & 0 \\ 0 & 0 & 1 \end{bmatrix} \tag{3.12}$$

where the DCM is defined as,

$$\mathbb{C} = \mathbb{R}_1(\phi_1)\,\mathbb{R}_2(\phi_2)\,\mathbb{R}_3(\phi_3) \tag{3.13}$$

The rotation angles ϕ_1, ϕ_2, ϕ_3 are the Euler rotation angles and are about the roll, pitch, and yaw axes, respectively. Euler angle representation is an intuitive and efficient means of describing the rotation of a rigid body, however the dynamic equations can suffer from singularities. Trigonometric functions are present in the mathematical descriptions, which can lead to losing a degree of freedom, at certain angular positions. The rotation between two frames can then be found by multiplying the desired frame matrix by the DCM, seen in equation 3.13.

Quaternions, or Euler Parameters, are vectors comprised of four elements, one real and three complex. They provide a redundant, singularity-free attitude description and can describe arbitrary and large rotations [22]. The quaternion elements shown below can be used to determine the quaternion vector $\boldsymbol{q}$ by [16],

$$\boldsymbol{q} = [q_1\ q_2\ q_3\ q_4]^T \tag{3.14}$$

$$q_1 = e_1 \sin\left(\frac{\phi}{2}\right) \tag{3.15}$$

$$q_2 = e_2 \sin\left(\frac{\phi}{2}\right) \tag{3.16}$$

$$q_3 = e_3 \sin\left(\frac{\phi}{2}\right) \tag{3.17}$$

$$q_4 = \cos\left(\frac{\phi}{2}\right) \tag{3.18}$$

where $[e_1\ \ e_2\ \ e_3]^T$ is the Eigen axis, $\boldsymbol{e}$, and can be described as the axis about which the rigid body rotates to change its attitude [22]. The relation between the kinematic equations and body-fixed rotation rates of the rigid body can be described as [16],

$$\dot{\mathbb{C}} + \Omega\mathbb{C} = 0 \tag{3.19}$$

where Ω is described with the body-fixed rates of rotation as,

$$\Omega = \begin{bmatrix} 0 & -\omega_3 & \omega_2 \\ \omega_3 & 0 & -\omega_1 \\ -\omega_2 & \omega_1 & 0 \end{bmatrix} \tag{3.20}$$

The kinematic equation in quaternion form can then be described as,

$$\dot{q} = \frac{1}{2}(q_4\omega - \omega \times q) \tag{3.21}$$

where $\dot{q}_4$ is,

$$\dot{q}_4 = -\frac{1}{2}\omega^T q \tag{3.22}$$

To solve for axial rates of rotation, the summed disturbance torque vector in body-fixed frame, is input into the dynamics equation (3.24) as,

$$\vec{M}_{Total} = \vec{M}_{gg} + \vec{M}_{aero} + \vec{M}_{mag} + \vec{M}_{hys} \tag{3.23}$$

$$\vec{M}_{Total} = \mathbb{J}\dot{\vec{\omega}} + \vec{\omega} \times \mathbb{J}\vec{\omega} \tag{3.24}$$

where $\vec{M}_{Total}$ is the total angular moment being applied to each axis and $\mathbb{J}$ is the spacecraft's mass moment of inertia matrix and $\vec{\omega}$ is the axial rotation rate vector, to be solved. The DCM does not need to be applied to the solving the rates of rotation of the spacecraft, as the moments are already in the body-fixed reference frame.

There is no standard rule for determining whether a system is stiff or non-stiff, however both stiff and non-stiff solvers can be applied to determine a system's stiffness. To determine solver type for SNAP, both types of solvers where tested, resulting in the system being characterized as non-stiff. The Ode45 solver was chosen as the optimal numeric integrator for SNAP due to it over-performing the stiff system solver, Ode23.

3.1.6 Attitude Dynamics Model Validation

SNAP was designed with a user interface, into which system parameters can be input, such as: axis inertias, mass, TLE files, magnetic properties, form factor, simulation time, and initial rates. After the course of a simulation, SNAP will output relevant dynamic and magnetic data as well as plots including: torque magnitudes, axes relative to Earth's local magnetic field vector, and rotational rates about each axis. This data is then analyzed post simulation to understand the attitude dynamics behavior of the spacecraft being analyzed.

In order to validate SNAP for use in simulating the attitude dynamics of VIOLET, a previously flown CubeSat mission has been analyzed. As mentioned in chapter 2, the CSSWE nanosatellite employed a PMAC system, and was comprehensively simulated by a custom numerical model. The CSSWE attitude dynamics simulation results gave a settling time of seven days and from on-orbit data received during flight, the de-tumble time of seven days was confirmed. However, a Z-axis to GFV steady state Beta angle was simulated to be under 5° but was actually found to be 15° on-orbit. Unfortunately there is no data available pertaining to on-orbit rates of rotation of CSSWE [6]. The data used to run the SNAP verification simulations can be seen in Table 3.1 [5].

The plots comparing CSSWE's deployment to settling time can be seen in Figures 3.5 through 3.8. It should be noted that differences in the operation of SNAP and the CSSWE simulation method would not allow for some of the inputs to be used in SNAP, where the grey rows in Table 3.1 indicate those inputs. Some of these inputs include initial roll axis angle relative to GFV and inputs relating to torque due to solar pressure. Additionally, SNAP does not model the torque due to aerodynamic drag about the roll axis. The magnitude of this torque is significantly lower than that about the pitch and yaw axes. The consequence of this is different steady state roll rate results between the different simulation tools.

Table 3.1: CSSWE SNAP Validation Inputs.

Parameter	Value	Units
CubeSat form factor	3	U
Numeric integrator	RK4	
Time step	0.1	s
Mass	4.6	kg
Initial Rates	$[0.17\ -0.97\ 2.93]^T$	deg/s
Moments of inertia	$[2.22{\cdot}10^{-2}\ 2.18{\cdot}10^{-2}\ 5.00{\cdot}10^{-3}]^T$	kg·m^2
Permanent magnet moment vector	$[0\ 0\ 0.55]^T$	A·m^2
Hysteresis rods per axis	$[3\ 3\ 0]^T$	
Hysteresis rod length	95	mm
Hysteresis rod diameter	1	mm
Hysteresis rod coercivity H_c	0.3381	A/m
Hysteresis rod remenance B_r	$6.0618{\cdot}10^{-4}$	Tesla
Hysteresis rod saturation B_s	0.3000	Tesla
Residual magnetic moment vector	$[0.0059\ 0.0083\ -0.0004]^T$	A·m^2
Orbital inclination	64.7	Degrees
Orbital altitude	478 x 786	km
Base initial Euler angles	[13.9 -71.6 104.1]	deg
Initial magnetic field offset	178.1	deg
CG to geometric center vector	$[2.601\ -0.218\ -8.086]^T$	mm
Satellite coefficient of reflectivity	0.8	
81 day average F10.7 flux	$168.5{\cdot}10^{-22}$	W·m^{-2}Hz^{-1}
Daily F10.7 flux for previous day	$128.7{\cdot}10^{-22}$	W·m^{-2}Hz^{-1}
Solar pressure at Earth	$4.5{\cdot}10^{-6}$	N·m^2

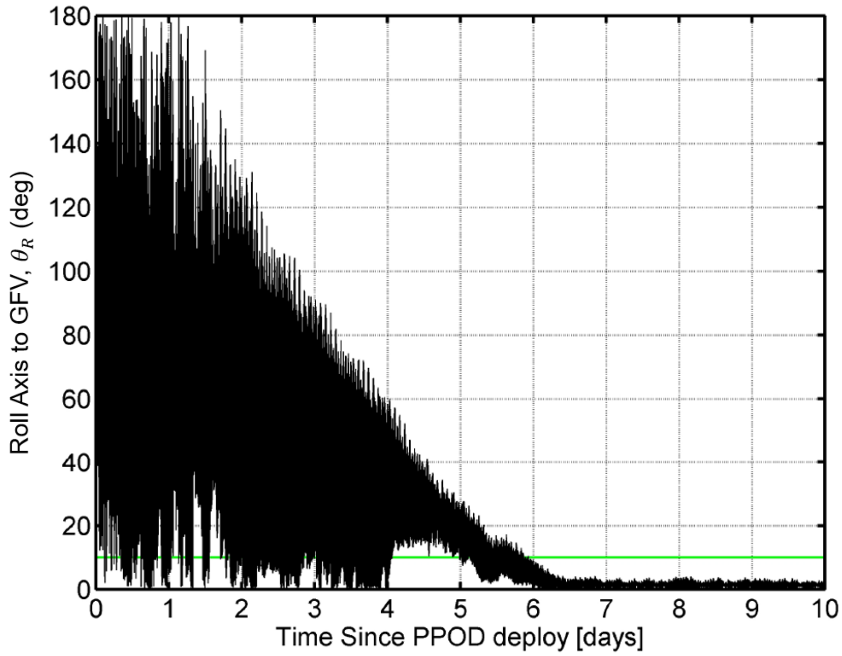

Figure 3.5: Original CSSWE simulation output of Z-axis relative to local GFV, θ_R [5].

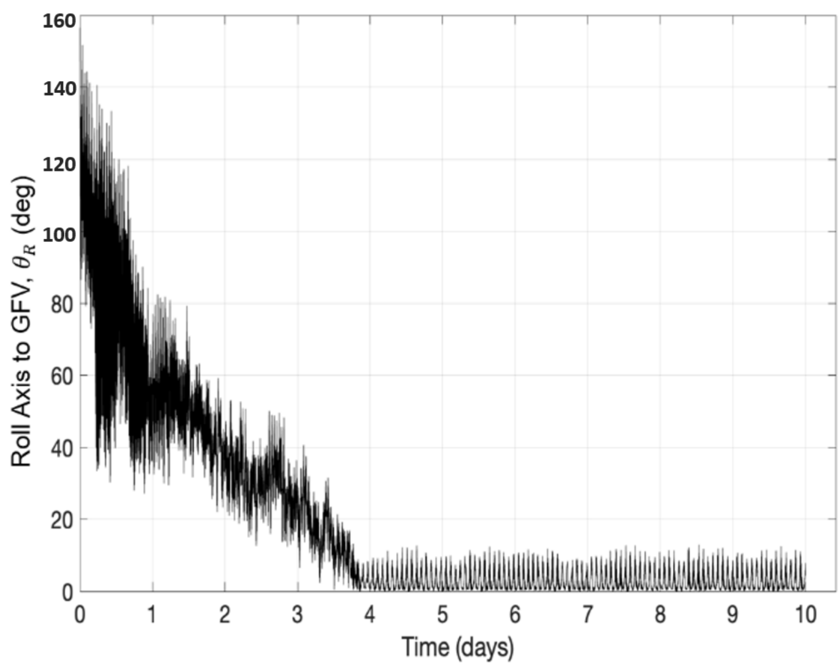

Figure 3.6: SNAP CSSWE simulation output of Z-axis relative to local GFV, θ_R.

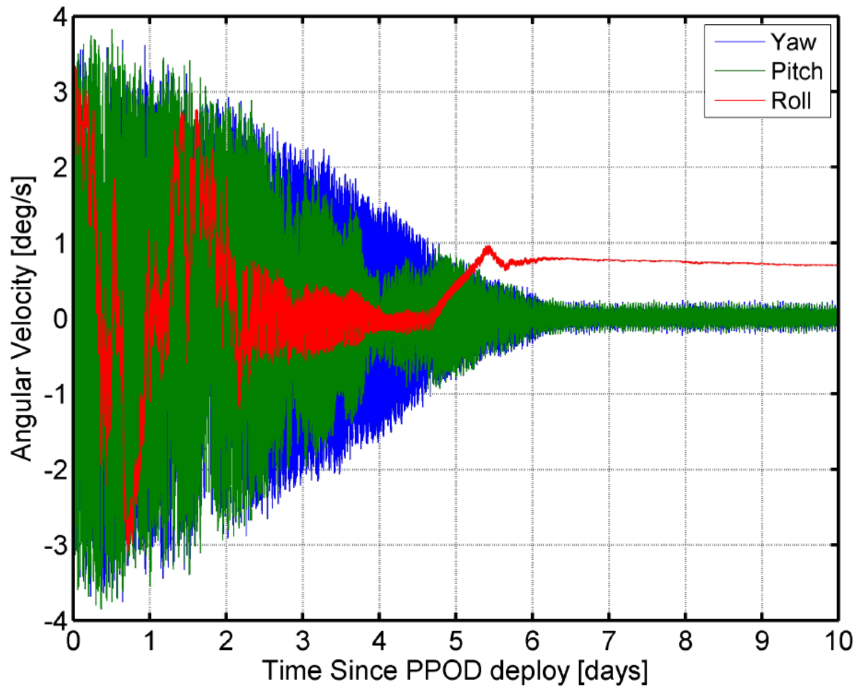

Figure 3.7: Original CSSWE simulation output of body-fixed rotational rates [5].

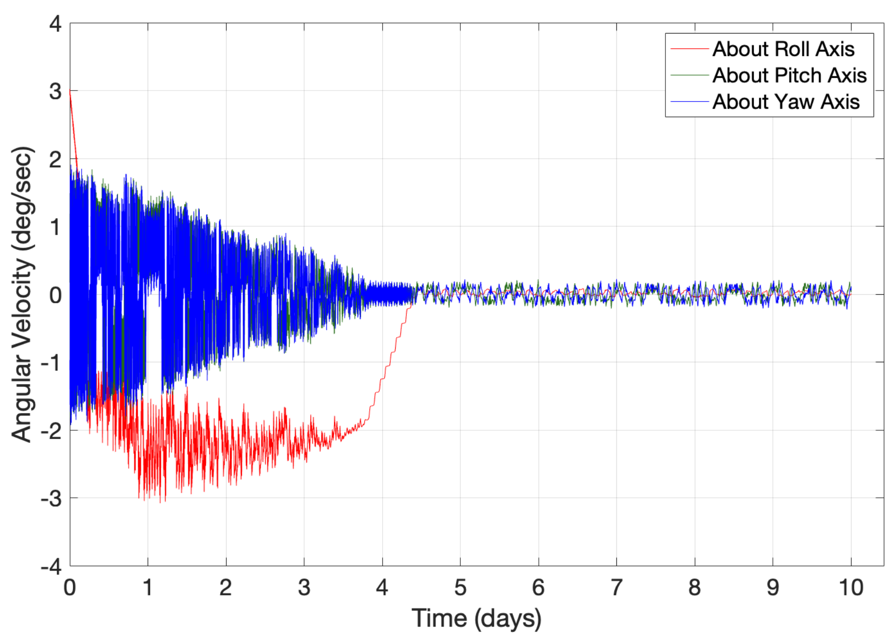

Figure 3.8: SNAP CSSWE simulation output of body-fixed rotational rates.

The process for validating SNAP is to simulate the CSSWE spacecraft during de-tumble phase and then compare the results with the data from the CSSWE simulations. The results being compared include; roll axis relative to GFV, θ_R and body-fixed rates of rotation, $\vec{\omega}$.

Comparing Figures 3.5 and 3.6, it can be seen that for the original CSSWE simulations, the spacecraft reaches steady state in six days, where as the SNAP simulation takes just under four. This 30% difference can be explained by the differences in allowable simulation inputs, specifically, SNAP's lack of a SRP model and the inability to set the initial Beta angle. Upon comparison of steady state, mean θ_R, the SNAP results align closer to the CSSWE on-orbit steady state θ_R of 15°.

Comparing the rotational rate plots (Figures 3.7 and 3.8), it can be seen that the roll axis SNAP results converge to below 1 deg/s compared to the CSSWE simulations. The differences can be explained in part, by the large differences in magnetic field models as SNAP utilizes a symmetrical L-shell model where CSSWE simulations utilize data from the International Geomagnetic Reference Field (IGRF). Upon reaching stability, the rotational rates about the pitch and yaw axes (X and Y) from both simulations are essentially the same, however the SNAP plot shows the roll axis (Z) reaching steady state near 0.1 deg/s compared to CSSWE simulation showing 0.8 deg/s. The likely cause of this disparity is the SNAP aerodynamic model not accounting for torque about the roll axis.

3.2 Attitude Control System Design

This section will outline the design process necessary to ensure the ACS magnetic components yield adequate performance, as specified by the mission requirements of the

VIOLET nanosatellite mission [2]. Permanent magnet selection, hysteresis volume optimization, torque coil design, and the integrated HMAC system design will be discussed in detail.

3.2.1 Permanent Magnet Selection

As the permanent magnet is the primary actuation source in a PMAC system, it is important to ensure a strong enough magnet is selected to allow for the spacecraft to align itself with the local geomagnetic field vector. Selection of a permanent magnet with adequate strength to overcome environmental disturbance torques is critical as a magnet too strong can result in high Z-axis rates of rotation. Conversely, a weak magnet will not allow the spacecraft to track the GFV to the required accuracy. To calculate the minimum dipole moment, m_{min}, required for a PMAC system in LEO, the following formula is used [23],

$$m_{min} = 10 \cdot \frac{T_{RMS}}{B_{min} \cdot \sin(\beta_{max})} \tag{3.25}$$

where T_{RMS} is the root mean square (RMS) of the environmental disturbance torques that the spacecraft is subject to at 400 km altitude (Table 3.2), B_{min} is the minimum Earth magnetic field flux at 400 km altitude ($3 \cdot 10^{-5}$ Tesla), and β_{max} is the required pointing accuracy or alignment angle from the spacecraft's principal magnetic axis and the local geomagnetic field vector (10°) [23]. This calculation gives a good starting point to begin simulating the system with m_{min} being found to be 0.45 $A \cdot m^2$. Preliminary simulations showed that the calculated minimum was indeed just that, and the system proved to be unable to get close to the required 10° pointing accuracy; thus a stronger magnet was required. Multiple simulations were conducted by increasing the strength of the permanent magnet from m_{min} at increments of 0.05 $A \cdot m^2$. At each step of increasing magnetic dipole strength, the volume of hysteresis material was roughly calibrated for suitable damping. The iterative process was repeated until the pointing accuracy requirements were met, by ensuring a steady state mean Beta angle of at least 10°. The adequate magnetic dipole strength was found to be 0.8 A·m^2.

Table 3.2: Environmental Torque Magnitudes and RMS sum Experienced by a 2U CubeSat at 400 km Altitude.

Torque	Value (N·m)
Aerodynamic	$3 \cdot 10^{-7}$
Gravity Gradient	$3 \cdot 10^{-8}$
RMS Sum	$2.3 \cdot 10^{-7}$

3.2.2 Hysteresis Selection

Upon selection of a bar magnet, the remaining step is to determine how much hysteresis material will be used in the spacecraft by optimizing damping through iterative simulations. Similar to the torque generated by the bar magnet, the hysteresis torque is defined by,

$$\vec{M}_{hys} = \vec{m}_{hys} \times \vec{B} \tag{3.26}$$

The behavior of hysteresis rods relates directly to the B/H curve which is dependent on the combination of material, treatment and length-to-diameter ratio (l/d). Additionally, it is necessary to place rods on the same axis apart at least 30% of their length to ensure their magnetic interaction will not negatively affect damping [24].

The material being used for the hysteresis rods is HyMu-80, a standard ferromagnetic material used in PMAC systems with flight heritage. The hysteresis rods act as non-linear dampeners by removing much of the oscillations caused by the continuous GFV tracking by the permanent magnet. The amount of hysteresis material chosen will have a direct effect on settling time, pointing accuracy and axial rates. With the adequate amount and correct placement of the hysteresis material, an optimal damping scenario will occur. This scenario will be a balance between the two types of PMAC error; steady state and oscillatory error [5]. Steady state error stems from the hysteresis rod dipole moment adding to the permanent magnet dipole and creating a misalignment between the spacecraft's total dipole and its pointing axis (Z). This error is apparent after settling of the spacecraft when the angle between the Z axis and GVF is at its smallest. Oscillatory error occurs from the constant change in the orientation and magnitude of the GFV on the orbital path, causing a lag time before alignment. As you increase the volume of hysteresis material, the oscillatory error and settling time decreases, however, this is at the cost of an increase in steady state error. The opposite trade off occurs when lowering the volume of hysteresis material in a spacecraft [5].

The most reliable method for selecting the optimal amount of hysteresis material per Pitch and Yaw axis, is to incrementally increase or lower the volume of hysteresis material per simulation while leaving all other parameters the same. Through iteration, the optimized hysteresis volume per axis was found by characterizing both types of PMAC errors, by analyzing the mean, and amplitudes of axial rates, GFV tracking and time to steady state. Simulation results are shown in Figure 3.9 for values of 0.07, 0.08, 0.09, 0.10, and 0.11 cm^3. Through this process, the optimal amount of hysteresis material for a permanent magnet strength of 0.8 $A \cdot m^2$ was found to be 0.09 cm^3 for the pitch and yaw axes. Referring to Figure 3.9 the hysteresis volumes of 0.07 and 0.08 cm^3 show that the roll axis does not achieve adequate alignment with the GFV in under 72 hours.

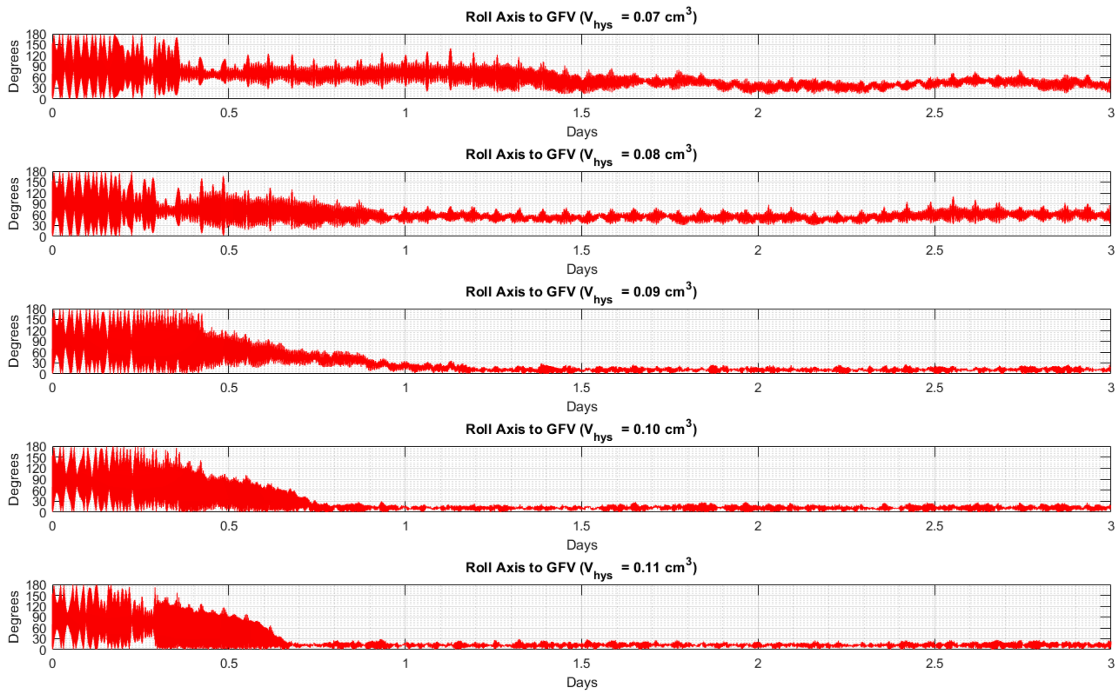

Figure 3.9: Roll axis to GFV for range of hysteresis volumes.

The period of time between deployment and the spacecraft reaching steady state is defined as t_{pd}. To characterize t_{pd}, the running mean of θ_R was taken across 60 minute intervals and once the mean values stabilized to the required value, the spacecraft was deemed to be in steady state. Additionally, the standard deviation and mean of θ were calculated starting from when the spacecraft reached steady state, to the end of the simulation data.

Table 3.3 outlines the results from this analysis, considering both oscillatory and steady state error. The hysteresis volume with the most balanced error results was found to be 0.09 cm^3 with an average roll axis to GFV angle and standard deviation of 10.13° and 5.35°, respectively.

Table 3.3: Hysteresis Selection Results

V_{hys} (cm^3)	$\theta_{roll(ave)}$ (deg)	$\theta_{roll(std)}$ (deg)	t_{pd} (hours)
0.07	34.60	13.32	> 72
0.08	33.54	11.85	> 72
0.09	10.13	5.351	28.81
0.10	10.54	5.463	24.65
0.11	11.37	5.536	18.22

3.2.3 Magnetic Torque Coil Design

Due to the magnetic torque coils having to partially overcome the relatively strong permanent magnet, printed coils on FR4 were unable to reach the required minimum for magnetic moment generation. The design began with one coil for each of the four faces orthogonal to the pitch and yaw axes (X and Y), fastened to the structure, behind the solar panels, with the Z torque coil placed in VIOLET's center module. Through iterative design and part simplification processes, the final design included two torque coils per solar panel assembly, with the Z coil placement remaining the same. Through design iteration, the coil masses were significantly lowered, allowing them to be attached to the solar panels using delrin brackets and epoxies. The -Y face solar panel with attached coils is shown in Figure 3.10. The equation governing the magnetic dipole moment created from a current loop is defined as,

$$m_{coil} = NIA \tag{3.27}$$

where m_{coil} is the magnetic dipole moment of the coil, N is the number of turns of copper wire, I is the current being supplied, and A is the cross sectional area of the coil. Considering the coils mounted to the solar panels, the cross sectional area of the coils was constrained by the dimensions and fasteners present. The cross sectional area was defined as 0.003 m^2 leaving ample room for connectors and harnessing. The supply current, and coil turns, have been defined as 0.03 A and 778 turns, respectively. With a total of 4 coils per pitch and yaw axes, at 0.07 A·m^2, each of the two axes can generate a maximum magnetic moment of 0.28 A·m^2. The roll axis has only one torque coil which has a cross sectional area of 0.003 m^2, supply current of 0.08 A, with 1167 coil turns. Yielding a maximum possible magnetic moment of 0.28 A·m^2. A wire gauge of 37 was selected for all coils, which was chosen to satisfy power requirements [2].

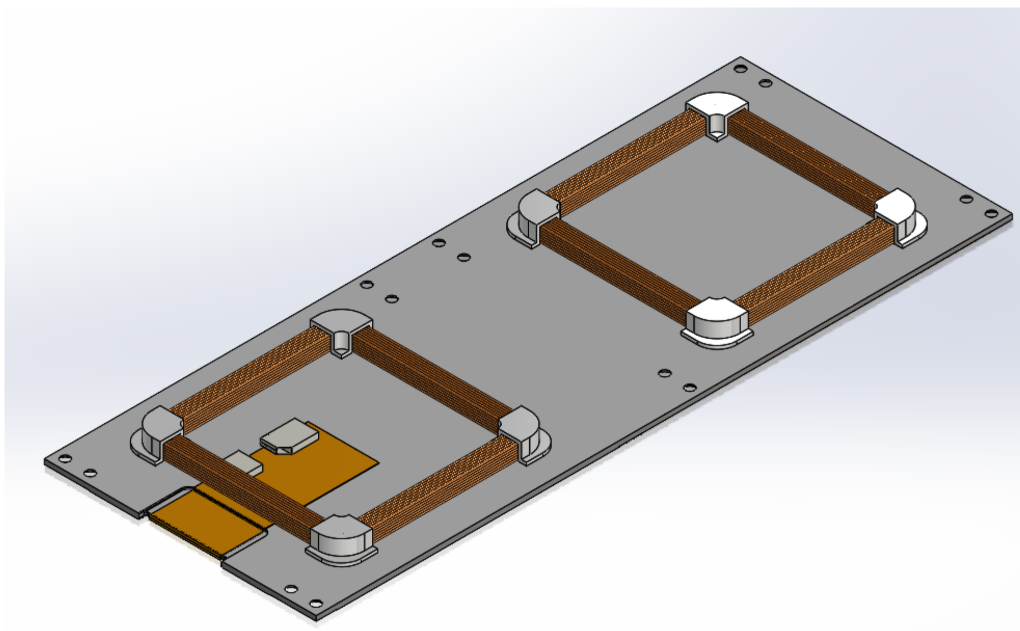

Figure 3.10: +X solar panel with attached torque coils.

3.2.4 Integrated HMAC System Design and Analysis

To model magnetic torque coils in the system, a Simulink block has been developed and added to SNAP's magnetic torque model. This model varies the dipole strengths in each axis after a specified period of time, to emulate the activation of the torque coils. This model can be seen in Figure 3.11. The relevant data for post processing is exported to a .mat file where it is then post processed to determine attitude dynamics behavior, specifically, body-fixed rotation rates, ω, post deployment settling time, t_{pd}, HMAC settling time, t_{ss}, pointing error, e_δ, and time in good pointing at latitude range, $t_{gp,n}$. There is a significant performance trade off with the HMAC system. The Z-axis torque coil can be utilized to null out a portion of the primary magnetic dipole to allow for more pitch and yaw axis control authority, i.e. larger angular deflection from the local GFV. There is however, a point where nulling out the primary magnetic dipole further will result in higher steady state rates of rotation. Higher rates will cause more blur during imaging leading to unusable data. To determine the dipole moment of the coils for each Beta angle, vector addition was used along with selecting symmetric values for the X and Y coils as much as possible. The generated magnetic dipole moment for each body-fixed axis across all Beta angles can be found in Table B.1.

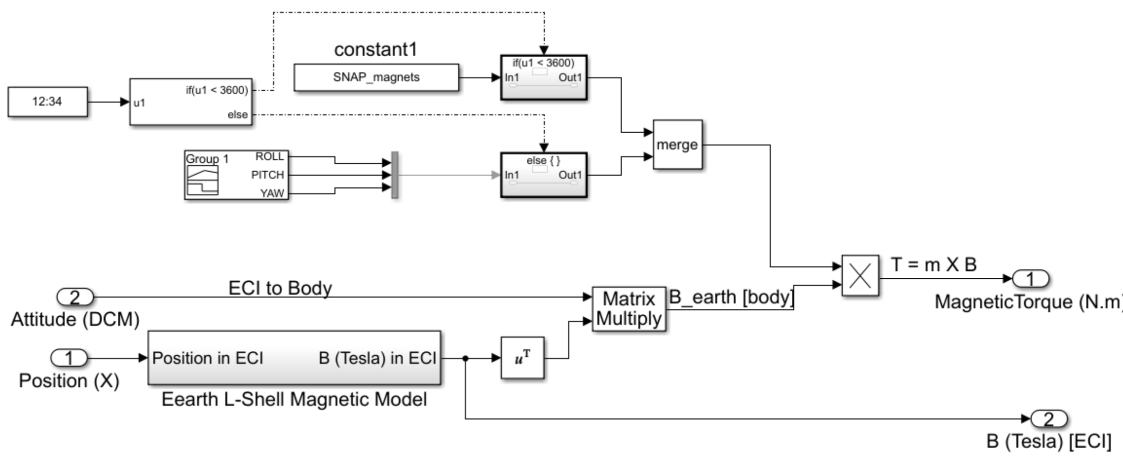

Figure 3.11: SNAP magnetic torque model with torque coil control modification.

Throughout the research and development process for the HMAC system, specific outputs have been analyzed depending on the design phase. Initially, during the preliminary phase, data regarding spacecraft axes relative to GFV, body-fixed rates, environmental torque magnitudes, and settling time were analyzed and catalogued. For the critical design phase and for final research objectives, the data was investigated further to determine optimal Beta angle for a given latitude range. Using a look-up table created from data taken from 30 simulations of Beta angles ranging from 0 to 30°, the best

Beta angle for each latitude range was calculated, as well as frequency and duration at which VIOLET is in a good pointing attitude for SASI imaging. Results from this analysis can be found in Chapter 5.

Chapter 4

Thermal Control System Development Methodology

This chapter will focus on the methodology of design and analysis of the TCS. Some background on modes of heat transfer in LEO and calculation method of important parameters will be discussed. Lastly, the FEM development process will be discussed, along with the mesh sensitivity analysis results.

4.1 Modes of Heat Transfer

This section will review the modes of heat transfer acting on a spacecraft in LEO. With no medium to act as a means for convective heat transfer, only thermal conductance and radiative heat transfer occur in a space environment. The modes of heat transfer applicable to the thermal analysis and design of the VIOLET spacecraft are: solar radiation, albedo radiation, Earth IR radiation and thermal conduction.

4.1.1 Radiation

A nanosatellite in orbit will experience much higher levels of solar radiation, as it is not protected by the Earth's atmosphere. This radiation flux exchanged between two bodies that have a non-zero view factor, can be calculated by the following equation,

$$q = -\sigma \varepsilon_1 \varepsilon_2 A_2 F_{2-1} (T_1^4 - T_2^4) \tag{4.1}$$

where q is the energy exchange rate, σ is the Stefan-Boltzmann's constant, ε_1 is the emissivity of body 1, ε_2 is the emissivity of body 2, A_2 is the surfce area of the second body, F_{2-1} is the view factor, and T_1 and T_2 are the surface temperatures of the bodies. In the case that a spacecraft is surrounded by space the energy exchange rate is,

$$q_L = -\sigma \varepsilon_1 A_1 T_1^4 \tag{4.2}$$

Conversely, for a spacecraft in direct sunlight, the absorbed energy can be found by,

$$q_S = G_S A \alpha \tag{4.3}$$

where G_S is the solar constant, defined as 1362 W/m^2 [17], A is the spacecraft surface area and α is the absorptivity of the spacecraft surface. Albedo radiation is the reflection of light from the sun off the surface of the Earth. This mode of heat transfer has a lower magnitude than direct solar radiation but will still have a significant radiative heating effect on a spacecraft.

As solar radiation reaches Earth, a fraction of the energy is absorbed on the surface and atmosphere. The effect of this is the warming of the planet. This heat is then emitted from the Earth in the form of IR radiation. This mode of radiative heat transfer is the lowest magnitude of the modes described in this section, and will have only a small effect on the thermal behavior of a spacecraft. The radiative heat flux due to IR radiation from Earth can be determined from,

$$q_{IR} = G_{IR} A \alpha \tag{4.4}$$

where G_{IR} is the Earth's infrared (IR) constant, with the average yearly value defined as 250 W/m^2 [17].

4.1.2 Conduction

The generated heat from the radiative modes of heat transfer as well as powered electrical components will transfer via conduction throughout the spacecraft body. Fourier's law of thermal conduction can be used to determine the conductive heat flux between two bodies as,

$$q_x = \left(\frac{kA}{L}\right)(T_1 - T_2) \tag{4.5}$$

where k is the material thermal conductivity, A is the cross-sectional area normal to the direction of heat transfer, L is the length of heat transfer path and T is the temperatures of the bodies taking part in heat transfer.

4.2 Thermal Finite Element Analysis

To characterize the thermal behavior of the VIOLET nanosatellite during flight, a thermal FEM has been developed in the Siemens NX 12 Space Systems Thermal software package. This section will outline the process of meshing spacecraft components, applying thermal couplings, radiative properties, power states, case boundary conditions, and the mesh sensitivity analysis will be reviewed.

4.2.1 Meshing

To create the finite element model, a CAD model of the nanosatellite has been created with simplified model geometry. Generally, thermal FEA methods are not sensitive to element size, therefore model geometry has been simplified to a point where it still reflects the flight hardware. Staying away from complex geometry has allowed for the most possible 2D meshes and a significant reduction in simulation times. Once the geometric model is created, meshes can be applied to the various structural elements, circuit boards and components.

The mesh types applied in this FEA model are 2D and 3D meshes. For simple geometry such as a circuit board or solar panel, 2D meshes suffice, as the two-dimensional mesh can easily be extruded to the thickness of the component. However, with more complex geometry of the structure and SASI optics, 3D meshes were required. As recommended by the CSA [25], tetrahedral elements are the most effective choice for nanosatellite structures and were selected as the element type for the 3D meshes contained in the model. Siemens NX Space Systems Thermal utilizes the finite volume method (FVM) as well as the finite difference method (FDM) for discretizing partial differential equations and solving for element and node temperatures, respectively. Using this method, the heat transfer properties are stored and propagated through the elements and nodes contained in the mesh model. The fully meshed model, with solar panels hidden, is shown in Figure 4.1.

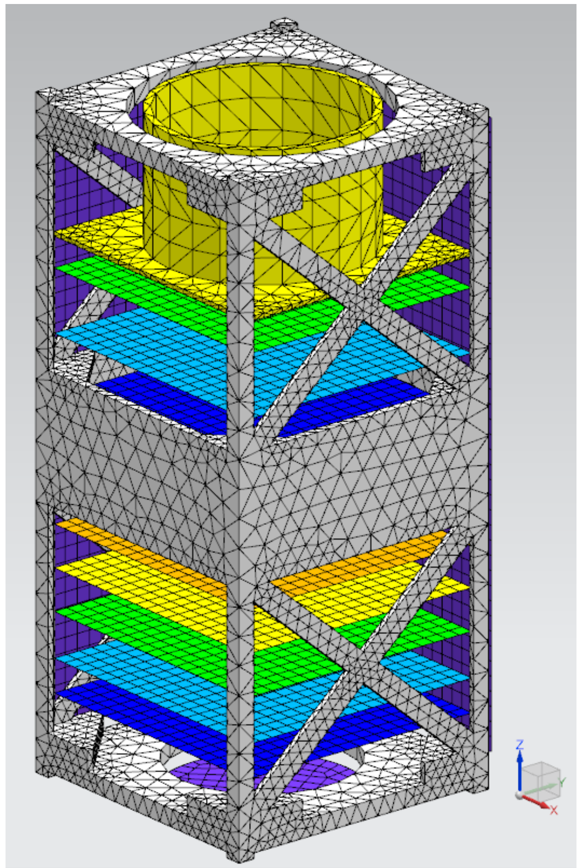

Figure 4.1: VIOLET thermal FEA meshed model.

4.2.2 Thermal Couplings

Upon defining the thermal conductivities of the various materials in the VIOLET assembly, the resistivities of the interfaces, or joints could be found. The thermal resistance for heat transfer between two defined bodies can be found as,

$$R_{series} = \frac{L_1}{AK_1} + \frac{L_1}{AK_2} \tag{4.6}$$

$$R_{parallel} = \left[\frac{AK_1}{L_1} + \frac{AK_2}{L_2} \right]^{-1} \tag{4.7}$$

These equations were utilized to determine the resistivity of critical heat paths throughout the spacecraft by separating the calculations into parallel and series joints. The material thermal conductance values can be found in Table 4.1.

Table 4.1: Material Thermal Conductances

Component	Material	Thermal Conductivity [W/mK]
Structure	6061-T6 Aluminum	157
Spacers	6061-T6 Aluminum	157
Tie rods	18-8 Stainless steel	16
Header pins	6061-T6 Aluminum	157
PCB	Copper	300
	FR4	0.25
Solar Panel	Silicon PV cell	150
	Ethylene vinyl acetate	0.35
	FR4	0.25
	Copper	300
GNSS Antenna	Polycarbonate	0.2
	Copper	300
	Zamak White Metal	113

Utilizing equations 4.6 and 4.7 the total thermal resistance was calculated for each thermal coupling throughout the FEA model. MS Excel was used to develop a modifiable spreadsheet, as the iterative design of the thermal control system progressed. The calculated resistances can be found in Table 4.2.

Table 4.2: Sub-System Conductive Thermal Paths

Joint Location	Header Resistance (K/W)	Interface Joint Resistance (K/W)
Panel to Structure	-	0.919
GNSS antenna to -Z	-	1.21
-Z to GRIPS	0.683	3.34
GRIPS to OBC	0.621	3.21
OBC to TRXVU	0.869	3.72
TRXVU to SCP	0.807	3.59
SCP to LMB	0.807	3.59
LMB to SASI-C	0.994	3.59
SASI-C to ZTB	1.06	2.70
ZTB to EAOP	0.651	2.39
EAOP to BATT	1.24	0.956
BATT to EPS	-	0.956
EPS to SASI-O	0.66	7.19
SASI-O to +Z	-	7.58

4.2.3 Radiative Surfaces

As radiation is the only mode of heat transfer in which a spacecraft thermally interacts with the space environment, it is critical to properly define the thermo-optical properties of the surfaces taking part in that interaction. The components of VIOLET which have significant view factors with the space environment include; the four solar panels, Global Navigation Satellite System (GNSS) antenna, SASI imager, both Z faces and the deployment rails. The thermal emissivity and absorptivity values used in the FEA model are shown in Figure 4.3.

Table 4.3: Thermo-Optical Properties

Material	Emissivity	Absorptivity
Black anodized 6061-T6	0.86	0.79
Machined 6061-T6	0.39	0.31
FR4	0.9	0.65
Solar cells	0.85	0.85
Silver teflon tape	0.9	0.15

4.2.4 Analysis Cases

To ensure the thermal control system of VIOLET will be capable of keeping all subsystems within their acceptable temperature ranges, WCC and WCH simulations have been conducted. At least one of each will be necessary to ensure compliance with the mission's thermal requirements. In order to adequately simulate radiative heat transfer for a spacecraft in orbit around Earth, it is important to define the orbital parameters. These parameters will dictate the magnitude and duration of solar, Earth infrared and albedo flux, as well as how long VIOLET will be in eclipse. The parameters related to how much thermal radiation an orbiting spacecraft will experience is directly dependent on how close the Earth is to the sun. The CSA CubeSat Thermal Simulation Guidelines [25] outline the most important parameters which need to be defined for each of the thermal simulation cases in the NX Space Systems Thermal. The dynamic behavior has been simplified to having the roll axis be north pointing with a rate of 1 deg/s, which best emulates PMAC actuation. The orbital altitude, which will decrease over the mission, has a significant effect on orbital heating and cooling. With a lower altitude the Earth's atmosphere will absorb more solar flux and the spacecraft will see less radiative heating. The opposite is true with higher orbital altitudes. The values selected for solar flux, albedo, and infrared flux were defined from values obtained in the Spacecraft Thermal Control Handbook [26]. The orbital parameters for both WCH and WCC cases can be found in Table 6.1.

4.2.5 Power States

The power states of VIOLET's sub-systems were generated in collaboration with the electrical power system team to ensure the most accurate representation possible of conditions relating to highest and lowest power states during the mission. For both cases, the simulation begins at deployment, after which there is a 30 minute period where the satellite is powered off due to NASA requirements, relating to interference with ISS systems.

The WCC power states were defined over a period of 24 hours, which have VIOLET in safe hold mode, with minimum power generation from sub-systems. The power states for WCC are constant as the satellite is in its lowest power generating state for the duration of the simulation. For WCC, all sub-systems can be assumed to be in safe mode after the initial 30 minute timer.

The WCH power states, also defined over 24 hours, have VIOLET in normal operations, accounting for scientific data acquisition, ADCS mode, and most critically, communications mode. WCH however, takes into account timings of modes during normal operation and thus utilizes time varying thermal loads. This is accomplished by importing .csv data including time and power data across 24 hours. The two communications modes have been separated into COMMS-M (mission communications) and COMMS-A (amateur communications). The communication system's thermal loads for COMMS-M are tied to the period of time and frequency in which the satellite is in range of the New Brunswick ground station, where COMMS-A communicates over longer periods with multiple amateur ground stations. The mode timings for WCH are shown in Table 4.4, along with the thermal loads of each sub-system per mode in Table 4.5.

Table 4.4: Worst Case Hot Operational Mode Timings

Mode	Timing (min)
COMMS-M	30-488
ADCS	489-670
SASI	671-760
GRIPS	761-968
COMMS-A	969-1440

Table 4.5: Thermal Loads Per Operational Mode

	Operational Modes (W)					
Sub-System	Safe Mode	COMMS-M	COMMS-A	ADCS	SASI	GRIPS
GRIPS	0	0	0	0	0	2.8
OBC	0.2	0.2	0.2	0.2	0.2	0.2
TRXVU	0	4	4	0	0	0
LMB	0	15	0	0	0	0
SCP	0	3.88	3.88	0	0	0
SASI-C	0	0	0	0	1.12	0
EAOP	0	0	0	2.3	2.3	0
BATT	2	0.5	0.5	0.5	0.5	0.5
EPS	0.1	1.5	1.5	1.5	1.5	1.5
SASI-O	0	0	0	0	0.37	0

4.3 Thermal Finite Element Model Validation

Due to the current inability to conduct thermal vacuum testing to validate the thermal FEA model, various analyses have been completed, including a mesh sensitivity analysis and iterative analytical calculations. This has been done to ensure the model is behaving as expected. This section will go over these analyses and their results.

4.3.1 Mesh Sensitivity Analysis

To verify that mesh size does not affect the FEA results, a mesh sensitivity analysis was conducted separately for conductive and radiative heat transfer. For the conductive analysis, a simple case of two PCBs conducting heat through tie-rod, spacer thermal couplings was developed including 3 cases with varying 2D element sizes. The standard mesh size for 2D elements in the VIOLET model is 5 mm, where the coarse and fine element sizes were defined as 20 mm and 1.25 mm, respectively. Figures 4.2, 4.3, and 4.4 show the different models with varying element sizes.

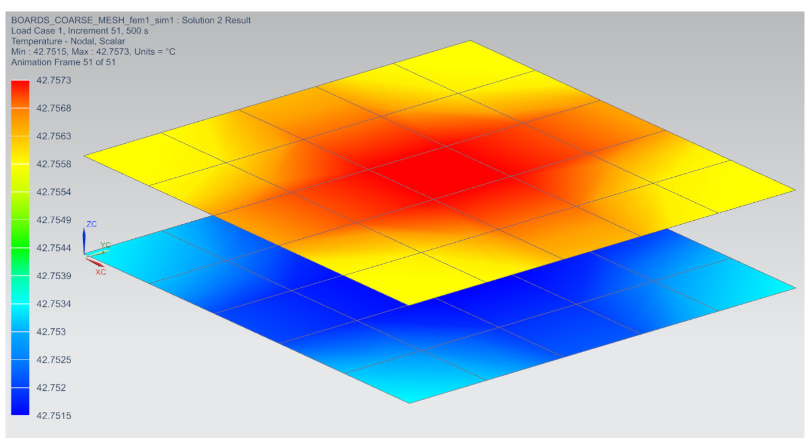

Figure 4.2: Coarse element size mesh temperature gradient at end of simulation.

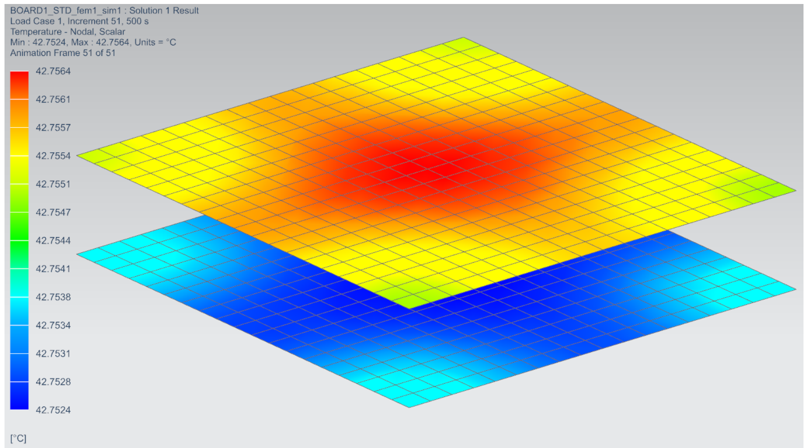

Figure 4.3: Standard element size mesh temperature gradient at end of simulation.

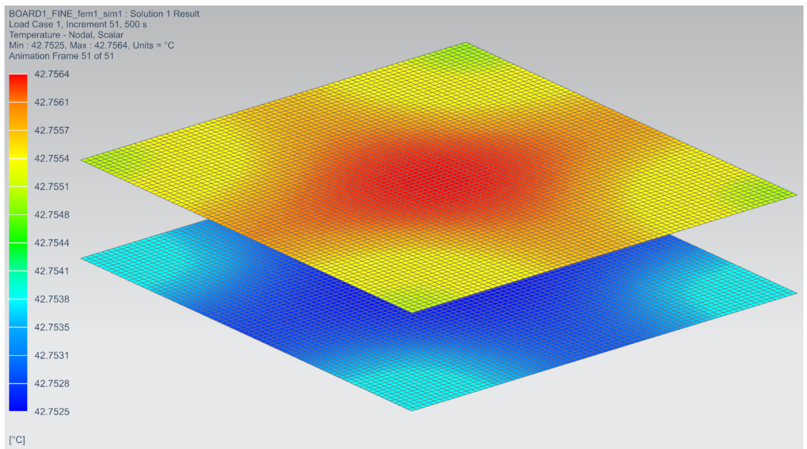

Figure 4.4: Fine element size mesh temperature gradient at end of simulation.

The +Z PCB, also defined as 'PCB 1', was given a sinusoidal thermal load over a total analysis duration of 500 seconds. The amplitude and frequency of the load is 0.05 W and 0.002 Hz, respectively. Additionally, the initial temperature of the two PCBs was set to $10°C$. The time varying thermal load can be found in Figure 4.5.

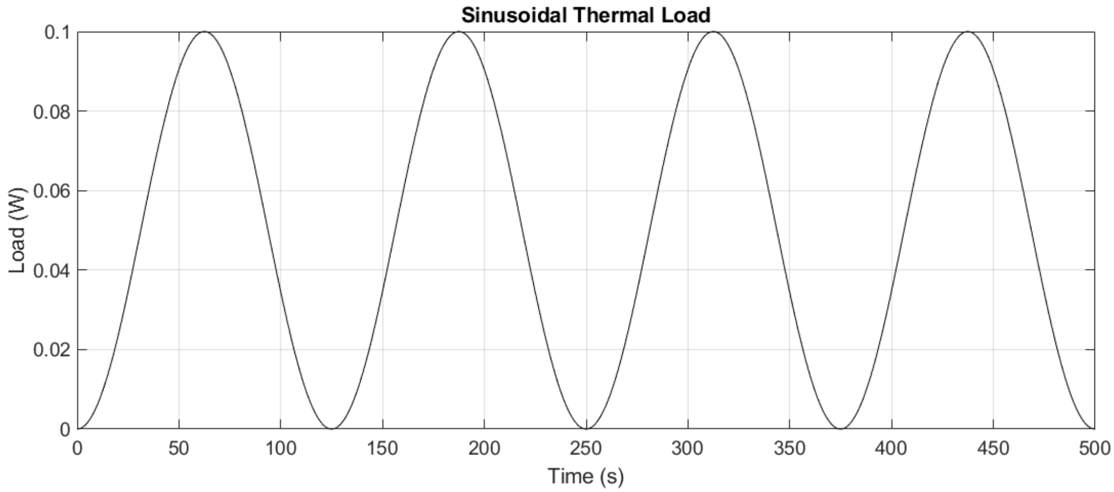

Figure 4.5: Sinusoidal thermal load applied to conductive mesh models.

The purpose of the sinusoidal thermal load was to better understand the heat transfer between the two PCBs during a phase of transience. The load set as a relatively low value such that the temperature curves would not rapidly trend upwards, as the two meshes are a closed system, not transferring heat to the environment. As the load cycles between 0 and 0.1 W for the three analysis cases, the temperature curves can be examined to determine if the rates of heat transfer are sensitive to element size. To ensure consistent results, a node on each PCB was chosen in the same location for the three cases. The thermal curves for each analysis case and the individual PCB's, is shown in Figure 4.6.

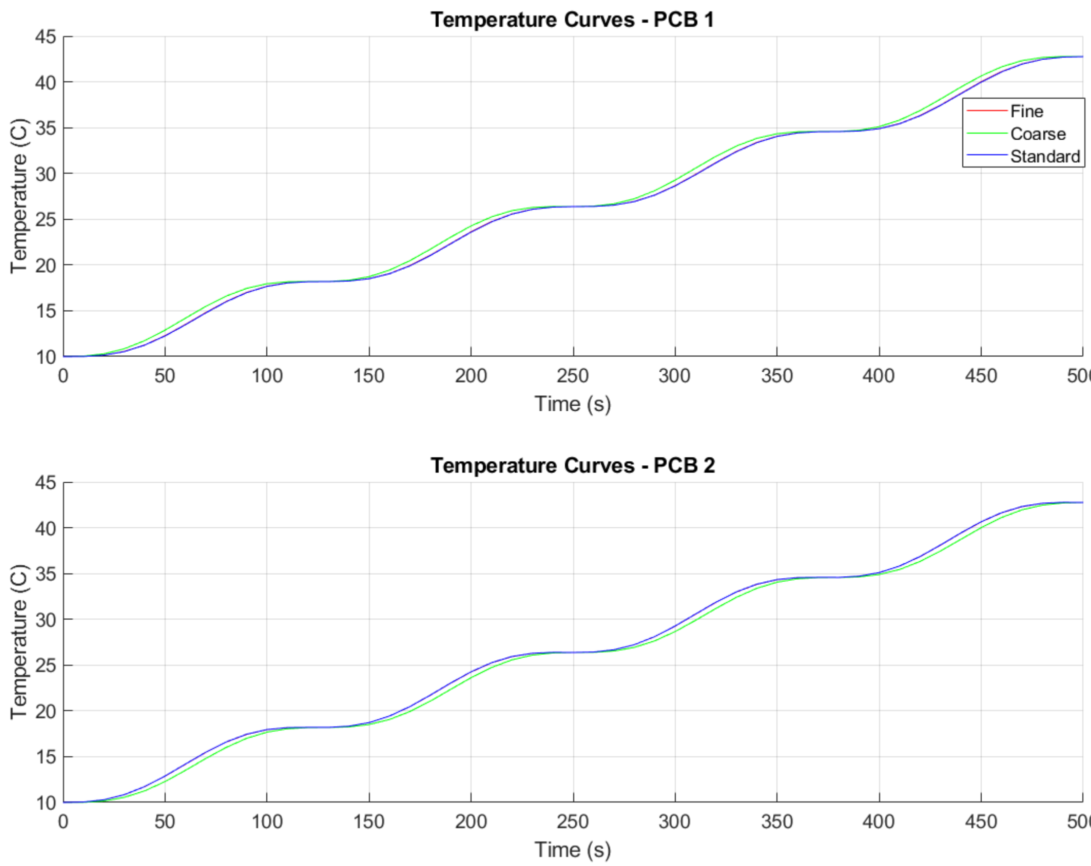

Figure 4.6: Standard element size meshes at final time step.

Throughout the course of the analysis, the effect of the cycling load can be seen as the temperatures of both boards increase. As the two PCBs are a closed system, their temperature momentarily stabilizes before increasing due to the load reaching its peak value, at four instances in the analysis. As the curves for both PCBs across the analysis cases match closely, the conclusion to be made that mesh sensitivity for two conducting 2D meshes will not impact simulation results. This also validates the selection of a 5 mm element size for 2D meshes in the thermal FEA.

Similar to the conductive analysis, the radiative mesh sensitivity analysis includes 3 cases. Each of which has matching initial conditions and parameters, with the exception of 3D element size. Additionally, the model geometry defined such that it matched a 2U CubeSat. The goal of this analysis is to verify that the NX Space Systems Thermal orbital heating model is not sensitive to element size. The standard 3D element size in the VIOLET model is 10 mm, leading to the fine and coarse sizes being defined as 5 mm and 20 mm, respectively. Figures 4.7, 4.8, and 4.9 show the different models with varying element sizes.

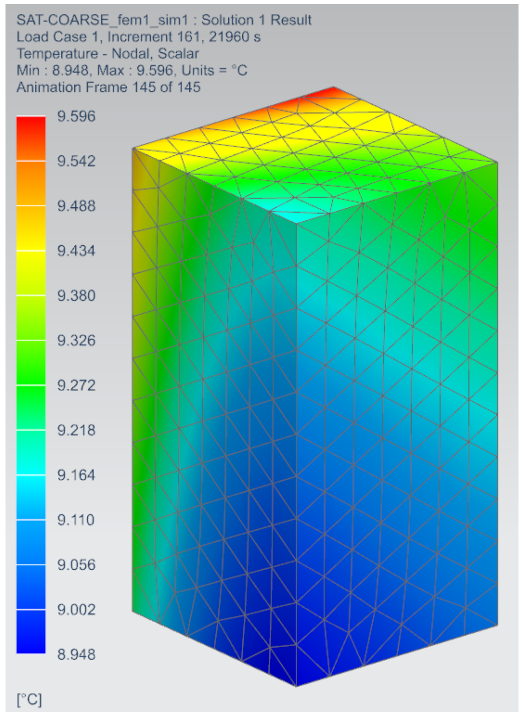

Figure 4.7: Coarse element size mesh temperature gradient at end of radiative simulation.

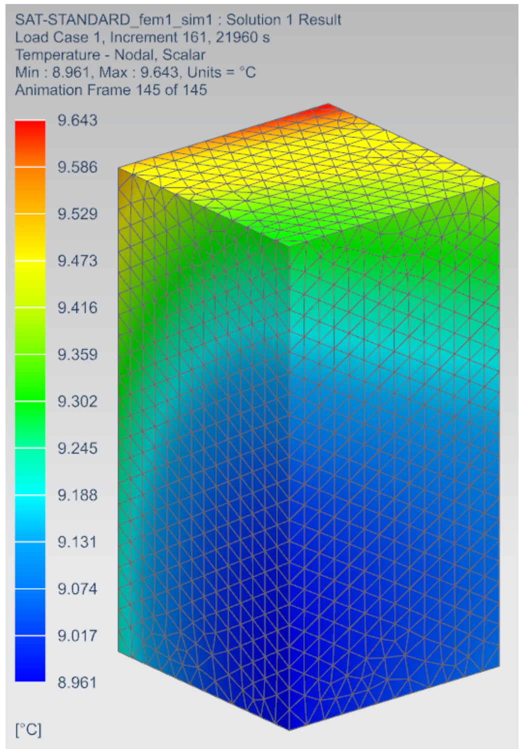

Figure 4.8: Standard element size mesh temperature gradient at end of radiative simulation.

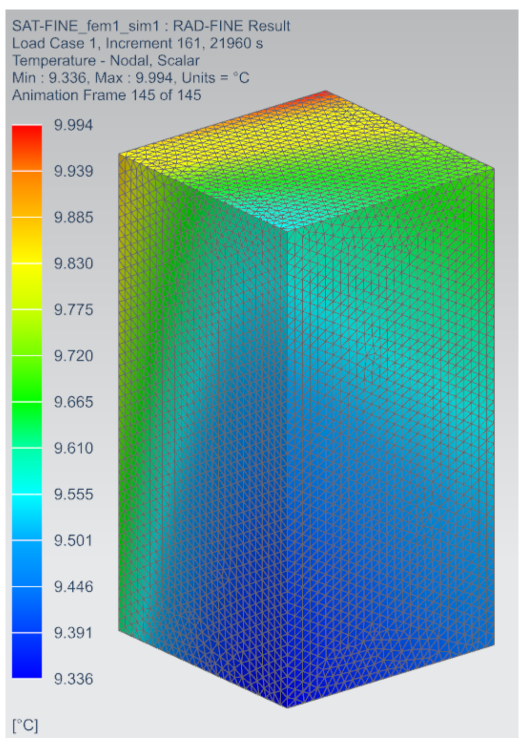

Figure 4.9: Fine element size mesh temperature gradient at end of radiative simulation.

The absorptivity and emissivity of the radiating surfaces were chosen to be 0.5 and 0.72, respectively, with the material being defined as Aluminum 6061. Since the only heat load in these analyses was due to solar, IR and albedo flux, the values were chosen so that the model's temperature curves would oscillate symmetrically about 10°C.

A node on each of the positive X, Y, and Z faces was chosen on each case model, and the temperature data was exported to generate the curves shown in Figure 4.10. Upon inspection of the curves, it can be seen that they compare favorably, with minimal variation across time. This leads to the conclusion that the orbital heating model is not sensitive to element size, verifying the choice of 10 mm 3D element size.

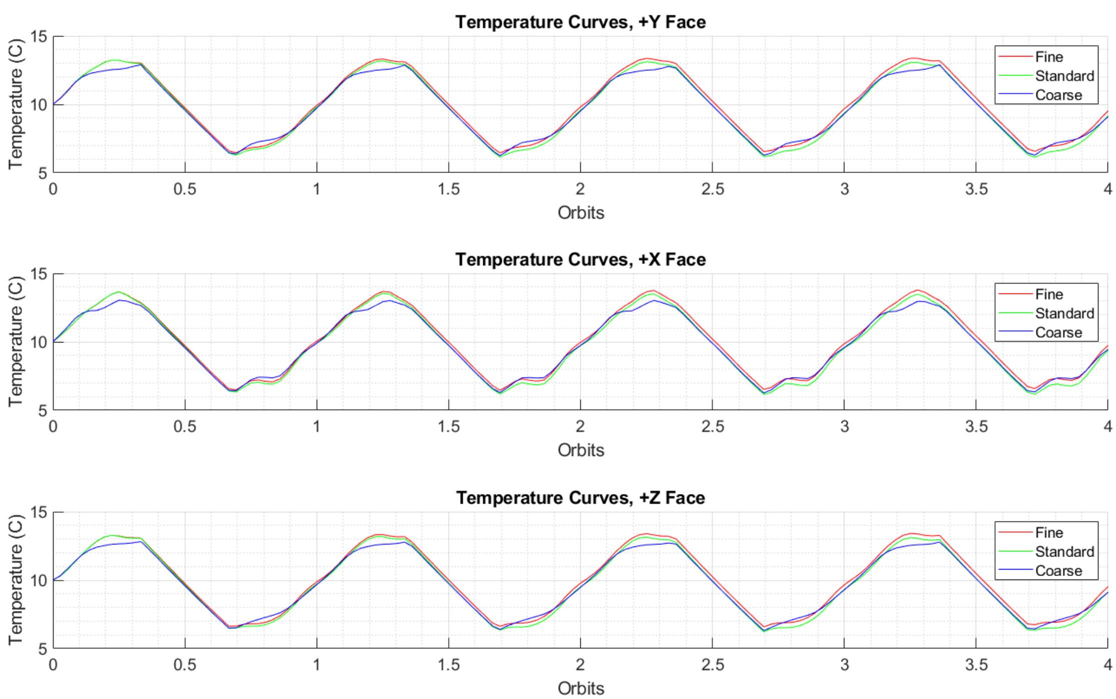

Figure 4.10: Temperature curves across radiative analysis cases.

4.3.2 Analytical Conduction Analysis

As the conductive mesh sensitivity analysis is a simple case compared to the full FEA model, a set of equations have been derived to analytically model this transient conduction between two PCBs. The purpose of this analysis is to verify at a high level that the methods used to simulate the thermal behavior of VIOLET are correct. The temperature of each board has been calculated at each time step of five seconds for a total duration of 500 seconds, to enable comparison of results to the conductive mesh sensitivity analysis. Additionally, all relevant initial and boundary conditions used in the sensitivity analysis were also utilized in the analytical model.

The approach to deriving the set of equations was to utilize an energy balance, where the temperature of PCB1 would be calculated based on initial conditions, followed by the temperature of PCB2. The instantaneous power stored in PCB1 can be defined as [27],

$$\dot{E}_{st,1} = \dot{E}_{gen} - \dot{E}_{out} \tag{4.8}$$

where $\dot{E}_{gen}$, in Watts, is the sinusoidal load shown in Figure 4.5, and $\dot{E}_{out}$ is the power moving through the four tie-rod spacer joints from PCB1 to PCB2, which can be defined as,

$$\dot{E}_{out} = \frac{T_{1,n} - T_{1,n-1}}{R_{eq}} \tag{4.9}$$

where T_1 is the temperature of PCB1 at the current and previous time steps, and R_{eq}, is the equivalent resistance between the two PCBs, calculated from equations 4.6 and 4.7. To account for the stored power in PCB1, $\dot{E}_{st,1}$ can defined as [27],

$$\dot{E}_{st,1} = \frac{dT}{dt}\rho V c_p \tag{4.10}$$

where ρ, V, and c_p are the density, volume and specific heat of the PCBs, respectively. From these equations the temperature of PCB1 can be found for the current time step as,

$$T_{1,n} = \left[\dot{E}_{gen} - \left(\frac{T_{1,n} - T_{1,n-1}}{R_{eq}}\right)\right]\left[\frac{t_n - t_{n-1}}{\rho V c_p}\right] + T_{1,n-1} \tag{4.11}$$

Upon solving for $T_{1,n}$ the focus can then be placed on PCB2, where its energy balance is defined as,

$$\dot{E}_{out} = \dot{E}_{in} = \dot{E}_{st,2} \tag{4.12}$$

where the power into PCB2, $\dot{E}_{in}$ is equal to the power out of PCB1, which is also equal to the stored power in PCB2, $\dot{E}_{st,2}$. From this, the solution for the temperature of PCB2 at the current time step is defined as,

$$T_{2,n} = \left(\frac{T_{1,n} - T_{1,n-1}}{R_{eq}}\right)\left(\frac{t_n - t_{n-1}}{\rho V c_p}\right) + T_{2,n-1} \tag{4.13}$$

To solve for the temperatures of the two PCBs at each time-step, equations 4.11 and 4.13 were integrated into a while loop in MATLAB. The results comparing the average temperatures for all mesh sizes in the conductive mesh sensitivity analyses and the analytically solved temperatures is shown in Figure 4.11.

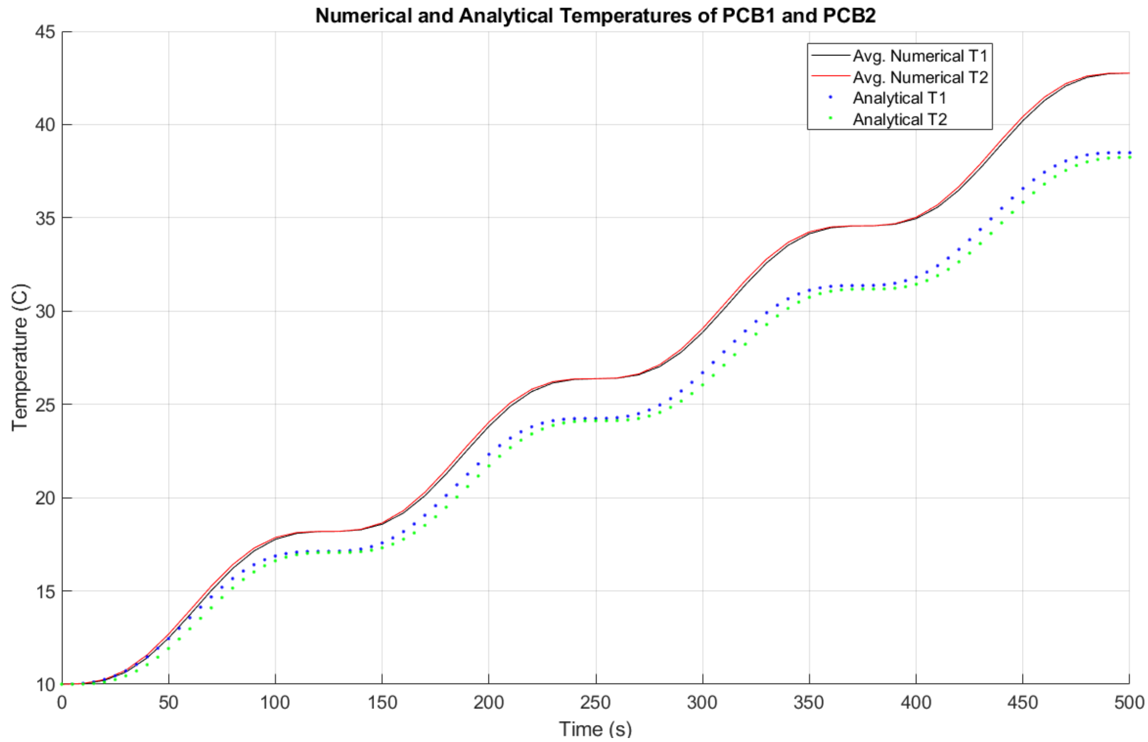

Figure 4.11: Temperatures seen in PCB1 and PCB2 over 500 seconds for both numerical and analytical analyses.

The solid lines are the temperature curves for PCB1 and PCB2, which are each an average of the temperatures seen over 500 seconds for coarse, standard and fine mesh sizes. Additionally, the dotted curves describe the analytically calculated temperatures of the PCBs. Figure 4.11 gives some valuable information related to the similarities and differences found in results from comparing numerical and analytical results. Each set of curves show a short temperature lag between the two PCBs. This can be explained by the temperatures in the mesh sensitivity analysis being from one node from each PCB, where the temperatures in the analytical calculation are an approximate average for each PCB. Since the nodes chosen in the sensitivity analysis were at "hot" locations, the linearly increasing difference is therefore expected between the two analyses.

Chapter 5

Attitude Control System Analysis Results

5.1 Post-deployment Analysis

As discussed in Chapter 3, SNAP takes user inputs to define physical, magnetic, and orbital properties to simulate the attitude dynamics of a nanosatellite over a specified period of time. The passive de-tumble phase occurs after the spacecraft is deployed from the NRCSD, interfaced with the ISS. Upon deployment, the spacecraft will have an initial rate of rotation about each axis, caused by axial moments of inertia. Simulating the attitude dynamics during this phase is critical to ensure the optimal amount of hysteresis material is used and also to understand and quantify settling time and dynamic behavior. The first results to be analysed is the de-tumble phase simulation data, for which the initial conditions can be seen in Table 5.1, where body-fixed axis vectors are in order of roll (Z), pitch (Y), and yaw (X). Due to the unknown initial body-fixed rates upon deployment from the NRCSD, three different simulations were run with initial rates about the roll, pitch, and yaw axes of 2, 4, and 6 deg/s, with the last being defined by NanoRacks as the maximum possible initial rates that may be seen upon deployment [2].

Table 5.1: Initial Conditions for Post-deployment SNAP simulations.

Parameter	Value	Unit
TLE	ISS (ZARYA)	-
Solver	Ode45	-
MMOI	[0.0055 0.0212 0.0212]	kg·m^2
Mass	3.6	kg
Magnetic moment	[0.8 0 0]	A·m^2
Hysteresis volume	[0 0.09 0.09]	cm^3
Hc	0.96	A/m
Br	0.35	Tesla
Bs	0.74	Tesla
Duration	4	days

As the spacecraft tumbles at the beginning of the simulation, the permanent magnet is constantly applying a torque against the GFV, and coupled with the hysteresis damping torques, slowly brings the spacecraft into acceptable alignment with the local GFV. Considering the case with the highest initial body-fixed axial rates (6 deg/s), the mean of the roll axis pointing accuracy upon reaching steady state, was found to be 10.0°, with a standard deviation of 5.3° degrees. With the use of the 0.8 A·m^2 permanent magnet, the spacecraft reaches steady state after an average of 33.5 hours (1.4 days), which is significantly less than the mission requirement of 7 days. Figure 5.1 shows the simulated roll rates of VIOLET for each of the simulations of varying initial body-fixed axial rates. The time it takes to reach post-deployment steady state is a minimum of 29.6 hours, with the maximum being 37 hours.

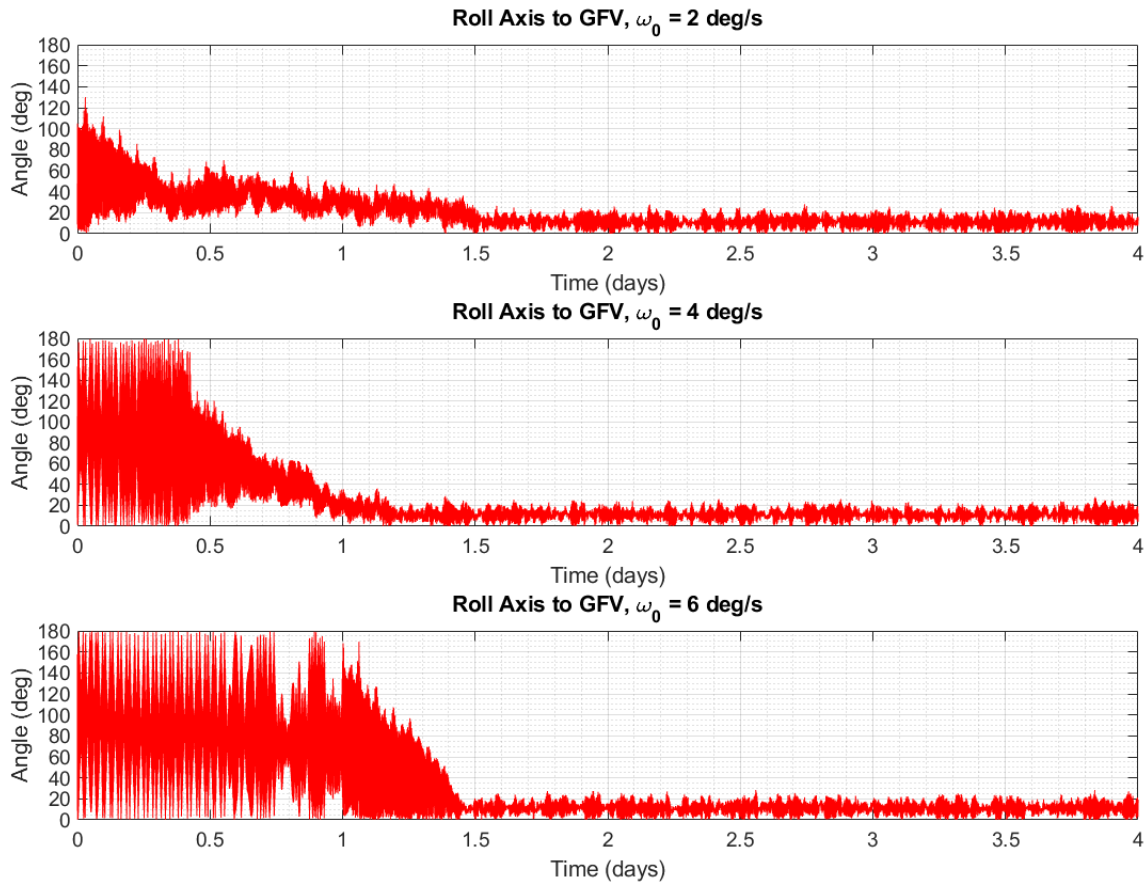

Figure 5.1: VIOLET body-fixed roll axis relative to GFV from post-deployment simulations with varying initial body-fixed axial rates.

Figures 5.2, 5.3, and 5.4 show the body-fixed axial rates of the spacecraft, for initial rates of 2, 4, and 6 deg/s, respectively. Once the spacecraft reaches post-deployment steady state, the only moments acting on it are the environmental disturbance torques, which the PMAC system has been designed specifically to overcome. Thus, the rates of rotation and pointing accuracy are very predictable with use of the PMAC system as there are no other significant moments acting on the system.

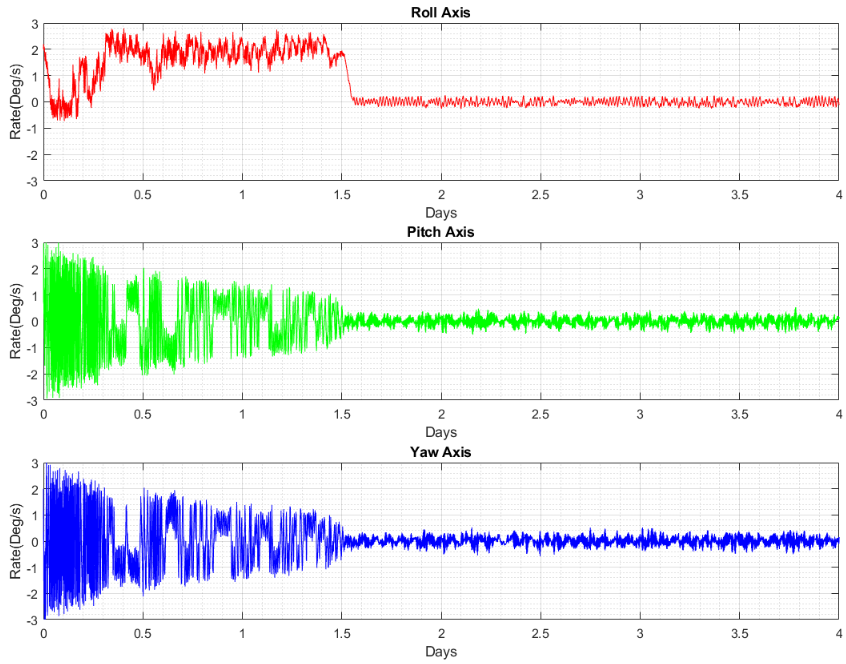

Figure 5.2: VIOLET axial rates from post-deployment simulations with initial body-fixed rates of 2 deg/s.

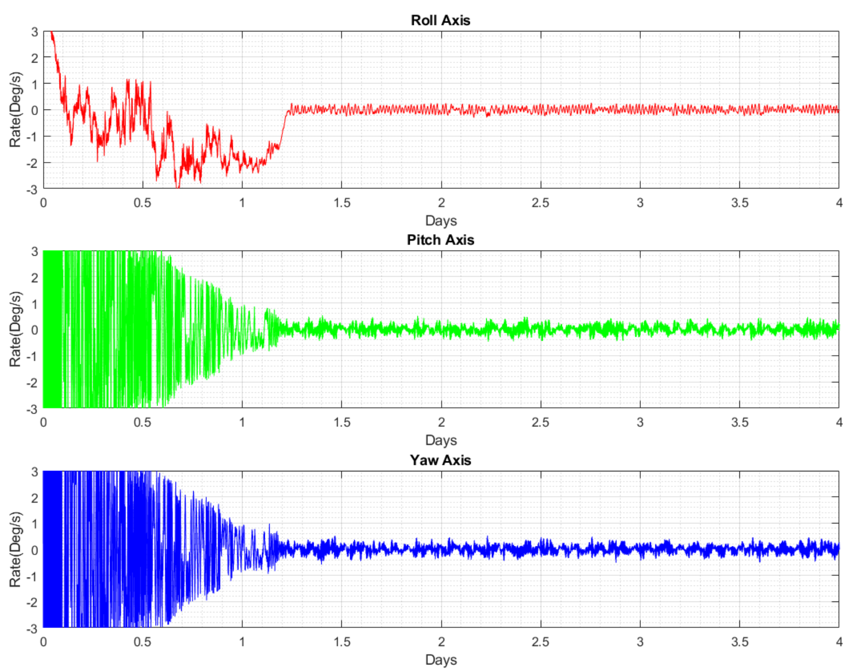

Figure 5.3: VIOLET axial rates from post-deployment simulations with initial body-fixed rates of 4 deg/s.

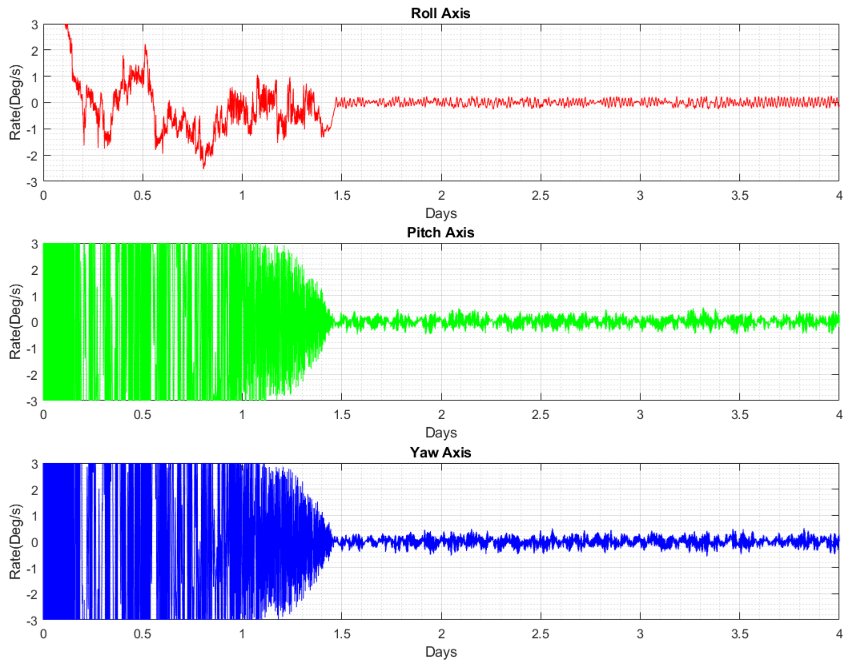

Figure 5.4: VIOLET axial rates from post-deployment simulations with initial body-fixed rates of 6 deg/s.

Through analysis of results from the 3 post-deployment simulations, it was found that initial rates of rotation ranging from 2 to 6 deg/s had little effect on time to steady state as well as steady state performance. Results confirming this conclusion can be found in Table 5.2, where there are minimal variation in rates, pointing accuracy, and time to steady state.

Table 5.2: PMAC Post Deployment SNAP Simulation Results

ω_0 (deg/s)	θ_{ave} (deg)	θ_{std} (deg)	ω_{ave} (deg/s)	ω_{std} (deg/s)	$t_{ss}(hours)$
[2 2 2]	[10.0 90.2 88.2]	[5.1 7.9 7.7]	[0.24 0.53 0.52]	[0.10 0.17 0.17]	36.5
[4 4 4]	[9.90 88.1 90.5]	[4.9 7.6 7.8]	[0.28 0.51 0.53]	[0.11 0.17 0.17]	29.6
[6 6 6]	[10.0 89.1 89.6]	[5.3 7.8 8.0]	[0.31 0.55 0.56]	[0.11 0.17 0.18]	37.0

5.2 Steady State Attitude Control Analysis

During VIOLET's mission, the HMAC system will be utilized to change the orientation of the principal magnetic dipole vector relative to the body-fixed roll axis, incrementally changing the spacecraft's attitude relative to the local GFV until the spacecraft is in an appropriate attitude for imaging. Once the spacecraft achieves the appropriate attitude for imaging at a defined latitude range, there will be a number of opportunities for imaging throughout the period of the simulation. The periods in which VIOLET is able to image is described as time in good pointing (TGP) which is defined as the period of time at which the spacecraft imaging axis is pointed at a -12° inclination within +/-5° error. The distribution of time in good pointing shows the amount of instances in which the spacecraft is in this state as well as the duration.

5.2.1 Passive Magnetic Attitude Control Performance

As PMAC is the foundation of the HMAC system, and its primary purpose being to allow the SASI imager to collect data of Earth's ionosphere, it is important to characterize its performance in achieving adequate attitude for imaging. To ensure results are not sensitive to epoch, a 4 day simulation was conducted and split into 24 hour periods. Each 24 hour data set was analyzed to determine consistency of results. This analysis showed under 10% of variation in total time in good pointing attitude across each of the four 24 hour data sets, which was deemed acceptable to allow for the selection of any data set for inclusion in the PMAC performance analysis. The initial conditions of the simulation can be found in Table 5.3.

Table 5.3: Initial Conditions for PMAC Steady State SNAP simulation.

Parameter	Value	Unit
TLE	ISS (ZARYA)	
Solver	Ode45	
MMOI	[0.0055 0.0212 0.0212]	$kg{\cdot}m^2$
Mass	3.6	kg
Magnetic moment	[0.8 0 0]	$A{\cdot}m^2$
Hysteresis volume	[0 0.09 0.09]	cm^3
Hc	0.96	A/m
Br	0.35	Tesla
Bs	0.74	Tesla
Duration	24	hours
Initial rates	[0.3 0.5 0.5]	deg/s

The inclination of Earth's magnetic field is closest to -12° near the equator. Figure 5.5 visualizes this as the data points show the spacecraft in good pointing attitude using only passive magnetic components. Additionally, it is important to note that true and magnetic north are not aligned. This misalignment presents itself in the ground track projection as a sine wave. If true and magnetic north were aligned, the ground track would resemble a horizontal line. Figure 5.5 also shows the distribution of time in good pointing for the duration of a 24 hour period, where there is a total of 14 imaging opportunities. Additionally, imaging opportunities under 20 seconds are not considered as the SASI imager requires exposure times up-to eight seconds due to its narrow-band optical filter. Knowing that the orbit will intersect the effective PMAC latitude range of -23° to 9° approximately 31 times over a 24 hour period. From this, the probability at which VIOLET will be in good pointing attitude has been found to be 45.2%.

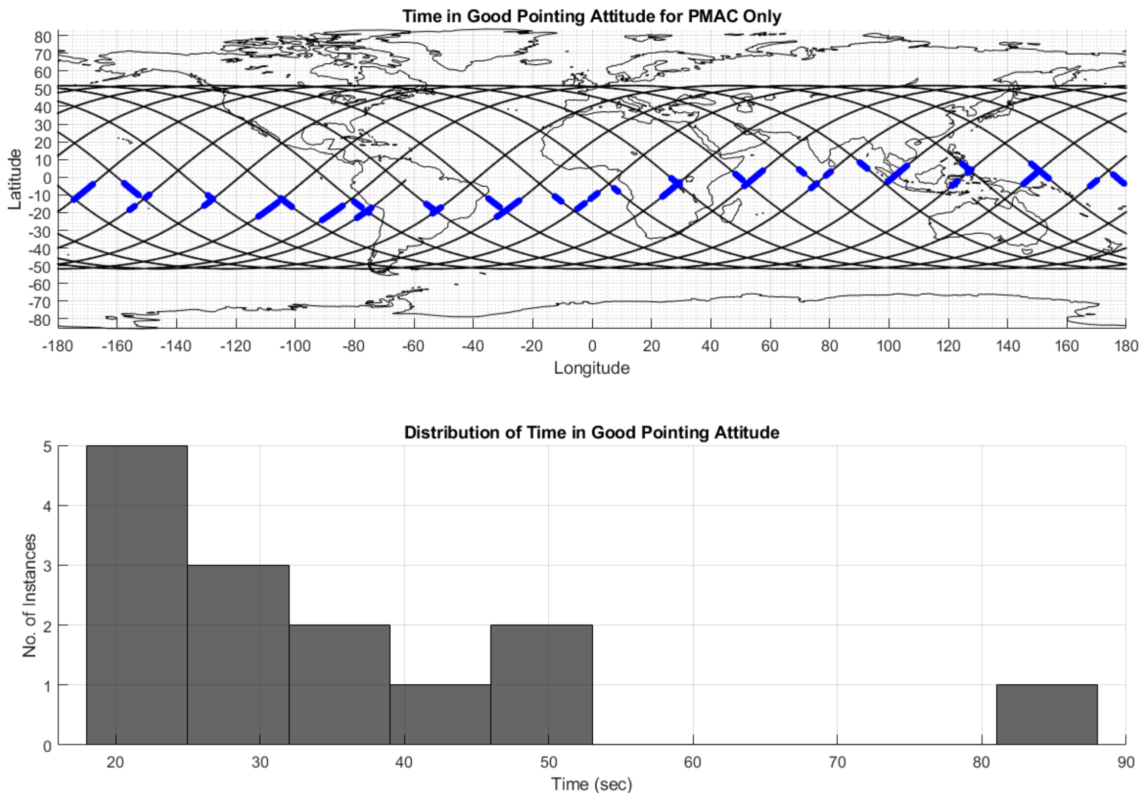

Figure 5.5: Ground track projection and distribution of time in good pointing for SASI imaging at full latitude range with only passive magnetic actuation.

5.2.2 Hybrid Magnetic Attitude Control Performance

SNAP simulations were conducted for Beta angles ranging from 1° to the maximum of 30°, at one degree increments. The data compiled from these 30 simulations was processed using a custom MATLAB post processing script found in Appendix B. Data sets saved from each simulation, including time, latitude, longitude, and e_δ were then formatted into a look up table. The look up table was then processed to determine the Beta angle yielding the best distribution of times in good pointing for various latitude ranges, from -30 to 30° latitude in 10° increments. This analysis produced seven Beta angles, each of which are the best choice for imaging at a specific latitude range. latitude ranges as well as corresponding best Beta angles can be found in Table 5.4. Additionally, the magnetic moment of each body-fixed axis per Beta angle can be found in Table B.1, in Appendix B.

Table 5.4: Defined Latitude Ranges used in HMAC Analyses.

Parameter	Latitude Range (deg)	Optimal β (deg)
LR1	-40° to -30°	30
LR2	-30° to -20°	25
LR3	-20° to -10°	15
LR4	-10° to 0°	6
LR5	0° to 10°	11
LR6	10° to 20°	22
LR7	20° to 30°	29

To produce results that reflect real mission cases it was determined that the best course of action was to analyze the period and frequency of time in good pointing at specific latitudes ranging from -40° to +30°, in 10° increments. Output plots were generated to show the ground track projections of the period and location in which VIOLET is simulated to be in a good pointing attitude for imaging. The initial conditions for each of the HMAC simulations can be found in table 5.5.

The data compiled from the 7 cases show the effectiveness of the HMAC system across VIOLET's orbits over a 24 hour period. From the data, conclusions can be made related to what configurations will be applicable for use in a real mission scenario. To simplify the following discussion, only the cases deemed adequate for SASI mission operations will be considered and discussed. The criteria for this selection will be described further in this sub-section.

Table 5.5: Initial Conditions for HMAC Steady State Analysis SNAP Simulations.

Parameter	Value	Unit
TLE	ISS (ZARYA)	-
Solver	Ode45	-
MMOI	[0.0055 0.0212 0.0212]	kg/m^2
Mass	3.6	kg
Magnetic moment	[0.8 0 0]	$A{\cdot}m^2$
Hysteresis volume	[0 0.09 0.09]	cm^3
Hc	0.96	A/m
Br	0.35	Tesla
Bs	0.74	Tesla
Duration	24	hours
Initial rates	[0.3 0.5 0.5]	deg/s

To assess whether an optimal Beta angle and latitude range pair will be adequate for SASI imaging operations, the distribution of time in good pointing must be considered. For the SASI payload to successfully image the ionosphere it must take, at minimum, four second exposures. To allow for exposure times of this length, with adequate margin, the results must show at least four instances of the spacecraft being in a good pointing attitude for over 20 seconds. With this criterion, latitude ranges 2 through 6 are deemed adequate. Figures 5.6 through 5.10 show the ground track projection of the spacecraft when it is in good pointing attitude along with the distribution of times spent in that attitude. Additionally, the full 24 hour ground track is shown in black.

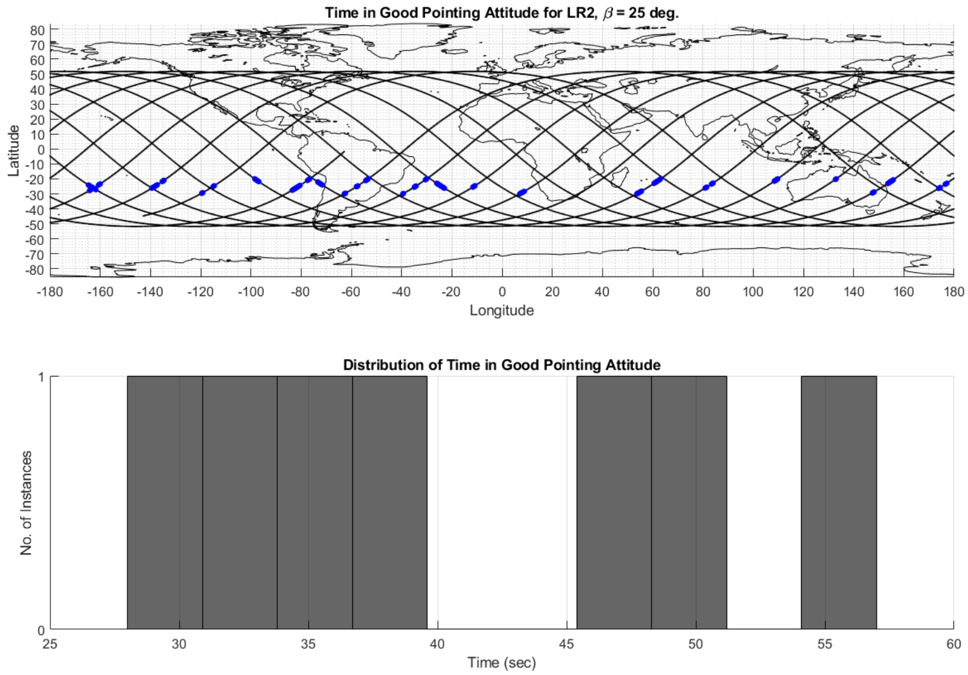

Figure 5.6: Ground track projection and distribution of time in good pointing for SASI imaging at latitude range 2, with Beta angle set to 25 degrees.

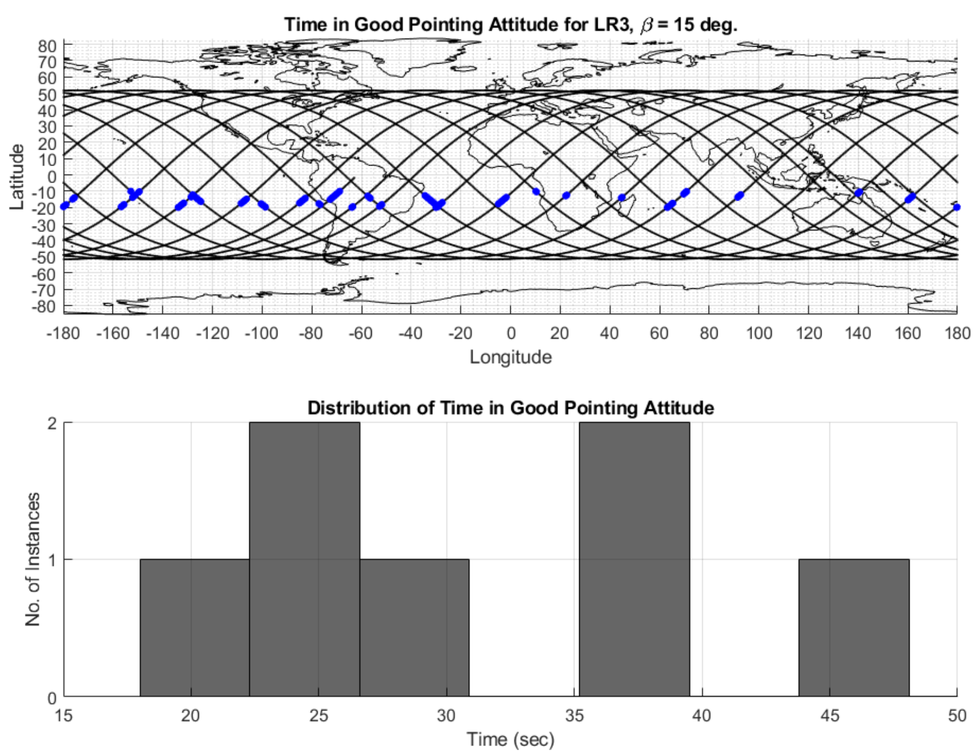

Figure 5.7: Ground track projection and distribution of time in good pointing for SASI imaging at latitude range 3, with Beta angle set to 15 degrees.

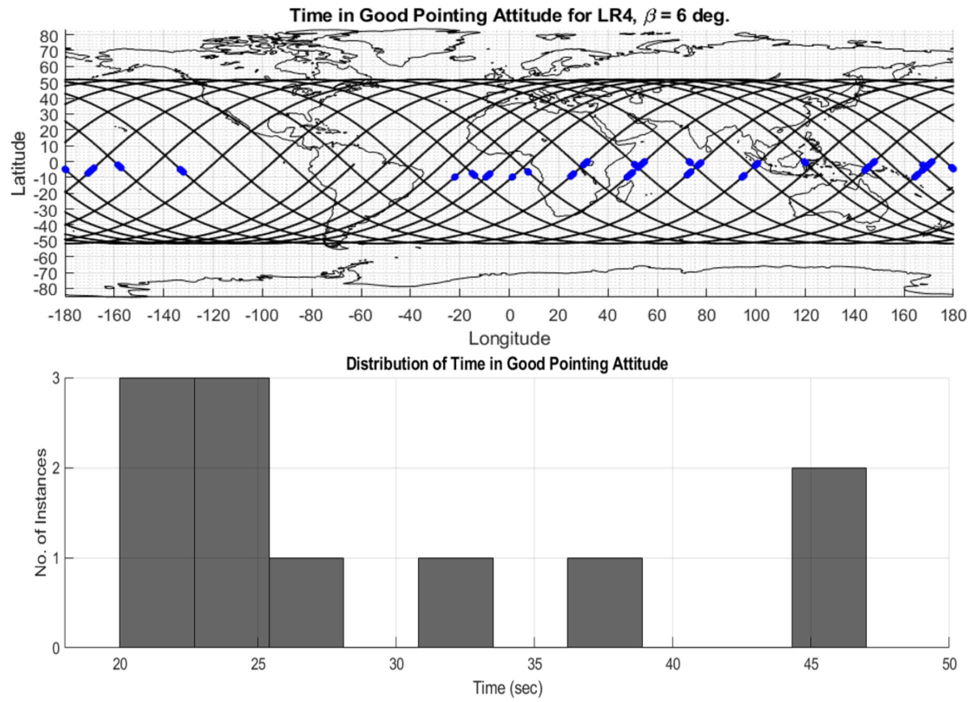

Figure 5.8: Ground track projection and distribution of time in good pointing for SASI imaging at latitude range 4, with Beta angle set to 6 degrees.

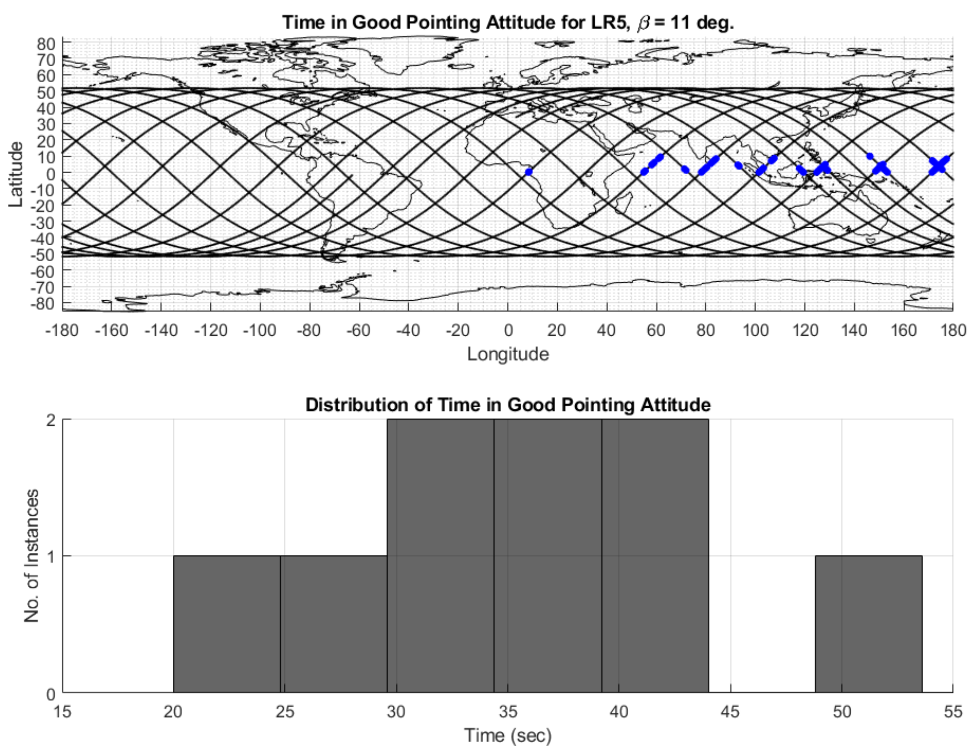

Figure 5.9: Ground track projection and distribution of time in good pointing for SASI imaging at latitude range 5, with Beta angle set to 11 degrees.

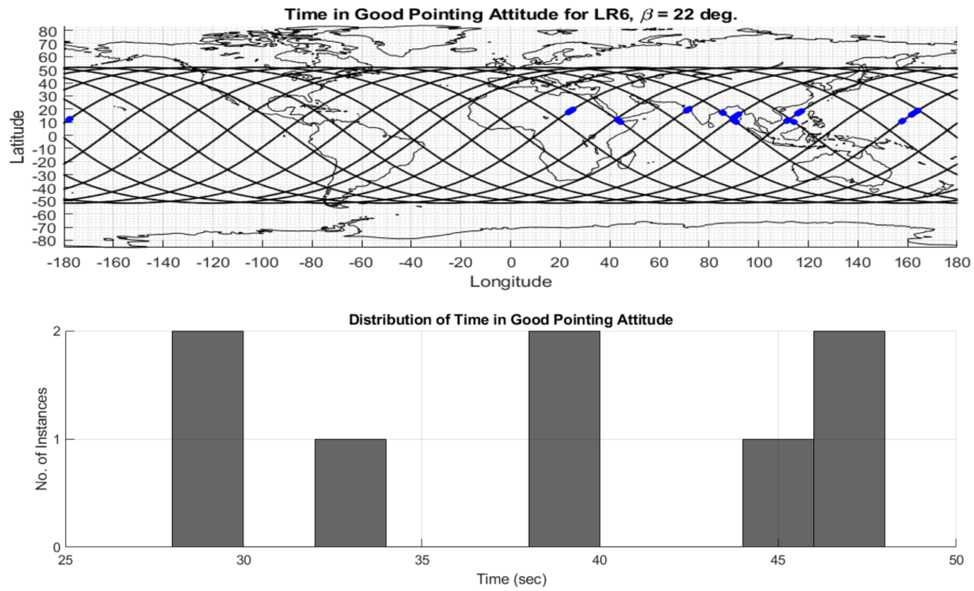

Figure 5.10: Ground track projection and distribution of time in good pointing for SASI imaging at latitude range 6, with Beta angle set to 22 degrees.

It is important to note that these simulations were conducted using the same TLE file, therefore they all begin at the same epoch. With a different TLE file, the distribution and location of times in good pointing attitude would vary due to the spacecraft moving through different locations of the Earth's magnetic field, at different times. It is expected that for a simulation spanning weeks, the ground track projection would become much more populated in the areas showing acceptable pointing. Therefore, the location and periods of time in good pointing for a specific latitude range will vary with epoch. From this analysis it can be concluded that the HMAC system will be effective for the SASI payload at latitudes ranging from -30° to +20°, with a maximum Beta angle of 25°. Additionally, over a 24 hour period, the ground track of the spacecraft will intersect the desired latitude range approximately 31 times. From this, a percentage can be found which defines the probability at which VIOLET will be in good pointing attitude. From Table 5.6 it can be seen that the probability of VIOLET being in good pointing attitude increases when it is near the equator, with a maximum found to be 35.5%.

Table 5.6: Percent Change of VIOLET Being in Good Pointing Attitude Per Orbit

Latitude	% chance per orbit
LR2	22.5%
LR3	22.5%
LR4	35.5%
LR5	29.0%
LR6	25.8%

The inclination error versus time has been plotted for latitude ranges 2 through 6 and is shown in Figure 5.11. The dashed lines represent the error tolerance of ±5°. An e_δ of zero occurs when the spacecrafts +Z axis is perfectly aligned with the imaging inclination of -12°. Therefore, the oscillations about zero occur due to the spacecraft orbiting the Earth and passing through the geomagnetic field whose vector magnitude and orientation differs greatly across latitudes. As the spacecraft reaches the specified latitude range, e_δ will fall between the error tolerance for a period of time. In Figure 5.11, for each latitude range, the error reaches the tolerance of 5° multiple time throughout the 24 hour duration. However, the curves passing through the area of acceptable error will not always equal adequate time in good pointing, as the criteria for this has been defined to be a minimum of 20 seconds.

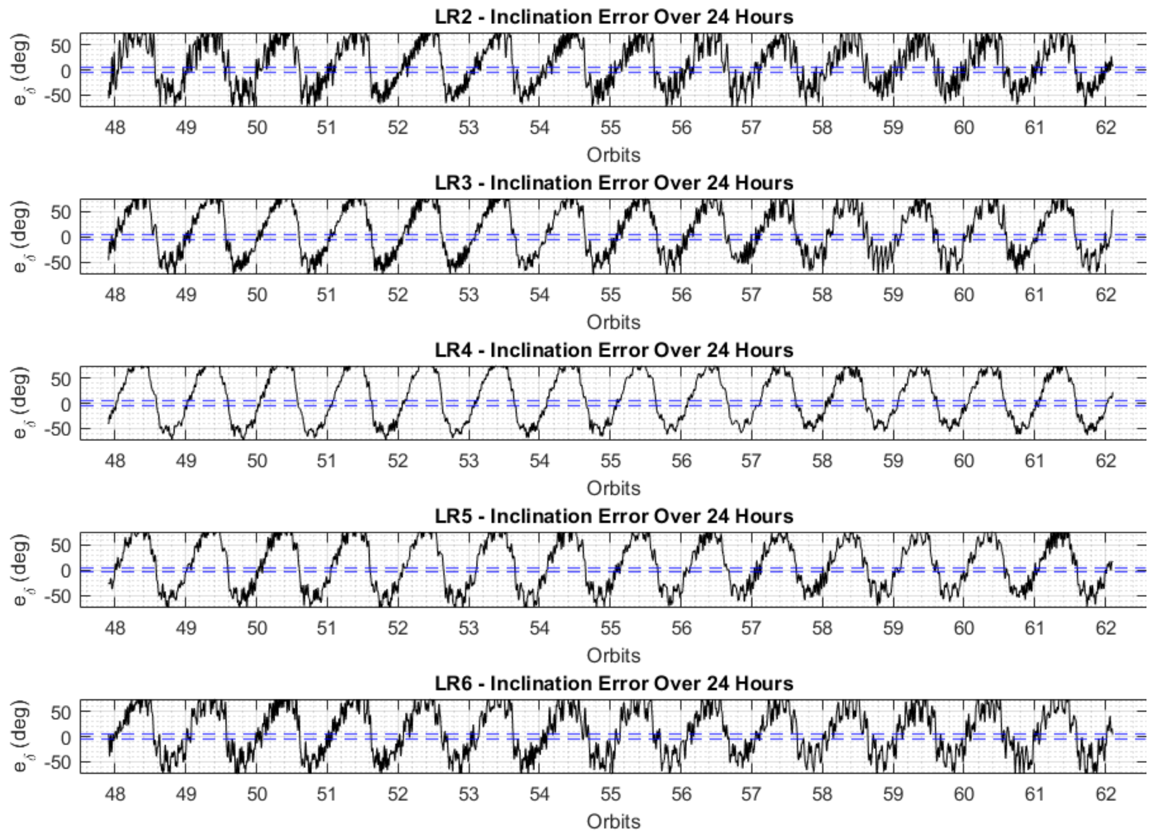

Figure 5.11: Inclination error versus time for latitude ranges 2 through 6, from day three to four (15.65 orbits).

To further characterize the effectiveness of the HMAC system at different latitude ranges, the time in good pointing of the PMAC and HMAC systems at specific ranges can be compared. The effective latitude range for SASI imaging using only PMAC is -23 to 9°. Therefore, for this comparison LR2 and LR6 need not be included due to PMAC not being capable of the required pointing error at those latitudes. Table 5.7 shows a direct comparison of TGP for PMAC and HMAC at the latitude ranges over a period of 24 hours, with only times in good pointing lasting longer than 20 seconds being considered. From the data contained in Table 5.7, it is evident that HMAC actuation yields at least double the TGP at latitude ranges compared to PMAC actuation.

Table 5.7: PMAC and HMAC Time in Good Pointing Attitude at Corresponding Latitude Ranges

Latitude	PMAC TGP (minutes)	HMAC TGP (minutes)	% Improvement
LR3	1.37	6.64	484%
LR4	1.94	5.42	279%
LR5	2.33	5.61	240%

5.2.3 System Performance Across Beta Angles

The pointing error, body-fixed axial rates, magnetic torques, and hysteresis torques have been be plotted across all Beta angles. This has been done for the purpose of investigating how the non-orthogonality between the hysteresis rods and the magnetic dipole generated by the HMAC system affect steady state performance.

Figure 5.12 shows the average body-fixed axes relative to the local GFV, for Beta angles ranging from 0 to 30°, with the vertical bars showing the standard deviation at each Beta angle. The data from each simulation was sampled from the point steady state is reached, to calculate the mean, standard deviation, maximum, and minimum values for the purpose of this analysis. Additionally, the average rates of rotation across all Beta angles is shown in Figure 5.13, with the vertical bars showing the min and max rates seen at each Beta angle.

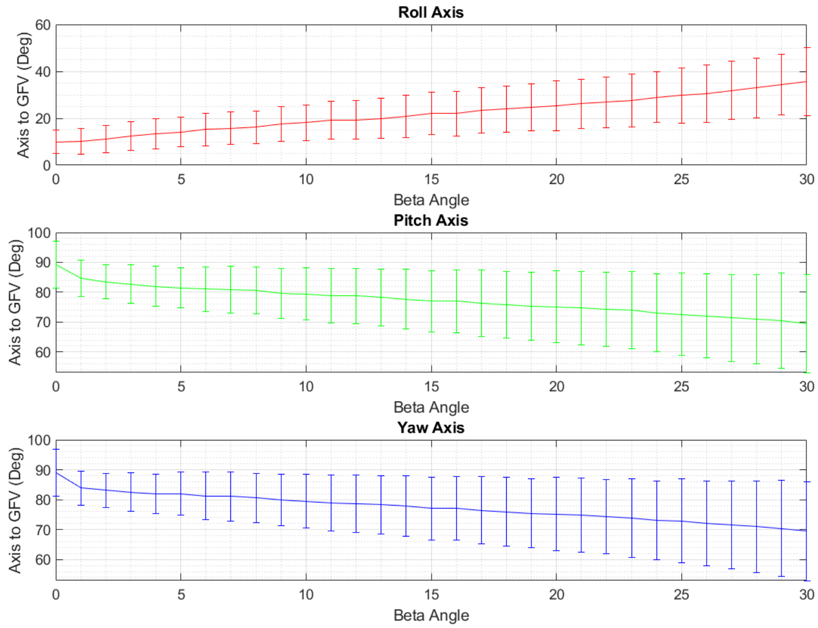

Figure 5.12: Mean and standard deviation of VIOLET body-fixed axes during steady state relative to the local geomagnetic field vector for various Beta angles.

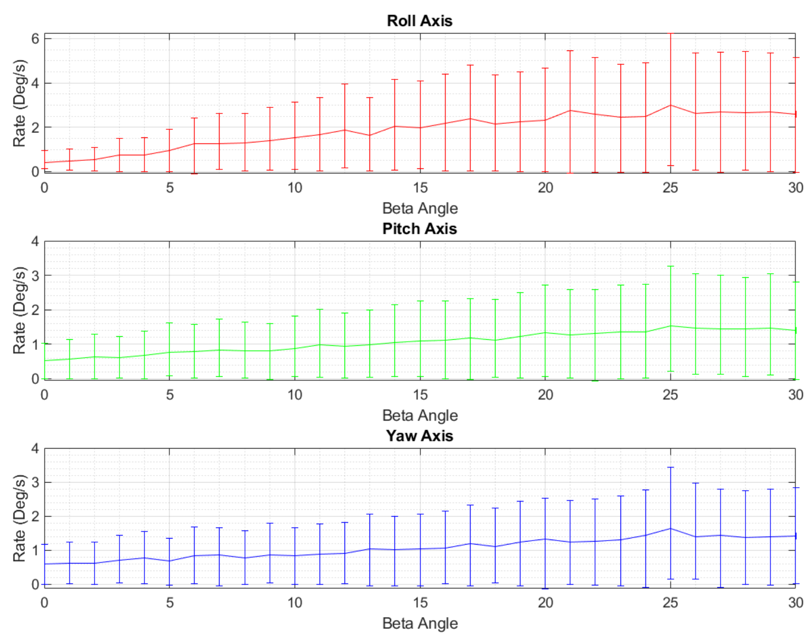

Figure 5.13: Mean of VIOLET body-fixed axial rates during steady state including minimum and maximums across various Beta angles.

As the Beta angle is increased, the angle at which the roll and primary magnetic axis is deflected from the local GFV increases. This results in more rotational potential energy, which begins to exceed the designed damping capability of the hysteresis rods. This becomes evident as the vertical bars increase in size as the Beta angle is increased. Considering Figure 5.12, there is a linear increase or decrease of the body-fixes axes relative to the local GFV, which is dependent upon $\vec{m}'$ and Beta angle. This result is expected as the HMAC vectors were calculated to accomplish this effect. Moving on to Figure 5.13, a similar reaction to an increase of the Beta angle can be seen. As the potential rotational energy is increased with Beta angle, the average rates increase, along with the minimum and maximum values, for each simulation. This result further underscores that with a larger deflection of $\vec{m}'$ from the roll axis, there will be higher rates and decreased GFV tracking accuracy. This figure shows that the rates of rotation exceed the system level requirement of 1.5 deg/s. Due to the passive foundation of the HMAC system, there is a low risk of negative mission impacts with high Beta angle actuation. Therefore, a request for deviation (RFD) can be filed to alter this requirement to enable experimental on-orbit operations of the HMAC system.

The analysis of the rotational state variables gives excellent insight into the benefits and drawbacks of the HMAC system with respect to dynamic behavior. However it is necessary to also examine the torque generated by the magnetic components in the spacecraft interacting with the Earth's magnetic field. This will give further insight into the effects on non-orthogonal hysteresis damping. Figures 5.14 and 5.15 show the average magnetic and hysteresis torque calculated for each simulation, with the vertical bars showing the standard deviation of the applied torques.

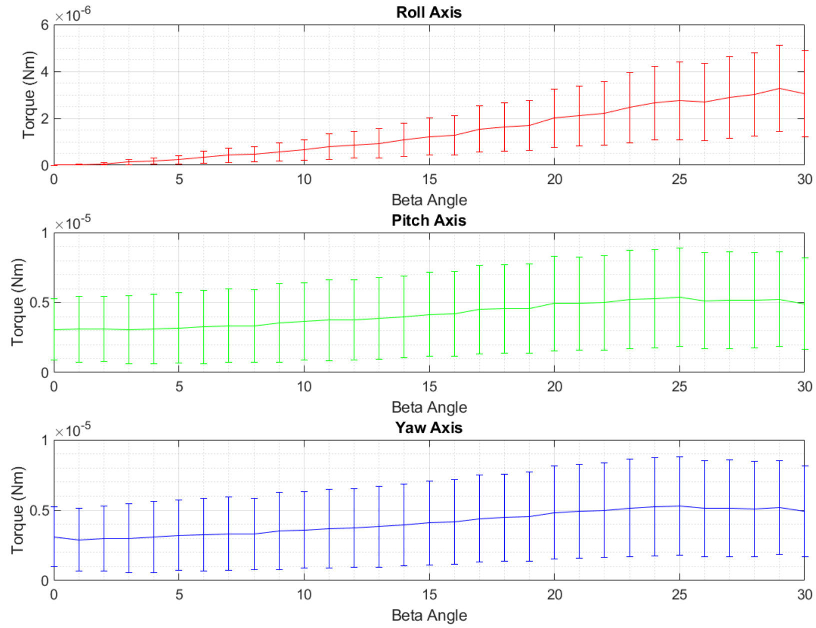

Figure 5.14: Mean and standard deviation of magnetic torques seen during steady state in VIOLET body-fixed axes for various Beta angles.

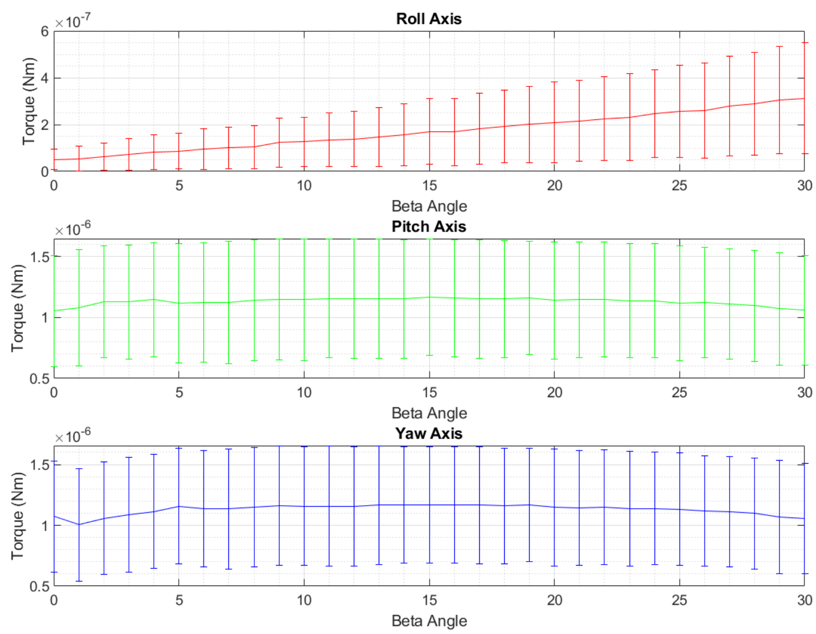

Figure 5.15: Mean and standard deviation of hysteresis torques seen in VIOLET body-fixed axes for various Beta angles.

As the Beta angle increases, so to does $\vec{m}'$. The additional magnetic flux from the torque coils, paired with the permanent magnet, increases the magnetic flux magnitude present in the spacecraft. This results in an increase of the applied torque from the permanent magnet and torque coils. Additionally, at higher Beta angles, $\vec{m}'$ becomes misaligned with the local geomagnetic field vector more frequently and at a larger magnitude, leading to higher average torques and standard deviations at each following simulation result.

Hysteresis torque generated is directly dependent on the magnetizing field being applied to the hysteresis rods as the spacecraft passes through the Earth's magnetic field. Upon inspection of Figure 5.15 it is evident that higher Beta angles do not affect the torque generated by the hysteresis rods. From the other results shown in this section it can be concluded that with higher Beta angles, the hysteresis torque remains relatively constant, however damping performance will decrease, causing higher rates of rotation and increased oscillatory error.

5.3 Summary

As part of this thesis, the ACS has been designed, simulated, and analyzed to ensure the system is compliant with requirements. The first sub-objective completed was to ensure the PMAC foundation of the HMAC system is capable of de-tumbling the spacecraft in under 7 days after deployment. It was found that the designed system will be able to de-tumble VIOLET to a mean θ_R of 10° in an average of 33.5 hours, between the three deployment conditions. Additionally it was determined that initial body-fixed rates of rotation do not affect steady state oscillatory error. The PMAC system was then analyzed during steady state to ensure there would be adequate duration and frequency at which VIOLET is in adequate attitude for SASI imaging operations. It was determined that the passive system is capable of adequate attitude within the latitude range of -9° to 23°.

The performance of the HMAC system was then analyzed for various latitude ranges with corresponding optimal Beta angles, to determine the duration and frequency at which VIOLET would be in adequate attitude for SASI imaging. It was determined that the HMAC system will be effective at latitudes from -30° to 20°. It was found that with higher Beta angles the frequency of times at which VIOLET is in adequate attitude, decreases. Additionally, the time in good pointing over a 24 hour period was compared between latitude ranges from PMAC and HMAC operations. It was found that the HMAC system yields approximately double the time in good pointing than PMAC over the same period of time.

The body-fixed axes relative to the local GFV, body-fixed axial rates, magnetic torques, and hysteresis torques have been analyzed across Beta angles to investigate the effect of Beta angle magnitude on the attitude dynamics of VIOLET. It has been found that with higher Beta angles, the steady state oscillatory error will increase, leading to less accurate GFV tracking and higher rates of rotation.

To allow VIOLET mission planners to determine when the spacecraft has attained the adequate attitude for imaging, SNAP simulations can be run and processed with up-to-date TLE files to determine real time imaging locations as well as time in good pointing. On orbit data can then be used to modify parameters in SNAP and allow for more accurate predictions. For these SNAP simulations, it will be critical to have accurate predictions of all state variables from VIOLET's ACS, specifically, $\vec{\mathbf{X}}_{ECI}$, $\dot{\vec{\mathbf{X}}}_{ECI}$, θ, and $\vec{\omega}$.

Chapter 6

Thermal Control System Analysis Results

6.1 Thermal Analysis

The VIOLET nanosatellite's thermal control system has been designed concurrently with the thermal FEA process. To passively control the temperature of sub-systems, outer surface and joint materials have been carefully selected to create heat paths throughout the spacecraft. This section will outline initial conditions and results of the WCC and WCH analyses. The following simulations are transient, using defined power states for each sub-system component over a period of 24 hours. The operation mode timings and power states per operational mode have been defined in Tables 4.4 and 4.5. To plot the temperature curves shown in Figures 6.2 to 6.10 a node was selected on each sub-system component and the data was logged. For the PCB sub-system components, the selected node was chosen in the same location where the thermal load was applied. The chosen nodes for the solar panels were selected on the area which the solar cells occupy, as they experience larger temperature ranges compared to the area covered with silver-teflon tape.

As discussed in Chapter 4, the WCC and WCH analyses require boundary conditions that reflect the goals of each case. For WCC, the spacecraft will be experiencing its coldest temperatures, with the opposite being true for WCH. The orbital parameters defining both WCC and WCH boundary conditions are shown in Figure 6.1.

Table 6.1: Orbital Parameter Inputs

Parameter	Worst Case Hot	Worst Case Cold	Units
Roll rate	1	1	deg/sec
Eccentricity	0.00128	0.00128	-
Altitude	400	250	km
Orbit inclination	51.6	51.6	deg
Orbital period	96	96	min
Orientation	North pointing	North pointing	-
Solar flux	1411.6	1323.6	W/m^2
Solar reflected (Albedo)	0.4	0.3	-
Earth IR flux	258	218	W/m^2

6.1.1 Worst Case Hot

Out of the two cases, WCH is the most critical to mission success. This is due to the communications sub-system having UVF, VHF, and S-Band capability. All of which have a significant thermal output, the sum of which can generate up to 23 W at one time. Additionally, VIOLET has two payloads, further increasing the internally generated heat loads during operations. As previously discussed, the boundary conditions and sub-system power states of the WCH analysis have been defined to achieve the highest temperatures seen during orbital operations. The power states have been selected based on the current operations schedule over a 24 hour period. The FEA model shown at the end of orbit seven can be seen in Figure 6.1, where the thermal gradients show the varying temperatures throughout the spacecraft.

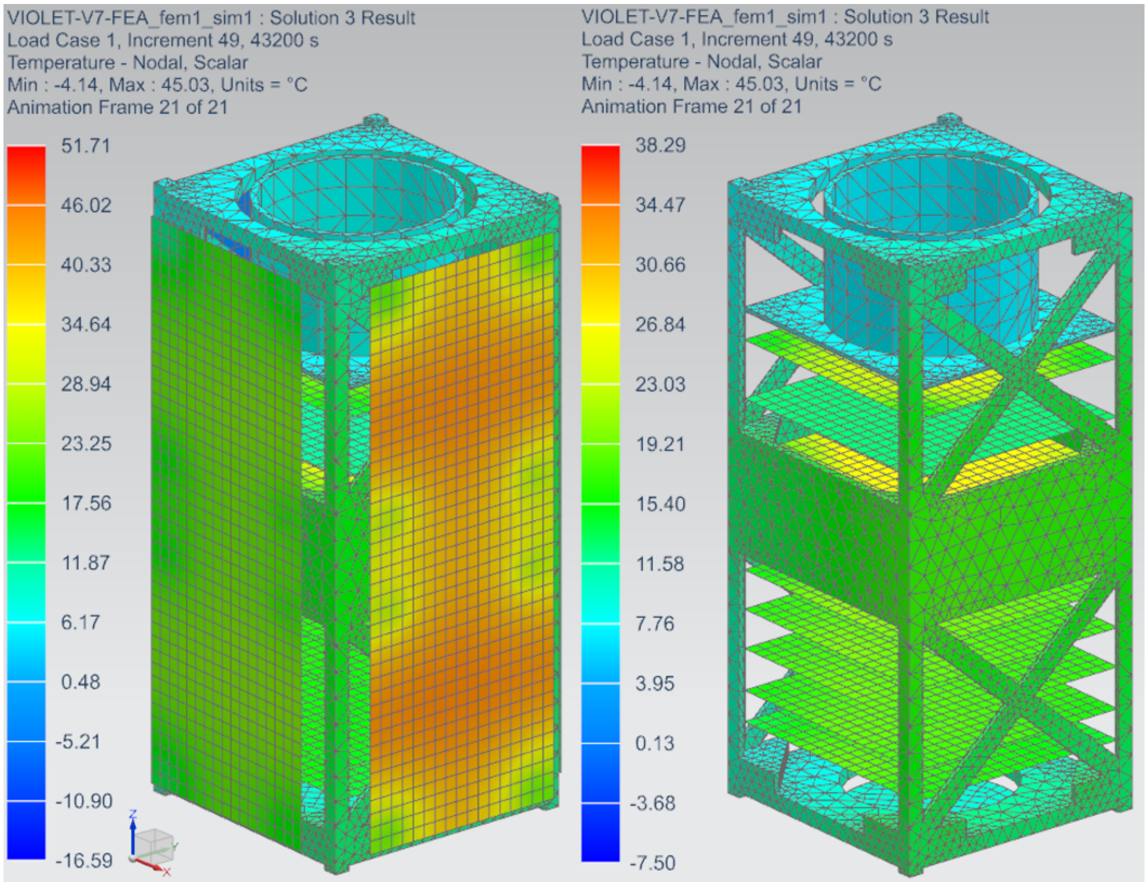

Figure 6.1: Temperature gradients seen during the WCH analysis, indexed at the end of orbit 7 with solar panels shown and hidden.

The temperature curves of the solar panels are shown in Figure 6.2. The effects of the spacecraft's rotation and north pointing attitude can be seen as the panel temperatures are not consistent with each other. At one time a panel may be facing deep space where another will be directly facing the sun, resulting in different temperatures at the same time-step. Additionally, a slight decrease in maximum temperatures occurs between five and eight orbits, which is consistent with internal power generation of the spacecraft, as the high thermal output communications modes are not active during that period. The internal temperature curves for the various sub-systems components located in the -Z module can be seen in Figure 6.3. The thermal peak seen at orbit 13 can be accounted for by the COMMS-A mode having the SCP and TRXVU active for longer periods of time as the spacecraft communicates with multiple ground stations, compared to the single ground station for COMMS-M utilizing S-Band.

The center module internal temperature predictions, included in Figure 6.4, show a temperature increase of all the components from orbit five to eight, where the spacecraft is in ADCS mode. During this mode the torque coils are fully powered for multiple orbits, along with the Electrical Power System (EPS). The units contained within the center module are 20% smaller than standard PC104 boards and have a lower resistance between them, due to their connections having half the parallel resistances compared to the -Z and +Z module PCB stacks. This results in the sub-system component temperatures being consistently matched throughout the analysis.

The internal temperature curves for the sub-system components housed in the +Z module can be seen in Figure 6.5. During WCH the battery heaters are not required and therefore the EPS, with its thermal load of 1.5 W, surpasses the battery module's temperature for the majority of the analysis. The SASI optical system includes a CMOS sensor, which performs poorly in high temperature. To mitigate over heating, the SASI-O assembly has been isolated from the rest of the +Z PCB stack by using stainless steel cylindrical standoffs, increasing the thermal resistance between it and the EPS. This is evident as SASI-O maintains a lower temperature than the EPS and batteries through the majority of the analysis.

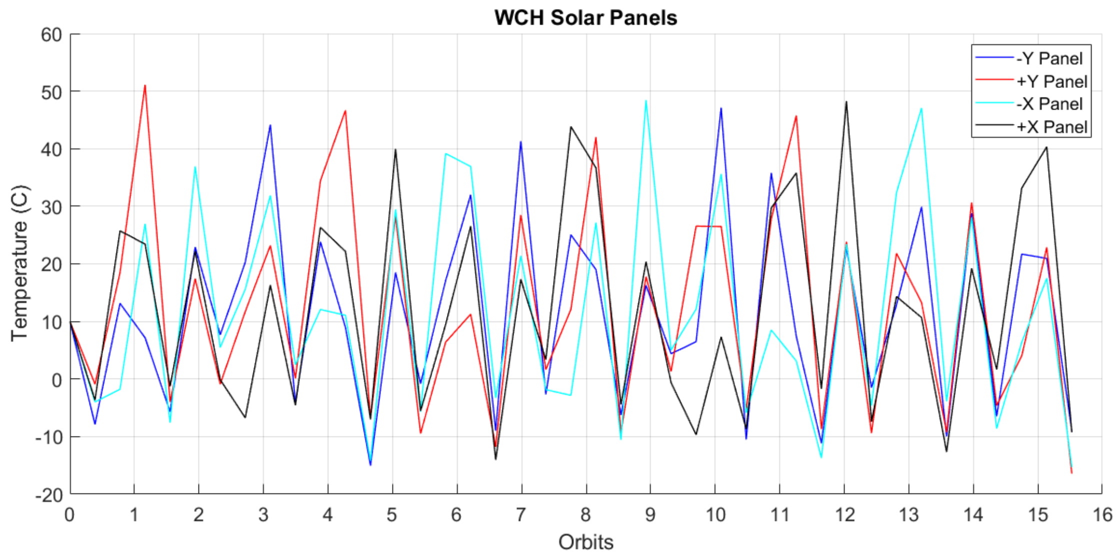

Figure 6.2: WCH temperature curves for solar panels.

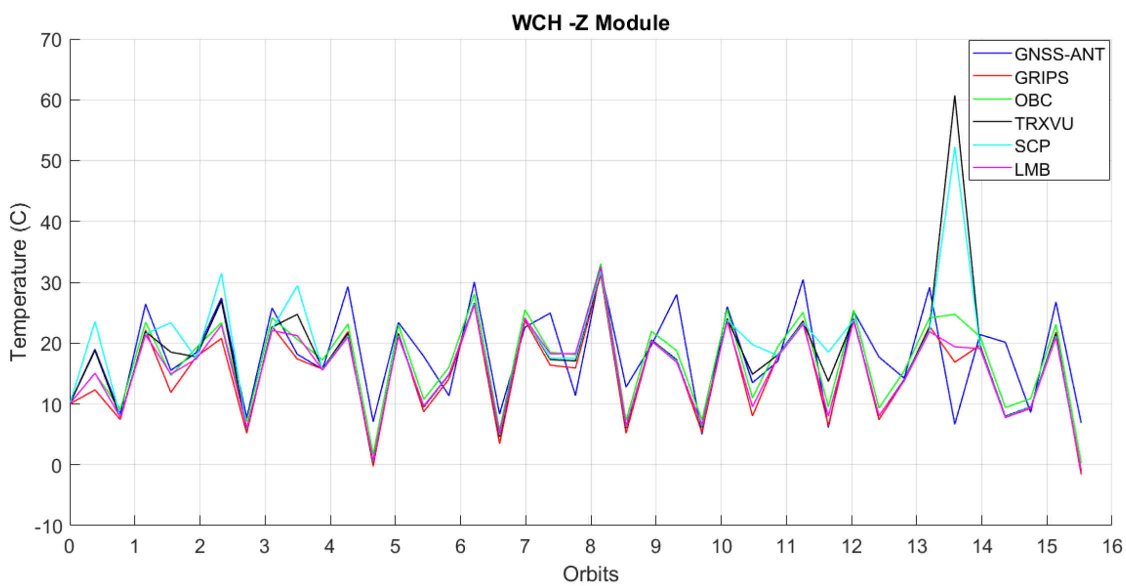

Figure 6.3: WCH temperature curves for -Z module sub-systems.

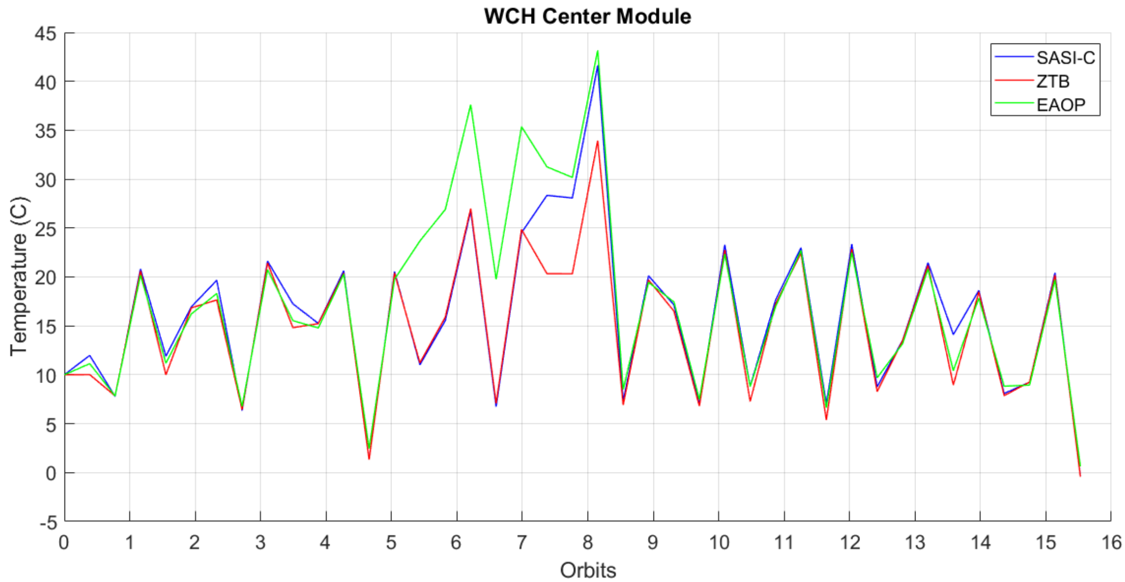

Figure 6.4: WCH temperature curves for center module sub-systems.

Figure 6.5: WCH temperature curves for +Z module sub-systems.

The minimum and maximum temperature reached for each sub-system component is shown in Table 6.2. The component of most concern for this case is the TRXVU, which showed a maximum temperature of 60.7°, only 10° less than its maximum acceptable temperature of 70°. Due to mitigative measures taken in the TCS design, as further discussed in Section 6.2, all components and sub-systems meet the temperature requirements, with at least 10% margin.

To further analyze the FEA results, the predicted WCH temperatures for the CANX-7 mission have been compared to that of VIOLET. The predicted minimum and maximum temperatures experienced within the CANX-7 were found to be -23.0°C and 58.1°, respectively [13]. Comparing the minimum and maximum predicted temperatures of -16.4°C and 60.7°C for the VIOLET FEA, it can be seen that results are adequately similar considering the two missions different orbits and physical design.

Table 6.2: Worst Case Hot Tabulated Finite Element Analysis Results and Operational Temperature Requirements

Sub-System	**Component**	**Simulated**		**Requirement**	
		Min (°C)	**Max (°C)**	**Min (°C)**	**Max (°C)**
EPS	Solar Panels	-16.4	51.1	-150	250
	iEPS Battery	7.44	22.9	0	45.0
	iEPS Main	4.23	37.2	-40.0	85.0
GRIPS	GNSS Antenna	5.01	32.0	-40.0	85.0
	GRIPS	-1.64	31.2	-40.0	85.0
OBC/ADS	OBC	-0.24	33.0	-40.0	85.0
	EAOP	-0.64	43.2	-40.0	70.0
	ZTB	-0.42	33.9	-40.0	70.0
COMMS	TRXVU	-1.05	60.7	-40.0	70.0
	SCP	-0.98	52.2	-40.0	75.0
	LMB	-0.94	32.6	-40.0	85.0
SASI	SASI-C	-0.35	41.6	-40.0	70.0
	SASI-O	-1.02	25.8	-30.0	70.0

6.1.2 Worst Case Cold

To best emulate the WCC conditions, the analysis boundary conditions have been defined such that the spacecraft sees the minimum amount of solar, IR, and albedo flux. Additionally the thermal load of all sub-systems is significantly lower, being in safe-hold mode. The sub-system component most sensitive to low temperatures is the EPS battery module, as sustained temperatures below zero can greatly reduce the capacity of energy the battery can safely discharge, as well as its operational lifetime. In contrast, the SASI optical system imaging sensor produces less noise and performs best at lower temperatures. The FEA model shown at the end of orbit seven can be seen in Figure 6.6, where the thermal gradients show the varying temperatures throughout the spacecraft.

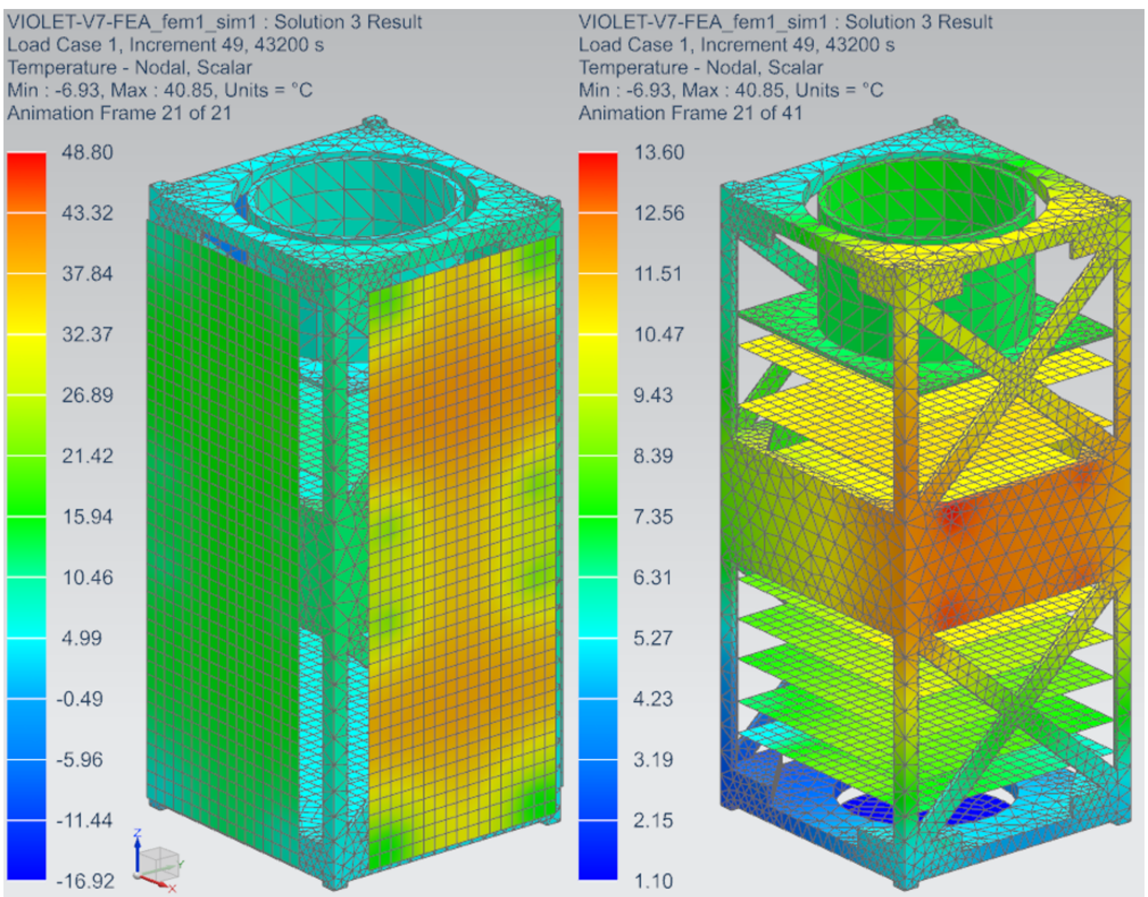

Figure 6.6: Temperature gradients seen during the WCC analysis, indexed at the end of orbit 7 with solar panels shown and hidden.

The solar panels have been designed to be the least sensitive component to temperature, as they make up the majority of the surface area which is absorbing and ejecting heat to the environment. Figure 6.7 shows the temperatures experienced by the four panels throughout the duration of the analysis. Compared to the same components in WCH, the WCC temperature predictions are shifted down approximately 5°C. With less radiative flux seen in addition to the lower internal power generation, the lower temperatures are expected.

The -Z module contains the GRIPS, COMMS and OBC sub-systems, making it the module which generates the most power across all modes of operation. Figure 6.8 shows the temperature curves for these sub-system components for the duration of the analysis. The GNSS antenna temperature curve has a higher amplitude than the other components, this is due to it having radiative interactions with the environment, as it is fastened to the -Z plate. The other components have a constant power state and have heat paths between them, deigned for minimal resistance. This results in their temperature curves being closely matches throughout the orbital heating cycles.

Similar to the WCH analysis, the center module sub-system component temperatures, shown in Figure 6.9, match closely for the duration of the analysis. This is a result of the lower relative thermal resistance between the PCB's, because they are separated by solid aluminum standoffs instead of tie-rod spacer joints seen in the -Z and +Z modules.

As previously discussed, the battery modules is very sensitive to low temperatures, and sustained operations below zero can have a strong impact on the battery performance and lifetime. Due to the initial temperature of zero degrees in addition to the 30 minute post-deployment timer the battery module temperature falls below zero for approximately 30 minutes in the first orbit. This is unavoidable due to the aforementioned initial conditions, however, it will not have a significant impact on the batteries, due to the limited time at that temperature. After the first orbit, the minimum temperature the batteries experience does not fall below 5°. In this case, the battery heater was turned on to full power (2 W) to ensure the battery temperature would remain above zero after the first orbit. The SASI optical system (SASI-O) requires low operational temperatures to take scientific quality images, creating the need for adequate thermal control of the optical system. From Figure 6.10, the SASI-O temperature curve verifies the effectiveness of material selection for thermal control as its temperature remains consistently less than other components for the duration of the analysis.

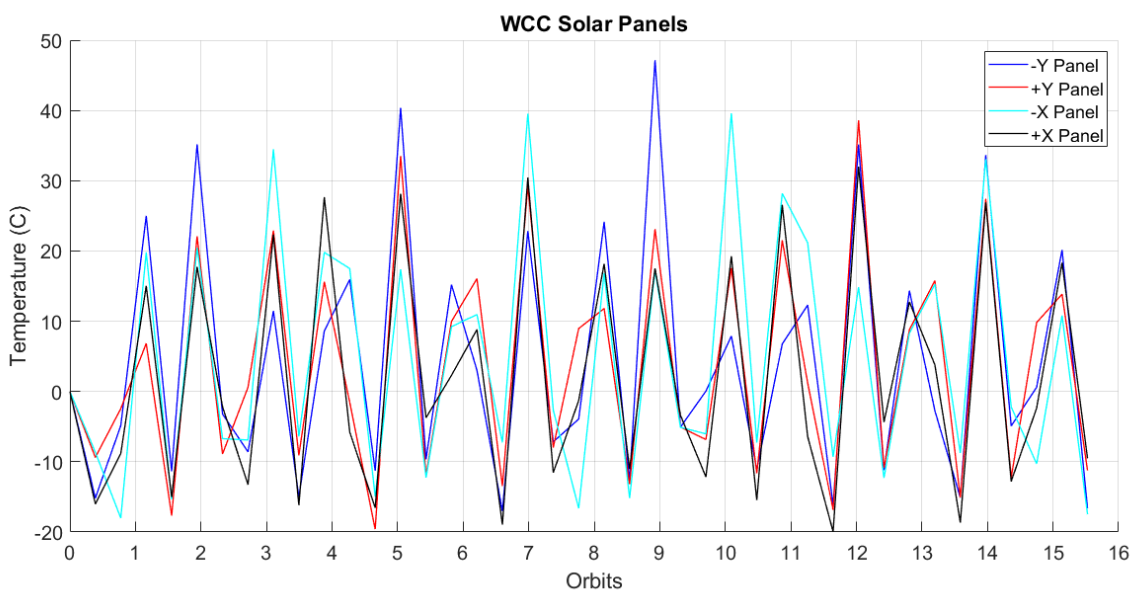

Figure 6.7: WCC temperature curves for solar panels.

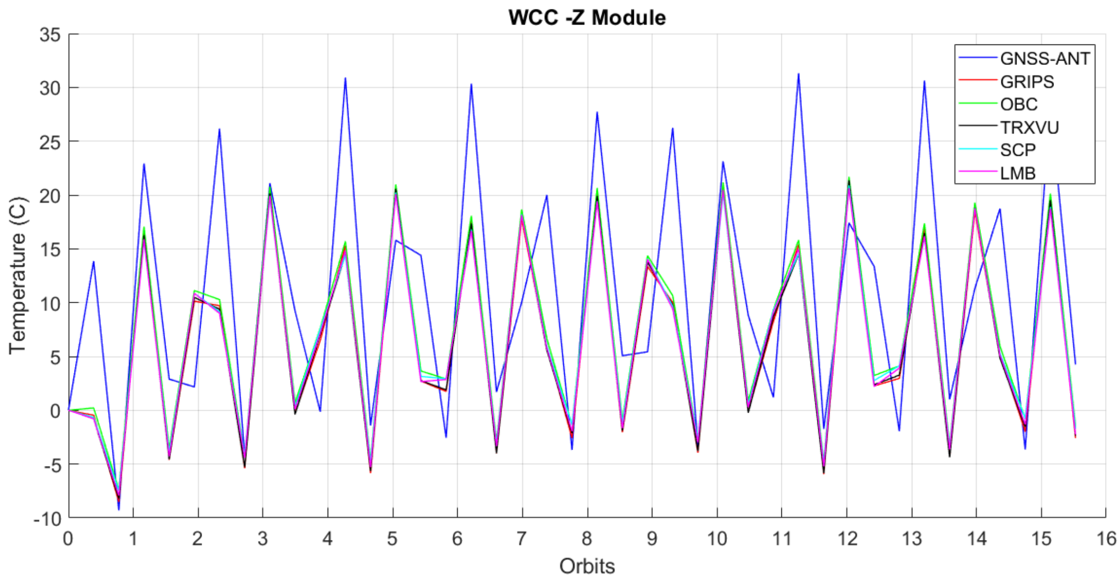

Figure 6.8: WCC temperature curves for -Z module sub-systems.

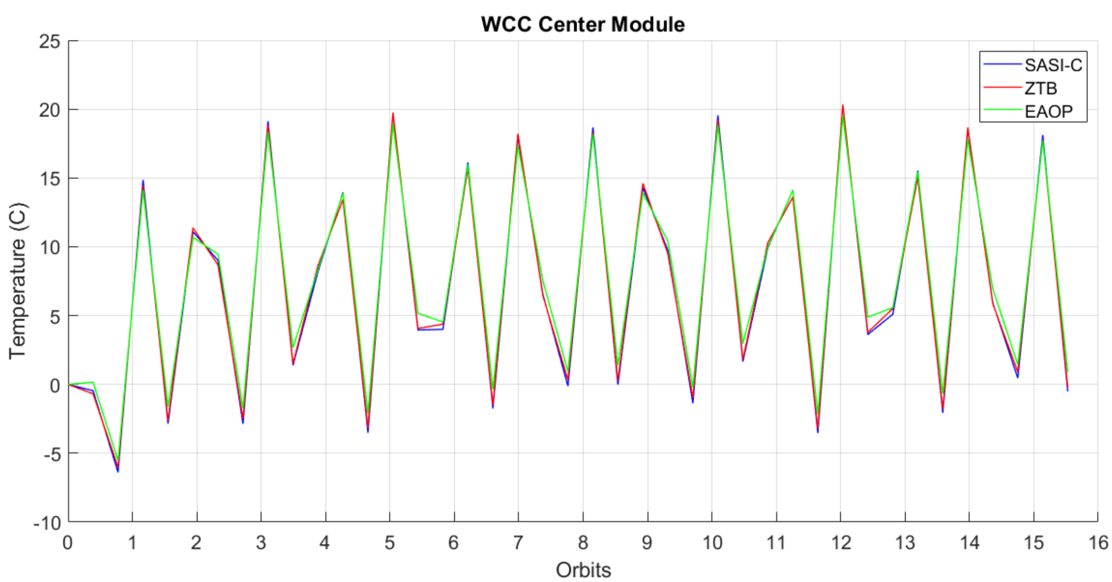

Figure 6.9: WCC temperature curves for center module sub-systems.

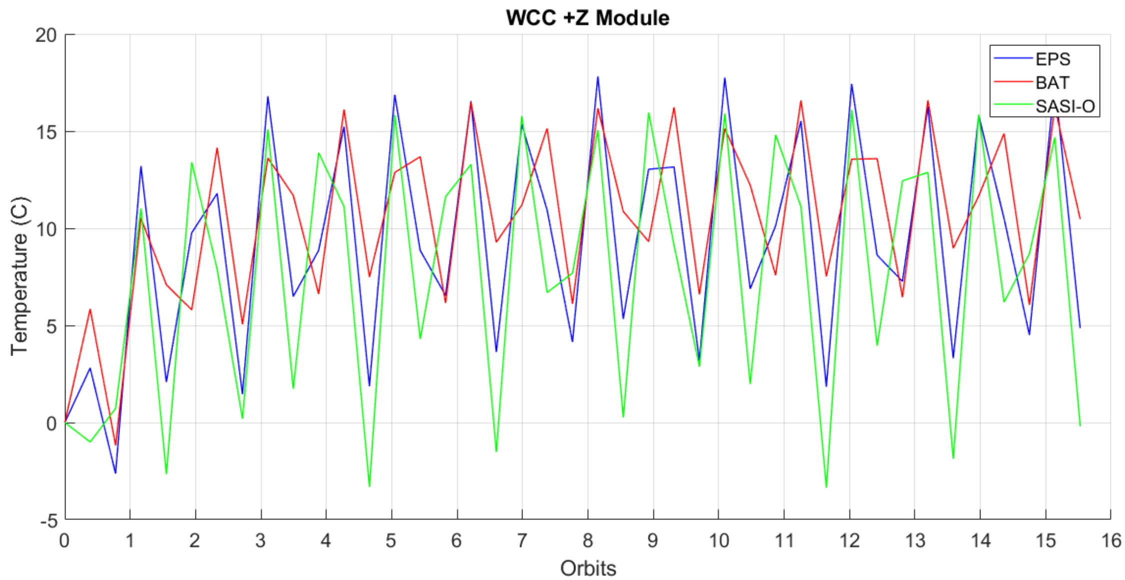

Figure 6.10: WCC temperature curves for +Z module sub-systems.

The minimum and maximum temperature reached for each sub-system component is shown in Table 6.3. Due to mitigative measures taken in the TCS design, all components and sub-systems, with the exception of the battery module meet the temperature requirements, with atleast 10% margin. As discussed, the initial temperature drop experienced by the battery module is a result of the initial conditions of the simulation, where VIOLET is deployed at a uniform temperature of zero degrees, and must wait 30 minutes before powering on. The amount of time at which the component is below zero violates its thermal requirements, however it will not have any significant impact on its energy capacity and lifetime.

To further analyze the FEA results, the predicted WCC temperatures for the CANX-7 mission have been compared to that of VIOLET. The predicted minimum and maximum temperatures experienced within the CANX-7 were found to be -29.5$^{\circ}C$ and 58.4°, respectively [13]. Comparing the minimum and maximum predicted temperatures of -20.0$^{\circ}C$ and 47.1$^{\circ}C$ for the VIOLET FEA. This comparison presents a significant difference to WCH as the CANX-7 simulated power states were defined much differently that those of VIOLET. For the CANX-7 WCC, the sub-systems are in normal operation compared to VIOLET being in safe-mode. This results in higher predicted temperatures in the CANX-7 analysis.

Table 6.3: Worst Case Cold Tabulated Finite Element Analysis Results and Operational Temperature Requirements

Sub-System	**Component**	**Simulated**		**Requirement**	
		Min (°C)	**Max (°C)**	**Min (°C)**	**Max (°C)**
EPS	Solar Panels	-20.0	47.1	-150	250
	iEPS Battery	-1.17	16.6	0	45.0
	iEPS Main	-2.63	17.8	-40.0	85.0
GRIPS	GNSS Antenna	-9.29	31.3	-40.0	85.0
	GRIPS	-8.51	21.0	-40.0	85.0
OBC/ADS	OBC	-7.37	21.7	-40.0	85.0
	EAOP	-5.54	19.5	-40.0	70.0
	ZTB	-6.02	20.3	-40.0	70.0
COMMS	TRXVU	-8.19	21.4	-40.0	60.0
	SCP	-7.46	20.9	-40.0	75.0
	LMB	-7.91	20.6	-40.0	85.0
SASI	SASI-C	-6.39	20.3	-40.0	70.0
	SASI-O	-3.35	16.1	-30.0	70.0

6.2 Thermal Control System Design

The passive TCS design was developed concurrently with the thermal analysis. This was accomplished through an iterative approach, where thermal paths throughout the spacecraft could be created to counteract where sub-systems were seen outside of their acceptable thermal ranges. A brief description of the passive mitigation measures employed and their impact is given below.

As the SASI Optical system includes an imaging sensor which requires lowest possible operating temperatures, it was isolated from the EPS by utilizing stainless steel spacers, instead of aluminum. The change of spacer material to stainless steel resulted in an equivalent resistance increase between SASI-O and EPS from 2.4 K/W to 7.2 K/W. The increased thermal resistance between SASI-O and the EPS enabled the imaging sensor to remain cooler than its surrounding sub-systems, by an average of 5° and 2.4° for WCH and WCC, respectively.

Aluminum spacers were used in the tie-rod spacer joints for the -Z module allowing adequate heat transfer from the COMMS sub-system components to the -Z face and solar panels via the center module. To ensure the LMB has an adequate thermal path to the solar panels, it was placed adjacent to center module, allowing its heat to be transferred through the center module to the solar panels and radiated to space effectively, further mitigating the risk of thermal runaway. The heat path from the LMB to the panels includes the interface between LMB and the bottom of the -Z module, where the path continues through the center module where the heat in transferred and radiated from the external surfaces of the solar panels.

The only means in which VIOLET interacts with its external environment is through thermal radiation. The materials and coatings thermo-optical properties of the external surfaces of the spacecraft have been chosen such that the spacecraft will both eject and absorb heat at a level which satisfies requirements for both WCC and WCH scenarios. Silver teflon tape was selected for use on the external surface of the solar panels to enable the surface to absorb significantly less heat. The silver teflon tape compared to the FR4 sub-strait brings the surfaces absorptivity from 0.65 to 0.15. Additionally, silver teflon tape will be used on the -Z and +Z surfaces to radiate heat effectively from the Z plates, which also act as heat sinks for both modules. The overall impact to thermal behavior is reduced maximum temperature throughout the satellite over the course of the analyses.

6.3 Summary

As part of this thesis, the Thermal Control System of the VIOLET nanosatellite was simulated and designed as a concurrent process. Analysis results showing sub-system component temperatures outside of their acceptable ranges would be examined and material selection and thermo-optical coatings were used in addition to specific placement location of components to mitigate thermal requirement violations. This process was iterated throughout TCS development, resulting in defined heat paths throughout the spacecraft, to keep components at safe operational temperatures.

As discussed in Chapter 1, VIOLET will not be undergoing TVAC testing, highlighting the importance of adequate thermal analysis. The cases in which VIOLET's TCS was simulated for includes: Worst Case Hot and Worst Case Cold. The initial conditions of both cases were defined to emulate the hottest and coldest temperatures, respectively, that the spacecraft would experience in flight.

The WCH analysis initial conditions were defined such that the solar, IR, and albedo flux would be at their maximum, leading to higher relative orbital heating. Additionally, the internal thermal loads were defined such that they best reflected a 24 hour operational schedule of VIOLET in which all modes of operation were active at-least once. The WCH results showed all sub-system components fall within their acceptable thermal ranges, within 10% margin.

The WCC inital conditions were defined such that the solar, IR, and albedo flux would be at their minimum, resulting in lower relative orbital heating. The power states for this case were less complex than the WCH analysis as the sub-system components were set to their lowest power state for the duration of the analysis (safe mode). The WCC results showed all sub-system component temperatures remaining within their acceptable thermal ranges, with the exception of the battery module. As discussed, the performance and lifetime of lithium polymer batteries decreases when exposed to sub-zero temperatures for prolonged periods of time. The 30 minute post-deployment timer coupled with the uniform initial temperature of 0° makes this thermal requirement violation unavoidable. However, as the battery temperature is only below zero for approximately 30 minutes, there will be no significant impact on battery performance and lifetime.

Chapter 7

Conclusions and Recommendations

7.1 Conclusions

The VIOLET ACS has been developed to meet mission requirements in its passive and active states. The PMAC components have been selected to ensure adequate GFV tracking and optimal hysteresis damping such that the spacecraft de-tumbles in less than seven days, over a range of possible deployment conditions. It was found that initial body-fixed rates of rotation has minimal effect on steady state oscillatory error and the predicted post deployment settling time was found to be well under seven days. It was also determined that the PMAC components allow VIOLET to be in good pointing attitude between the latitudes of -9° and 23°. The HMAC system's performance was then analyzed at the defined latitude ranges with the corresponding optimal beta angle applied. This analysis gave information on the duration and frequency where VIOLET may be in good pointing attitude for SASI imaging. The latitude range where the HMAC system yields adequate pointing was found to be from -30° to 20°, which includes latitude ranges 2 through 6. Comparing the time in good pointing for the latitude ranges which both HMAC and PMAC can attain adequate pointing, it was found that with HMAC system active, there is approximately double the time spent in good pointing attitude. The body-fixed axes relative to the local GFV, body-fixed axial rates, magnetic torques, and hysteresis torques were then analyzed across the 30 Beta angles ranging from 1° to 30°. This analysis showed that with higher Beta angles, oscillatory error will increase, resulting in less accurate GFV tracking and higher body-fixed rates of rotation.

The VIOLET TCS has been simulated and designed as a concurrent process to ensure all sub-system components do not exceed their acceptable temperature ranges during the mission. This was accomplished by simulating two cases, WCH and WCC, where the initial conditions reflect the highest and lowest temperatures VIOLET will experience in flight. Additionally, the selection of 2D and 3D element sizes was verified through a mesh sensitivity analysis for both conductive and radiative heat transfer. The component of most concern in the WCH analysis was the TRXVU, where it can be at full power for prolonged periods of time and can exceed its maximum operational temperature if not properly monitored and powered down. The WCH results showed each sub-system component remaining within their acceptable temperature ranges with at least 10% margin. The component of most concern in the WCC analysis was the battery module, as its temperature falls below zero for approximately 30 minutes. This requirement violation is unavoidable due to the uniform initial temperature of zero degrees and the 30 minute timer upon deployment. As the battery temperature falls below zero only once and for a short duration, there will be no significant impact on battery performance and lifetime. The passive thermal control system was developed concurrently with the FEA model, where heat paths were defined throughout the spacecraft by utilization of different joint materials, thermo-optical coatings and placement of components. The passive TCS design resulted in safer sub-system component temperatures for both WCH and WCC analyses.

7.2 Attitude Control System Recommendations

- For the purpose of this research, the L-shell model is sufficient to analyze the effectiveness of the ACS, however for simulations to emulate specific mission operations it is recommended that the World Magnetic Model be integrated into SNAP for more detailed results.
- To increase the ease of use for SNAP and data post processing it is recommended that the simulation process for determining the optimal Beta angle for a specified latitude range be automated further.
- To drastically increase the effectiveness of the HMAC system, it is recommended that for future deployments, a deployable boom magnetometer be included into the design. This would allow for active control of the torque coils allowing for more imaging time, at more latitudes.

7.3 Thermal Control System Recommendations

- For model updates, more detailed meshes of sub-systems, including critical surface mount components is recommended.
- The addition of harness models to the FEA would increase accuracy of the analysis, and should be considered for future revisions.
- To further verify the thermal FEA, thermal vacuum testing is highly recommended.

Bibliography

[1] CubeSat NB Team, *CubeSat NB, VIOLET Space Weather Exploration Mission*. `https://www.unb.ca/initiatives/cubesat/`: University of New Brunswick, 2019.

[2] T. Lavigne et al, “VIOLET System Requirements Document,” Tech. Rep. CCP-CNB-00210-SYS-ER-P21, CubeSat NB, 2020.

[3] D. Koks, “Using Rotations to Build Aerospace Coordinate Systems,” Tech. Rep. DSTO-TN-0640, DSTO Systems Science Laboratory, Edinburgh, 2008.

[4] D. Messmann and F. Coelho, “Magnetic Attitude Control for the MOVE-II Mission,” in *7th European Conference for Aeronautics and Aerospace Sciences*, (Milan, Italy), July, 2017.

[5] D. Gerhardt, *Small Satellite Passive Magnetic Attitude Control*. PhD thesis, Boulder, CO, 2014.

[6] D. Gerhardt, S. E. Palo, Q. Schiller, and X. L. L. Blum, “The Colorado Student Space Weather Experiment (CSSWE) On-Orbit Performance,” in *Journal of Small Satellites (JoSS)*, vol. 3, pp. 265–281, 2013.

[7] L. Blum, *Colorado Student Space Weather Experiment Webpage*. `https://lasp.colorado.edu/home/csswe/`: University of Colorado., 2016.

[8] G. Park and S. Seagraves, "A Dynamic Model of A Passive Magnetic Attitude Control System for the RAX Nano-satellite," in *AIAA Guidance, Navigation, and Control Conference*, (Toronto, ON), August, 2010.

[9] J. W. Cutler, J. C. Springmann, and S. Spangelo, "Initial Flight Assessment of the Radio Aurora Explorer," in *25th AIAA Conference on Small Satellites*, August, 2011.

[10] *MOVE II CubeSat Technology in Space*. `https://www.move2space.de/MOVE-II/`: Technical University of Munich, 2017.

[11] J. Giesselman, "Development of an Active Magnetic Attitude Determination and Control System for Picosatellites on highly inclined circular Low Earth Orbits," Master's thesis, RMIT University, Melbourne, AUS, 2014.

[12] A. Scholz, F. Konig, S. Frohlich, and J. Piepenbrock, "Flight results of the compass-1 mission," tech. rep., RMIT University, Melbourne, AUS, 2009.

[13] B. S. Cotten, "Design, analysis, implementation and testing of the thermal control, and attitude determination and control systems for the CANX-7 nanosatellite mission," Master's thesis, Toronto, ON, 2014.

[14] T. L. M. Jeans, "Design, analysis, testing, and implementation of the CANX-1 structural, thermal, and attitude control systems," Master's thesis, Toronto, ON, 2003.

[15] S. Rawashdeh, *Smart Nanosatellite Attitude Propagator (SNAP)*. `https://www.mathworks.com/matlabcentral/fileexchange/68652-SNAP`: MATLAB Simulink®, 2019.

[16] S. A. Rawashdeh, *Passive Attitude Stabilization for Small Satellites*. PhD thesis, Lexington, KY, 2010.

[17] J. R. Wertz, D. F. Everett, and J. J. Puschell, *Space Mission Engineering : The New SMAD*. Hawthorne, CA: Microcosm Press, 28th ed., 2011.

[18] M. Mohammed, A. Messerman, B. Mayhan, and K. Trauth, “Theory and practice of the hydrodynamic redesign of artificial hellbender habitat,” *Herpetological Review*, vol. 47, pp. 586–591, 12 2016.

[19] J. R. Wertz, *Spacecraft Attitude Determination and Control.* Hawthorne, CA: Microcosm Press, 1st ed., 1978.

[20] B. Cullity and C. D. G. Jr., *Introduction to Magnetic Materials.* Hoboken, NJ: Wiley-IEEE Press, 2nd ed., 2008.

[21] T. W. Flatley, “A magnetic hysteresis model,” Tech. Rep. N95-27801, Goddard Spaceflight Center, NASA, 1995.

[22] H. Schaub and J. L. Junkins, *Rigid Body Kinematics, Analytical Mechanics of Space Systems.* AIAA, 4th ed., 2018.

[23] F. Santoni and M. Zelli, *Passive Magnetic Attitude Stabilization of the Unisat-4 Microsatellite.* Acta Astronautica, 2009.

[24] M. Y. Ovchinnikov and V. I. Penkov, *Passive Magnetic Attitude Control System for the Munin Nanosatellite.* Cosmic Research, 2002.

[25] “Cubesat thermal simulation guidelines,” Tech. Rep. CCP-CSA-00098-TRA-GR-Rev-1, Canadian Space Agency, 2019.

[26] J. F. Clawson, G. T. Tsuyuki, B. J. Anderson, C. G. Justus, W. Batts, D. Ferguson, and D. G. Gilmore, *Spacecraft Thermal Control Handbook - Volume 1: Fundamental Technologies.* The Aerospace Press, 2nd ed., 2002.

[27] F. Incropera and D. DeWitt, *Fundamentals of Heat and Mass Transfer.* New York, NY: John Wiley and Sons, 4th ed., 1996.

Appendix A

Requirements

The ADCS system requirements for the VIOLET nanosatellite mission [1] are listed in the following section.

A.1 VIOLET ADCS Requirements

[R-SYS-1100] The CubeSat shall have passive magnetic attitude control (PMAC) in which the Z axis of the CubeSat will align its magnetic dipole with the local geomagnetic field vector. The attitude of the CubeSat shall be estimated to +/-12° per axis at any location in its orbit.

[R-SYS-1110] The CubeSat shall not have a precession angle greater than 10° or a precession rate greater than 2 deg/s. Once the attitude of the CubeSat reaches steady state, the CubeSat shall not have an angular rotation rate higher than 2 deg/s about its Z axis.

[R-SYS-1120] The PMAC system shall have at minimum, one permanent magnet with a minimum strength of 0.6 Am2 . The PMAC system may have a maximum of 2 permanent magnets with a total minimum strength of 0.6 Am2. The permanent magnet strength measured at 7 cm from the spacecraft shall not be greater than 3.16 Gauss.

[R-SYS-1130] The CubeSat shall have at least 1 hysteresis rod on both axes orthogonal to the Z axis (X and Y). There shall be at minimum 0.075 cm3 of hysteresis material on each axis orthogonal to the Z axis (X and Y).

[**R-SYS-1140**] The PMAC system shall yield a pointing accuracy of at least 15° relative to the earths local geomagnetic field vector.

[**R-SYS-1150**] The CubeSat shall de-tumble to stability (wx=1.5 deg/s, wy=1.5 deg/s, wz=1.5 deg/s) within 7 days post deployment from the NRCSD.

[**R-SYS-1160**] The CubeSat may have active magnetorquers on the X, Y and Z axes to point the CubeSat upto 40° with and accuraacy of +/-5° relative to the local geomagnetic field vector when imaging with the SASI payload.

[**R-SYS-1170**] The CubeSat may have 2 magnetorquers, one on the X axis and one on the Y axis. The magnetorquers shall have a maximum total power draw of 1 Watt. The magnetorquers shall each have a minimum, fully powered, magnetic moment of 0.2 Am2. The CubeSat may have attitude determination hardware for post processing and attitude control system optimization.

[**R-SYS-1180**] The ADCS shall have a built-in safe hold mode to allow for the position to be held as is while in orbit.

[**R-SYS-1190**] The total power draw of the ADCS shall be less than 2 W.

[**R-SYS-1200**] The total power draw of each individual torquer shall be less than 0.4 W.

[**R-SYS-1210**] The system shall include a design to dampen the torque and angular accelerations experienced by the CubeSat.

[**R-SYS-1220**] The ADCS shall incorporate both active and passive magnetic stabilization

[**R-SYS-1230**] Each actuator shall have a minimum magnetic moment of 0.2 Am2 each.

[**R-SYS-1240**] The north pole of the permanent magnet shall cause the -z-axis of the satellite to point to magnetic North.

[**R-SYS-1250**] The system shall use acceleration and orientation data to determine a pointing vector direction with an accuracy of ±10 degrees.

[**R-SYS-1260**] The ADCS should be capable of measuring and filtering accelerometric and gyroscopic data.

[R-SYS-1270] The ADCS micro-controller shall be capable of controlling the strength of the magnetic moment of each actuator. The settling time should be a maximum of four orbits.

[R-SYS-1280] The ADCS micro-controller shall be capable of storing a model of Earth's magnetic field. This will be used for comparison with CubeSat attitude data to determine the amount of current required through each torquer.

[R-SYS-1290] The microcontroller shall measure acceleration and orientation data every 0.5 seconds.

[R-SYS-1300] The printed circuit board shall have test points in order to facilitate testing and minimize the probing pins on devices.

[R-SYS-1310] The ADCS design shall allow for interfacing with CubeSat NB's main CAN bus.

Appendix B

Appendix B

B.1 SNAP Simulink Models

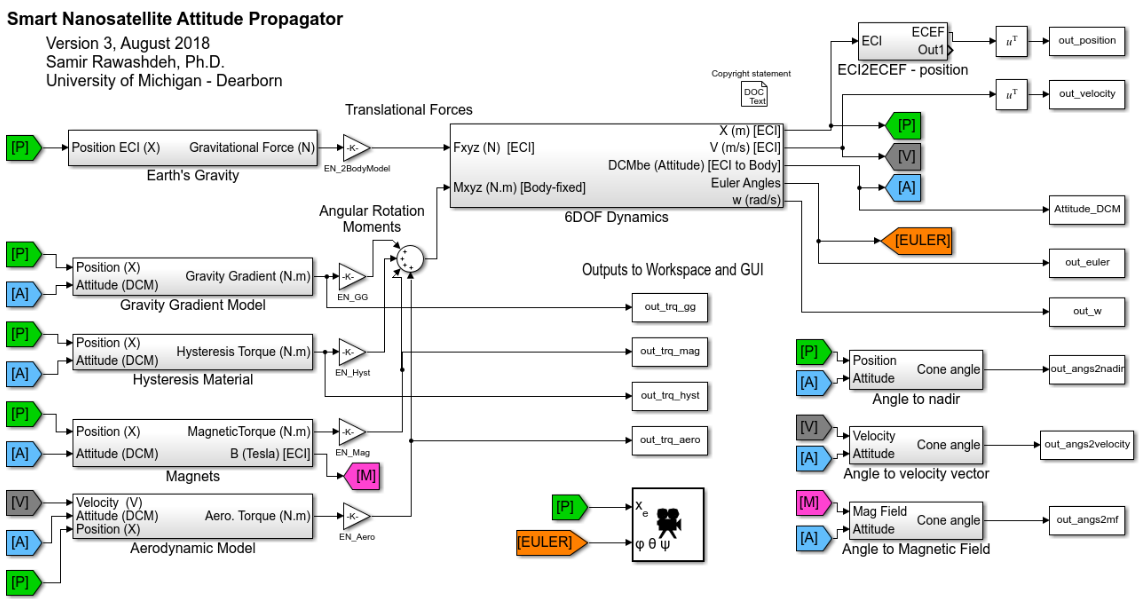

Figure B.1: SNAP Simulink main model [15].

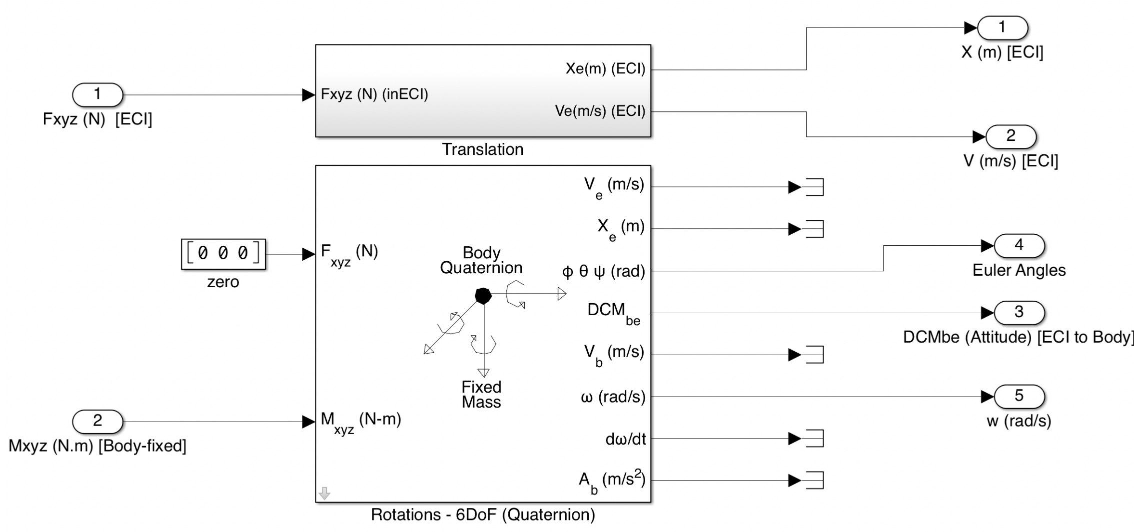

Figure B.2: SNAP Simulink 6-DoF Model [15].

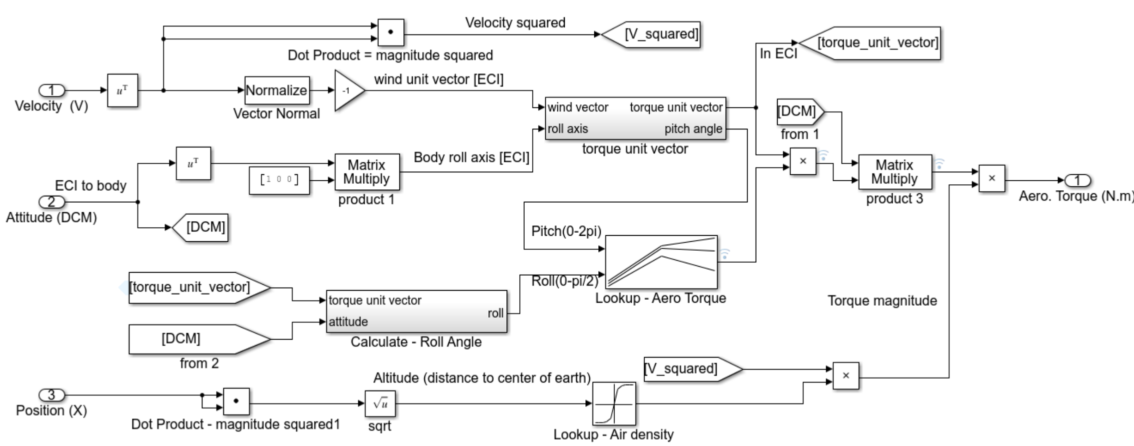

Figure B.3: SNAP Simulink aerodynamic model [15].

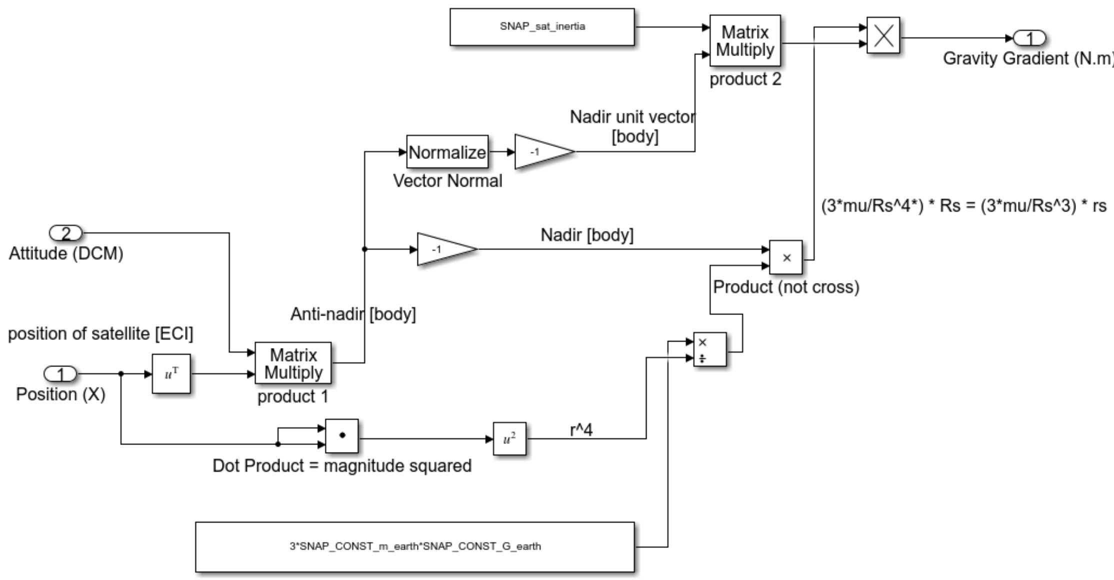

Figure B.4: SNAP Simulink gravity gradient [15].

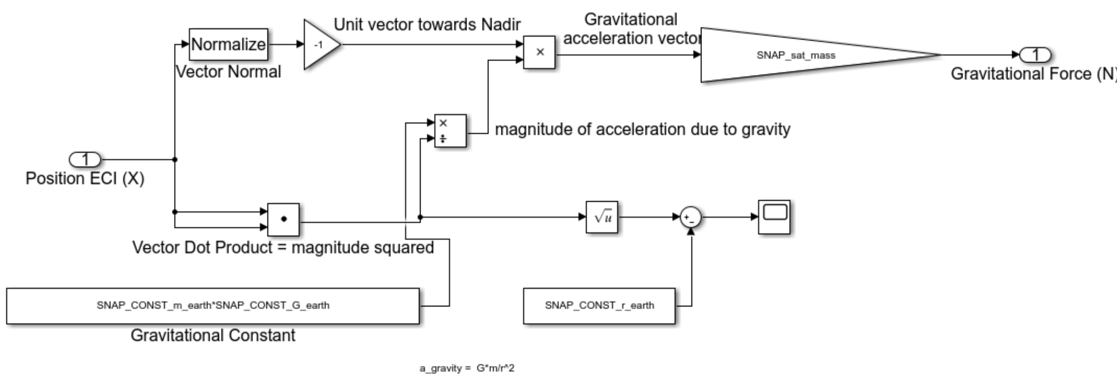

Figure B.5: SNAP Simulink 2-body gravitational force model [15].

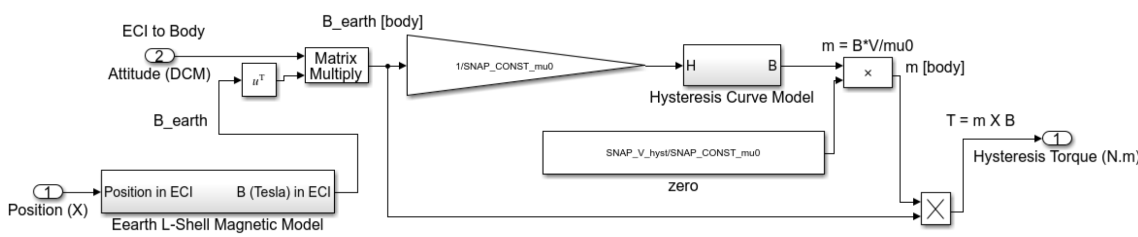

Figure B.6: SNAP Simulink hysteresis model [15].

Table B.1: Beta Angle Vectors

β (deg)	$\vec{m}\,(A\cdot m^2)$	β (deg)	$\vec{m}\,(A\cdot m^2)$
1	[0.8 0.008 0.008]	16	[0.8 0.16 0.16]
2	[0.8 0.016 0.016]	17	[0.8 0.176 0.176]
3	[0.8 0.032 0.032]	18	[0.8 0.184 0.184]
4	[0.8 0.04 0.04]	19	[0.8 0.192 0.192]
5	[0.8 0.048 0.048]	20	[0.8 0.208 0.208]
6	[0.8 0.064 0.064]	21	[0.8 0.216 0.216]
7	[0.8 0.072 0.072]	22	[0.8 0.224 0.224]
8	[0.8 0.08 0.08]	23	[0.8 0.24 0.24]
9	[0.8 0.088 0.088]	24	[0.8 0.248 0.248]
10	[0.8 0.096 0.096]	25	[0.76 0.248 0.248]
11	[0.8 0.112 0.112]	26	[0.73 0.248 0.248]
12	[0.8 0.12 0.12]	27	[0.7 0.248 0.248]
13	[0.8 0.128 0.128]	28	[0.67 0.248 0.248]
14	[0.8 0.144 0.144]	29	[0.63 0.248 0.248]
15	[0.8 0.152 0.152]	30	[0.61 0.248 0.248]

B.2 SNAP Post Processing Script

The shown MATLAB code was used to process data output from SNAP. The version shown was modified for different simulation scenarios outlined in chapter 5.

```
%%SNAP SIMULATION POST PROCESSING FOR PMAC/HMAC CASES
%Author: Alex DiTommaso
%Date: 20/04/2021

clear
clc
```

```
%%
%Load results and lla files
load('TS-HMAC-BETA29-RESULTS-01.mat') %.mat SNAP output file ...
    loading example
load('TS-HMAC-BETA29-LLA-01.mat')

%%
%%Initial Conditions for Data Processing
Lat_img = -12; %Target imaging latitude
beta = 15;
del_set = -12; %value for desired Z axis inclination based on ...
    pointing requirement for imaging location and beta angle
e = 5; %Abs of max/min inclination pointing error (for precise ...
    data formatting)
e_min = -5; %for using asymmetrical acceptable error (i.e. -6,+8)
e_max = 5;
set_min = -e; %Min allowable error
set_max = +e; %Max allowable error
% Lat_img_min = Lat_img - 50;
% Lat_img_max = Lat_img + 50;
Lat_img_min = 20;
Lat_img_max = 30;
time = sim_results.time; %seconds
t = time/3600; %hours
td = time/86400; %days
orbits = time*(1.797*10^(-4));
%%
%Array spliting
t_max_days = max(td); %max time in days of sim, used to make ...
    sure array splitting code is set up the way you want
data_size = length(t); %computing total length of data set
data_size_div2 = round(data_size/2); %used for splitting daily ...
    or hourly data
```

```
data_size_div4 = round(data_size/4);

LATS = lla(:,1); %Latitude in degrees
LONS = lla(:,2); %longitude in degrees

LATS_1 = LATS(1 : data_size_div4);
LATS_2 = LATS(data_size_div4 + 1 : data_size_div2);
LATS_3 = LATS(data_size_div2 + 1 : data_size_div2 + data_size_div4);
LATS_4 = LATS(data_size_div2 + data_size_div4 + 1 : data_size);

LONS_1 = LONS(1 : data_size_div4);
LONS_2 = LONS(data_size_div4 + 1 : data_size_div2);
LONS_3 = LONS(data_size_div2 + 1 : data_size_div2 + data_size_div4);
LONS_4 = LONS(data_size_div2 + data_size_div4 + 1 : data_size);

a2mf = sim_results.angs2mf; %Satellite axes to magnetic field ...
    vector (deg)
roll_a2mf = a2mf(:,1);

del_ex = sim_results.angs2nadir; %Z axis to Nadir
del_actual = 90-del_ex(:,1); %Z axis to tangent of Earths surface
error_del = del_actual-del_set; %instantaneous error angle ...
    between desired inclination and actual inclination

error_del_int = round(error_del);
error_del_1 = error_del(1 : data_size_div4);
error_del_2 = error_del(data_size_div4 + 1 : data_size_div2);
error_del_3 = error_del(data_size_div2 + 1 : data_size_div2 + ...
    data_size_div4);
error_del_4 = error_del(data_size_div2 + data_size_div4 + 1 : ...
    data_size);

%%
```

```
%%While loop to index acceptable pointing latitudes and error

error_del_int = round(error_del);
error_del_idx = find(error_del_int < e & error_del_int ≥ -e); ...
    %index # of all error values within +/- e

data_lat_1 = [];
data_lat_2 = [];
data_lat_3 = [];
data_lat_4 = [];
data_lon_1 = [];
data_lon_2 = [];
data_lon_3 = [];
data_lon_4 = [];
data_error_1 = [];
data_error_2 = [];
data_error_3 = [];
data_error_4 = [];
i = 1;

while i < length(error_del_idx)
    if error_del_idx(i) ≤ data_size_div4
        if ((LATS(error_del_idx(i)) ≥ Lat_img_min) && ...
                (LATS(error_del_idx(i)) ≤ Lat_img_max)) && ...
                ((error_del_int(error_del_idx(i)) ≥ -e) && ...
                (error_del_int(error_del_idx(i)) ≤ e))
            data_lat_1 = [data_lat_1, LATS(error_del_idx(i))];
            data_lon_1 = [data_lon_1, LONS(error_del_idx(i))];
            data_error_1 = [data_error_1, ...
                error_del(error_del_idx(i))];
        else
        end
    elseif error_del_idx(i) ≤ data_size_div2 && error_del_idx(i) ...
```

```
            > data_size_div4
        if ((LATS(error_del_idx(i)) ≥ Lat_img_min) && ...
            (LATS(error_del_idx(i)) ≤ Lat_img_max)) && ...
            ((error_del_int(error_del_idx(i)) ≥ -e) && ...
            (error_del_int(error_del_idx(i)) ≤ e))
            data_lat_2 = [data_lat_2, LATS(error_del_idx(i))];
            data_lon_2 = [data_lon_2, LONS(error_del_idx(i))];
            data_error_2 = [data_error_2, ...
                error_del(error_del_idx(i))];
        else
        end
    elseif error_del_idx(i) ≤ (data_size_div4 + data_size_div2) ...
            && error_del_idx(i) > data_size_div2
        if ((LATS(error_del_idx(i)) ≥ Lat_img_min) && ...
            (LATS(error_del_idx(i)) ≤ Lat_img_max)) && ...
            ((error_del_int(error_del_idx(i)) ≥ -e) && ...
            (error_del_int(error_del_idx(i)) ≤ e))
            data_lat_3 = [data_lat_3, LATS(error_del_idx(i))];
            data_lon_3 = [data_lon_3, LONS(error_del_idx(i))];
            data_error_3 = [data_error_3, ...
                error_del(error_del_idx(i))];
        else
        end
    elseif error_del_idx(i) ≤ data_size && error_del_idx(i) > ...
            (data_size_div4 + data_size_div2)
        if ((LATS(error_del_idx(i)) ≥ Lat_img_min) && ...
            (LATS(error_del_idx(i)) ≤ Lat_img_max)) && ...
            ((error_del_int(error_del_idx(i)) ≥ -e) && ...
            (error_del_int(error_del_idx(i)) ≤ e))
            data_lat_4 = [data_lat_4, LATS(error_del_idx(i))];
            data_lon_4 = [data_lon_4, LONS(error_del_idx(i))];
            data_error_4 = [data_error_4, ...
                error_del(error_del_idx(i))];
```

```
            else
            end
        end
i = i + 1;
end
accpt_pointing_day1 = round(length(data_error_1)*(1.667*10^(-3)))
accpt_pointing_day2 = round(length(data_error_2)*(1.667*10^(-3)))
accpt_pointing_day3 = round(length(data_error_3)*(1.667*10^(-3)))
accpt_pointing_day4 = round(length(data_error_4)*(1.667*10^(-3)))

LLE1 = [data_lat_1(:), data_lon_1(:), data_error_1(:)]; %LAT LON ...
    ERROR
LLE2 = [data_lat_2(:), data_lon_2(:), data_error_2(:)];
LLE3 = [data_lat_3(:), data_lon_3(:), data_error_3(:)];
LLE4 = [data_lat_4(:), data_lon_4(:), data_error_4(:)];

LLE_ALL = [LLE3;LLE2;LLE3;LLE4];
LAT_ALL = LLE_ALL(:,1);
LON_ALL = LLE_ALL(:,2);
ERR_ALL = LLE_ALL(:,3);
LLE_length = length(LLE_ALL(:,1));
%%
%Time in Good Pointing - Distribution
j = 1;
k = 1;
lat_diff = [];
count_idx = [];
count_diff = [];
LAT_sort = [];
LON_sort = [];
ERR_sort = [];

while j < LLE_length
```

```
    lat_dif = abs(LAT_ALL(j+1)) - abs(LAT_ALL(j));
    if abs(lat_dif) > 0.1
        count_idx = [count_idx, j];
        LAT_sort = [LAT_sort, LAT_ALL(j)];
        LON_sort = [LON_sort, LON_ALL(j)];
        ERR_sort = [ERR_sort, ERR_ALL(j)];
    else
    end
j = j + 1;
end

while k < length(count_idx)
    count_diff = [count_diff, count_idx(k+1) - count_idx(k)];
    k = k + 1;
end

TGP_AT_LAT_RANGE = [0.1.*count_diff,0];
LLET = [LAT_sort(:),LON_sort(:),ERR_sort(:),TGP_AT_LAT_RANGE(:)];
% LLET = [TGP_AT_LAT_RANGE(:),LAT_sort(:),LON_sort(:),ERR_sort(:)];
LLET_SORTED = sortrows(LLET);

%% Stats Calcs
roll_a2mf_ave = mean(roll_a2mf);
roll_a2mf_stdev = std(roll_a2mf);
pitch_a2mf = a2mf(:,2);
pitch_a2mf_ave = mean(pitch_a2mf);
pitch_a2mf_stdev = std(pitch_a2mf);
yaw_a2mf = a2mf(:,3);
yaw_a2mf_ave = mean(yaw_a2mf);
yaw_a2mf_stdev = std(yaw_a2mf);

Results_A2MF = [roll_a2mf_ave,pitch_a2mf_ave,yaw_a2mf_ave ; ...
    roll_a2mf_stdev,pitch_a2mf_stdev,yaw_a2mf_stdev];
```

```
rates = sim_results.w; %Axial rates (deg/s)
roll_w = rates(:,1)*(180/pi);
roll_w_ave = mean(roll_w);
roll_w_sdev = std(roll_w);
roll_w_min = abs(min(roll_w));
roll_w_max = abs(max(roll_w));
roll_w_abs_ave = (roll_w_min + roll_w_max)/2 ;

pitch_w = rates(:,2)*(180/pi);
pitch_w_ave = mean(pitch_w);
pitch_w_sdev = std(pitch_w);
pitch_w_min = abs(min(pitch_w));
pitch_w_max = abs(max(pitch_w));
pitch_w_abs_ave = (pitch_w_min + pitch_w_max)/2;

yaw_w = rates(:,3)*(180/pi);
yaw_w_ave = mean(yaw_w);
yaw_w_sdev = std(yaw_w);
yaw_w_min = abs(min(yaw_w));
yaw_w_max = abs(max(yaw_w));
yaw_w_abs_ave = (yaw_w_min + yaw_w_max)/2;

Results_RATES = [roll_w_ave,pitch_w_ave,yaw_w_ave ; ...
    roll_w_sdev,pitch_w_sdev,yaw_w_sdev ; ...
    roll_w_min,pitch_w_min,yaw_w_min ; ...
    roll_w_max,pitch_w_max,yaw_w_max ; ...
    roll_w_abs_ave,pitch_w_abs_ave,yaw_w_abs_ave];

T_mag = sim_results.trq_mag;
roll_T_mag = abs(T_mag(1,:));
roll_T_mag_ave = mean(roll_T_mag);
roll_T_mag_sdev = std(roll_T_mag);
```

```
pitch_T_mag = abs(T_mag(2,:));
pitch_T_mag_ave = mean(pitch_T_mag);
pitch_T_mag_sdev = std(pitch_T_mag);
yaw_T_mag = abs(T_mag(3,:));
yaw_T_mag_ave = mean(yaw_T_mag);
yaw_T_mag_sdev = std(yaw_T_mag);

T_hys = sim_results.trq_hyst;
roll_T_hys = abs(T_hys(1,:));
roll_T_hys_ave = mean(roll_T_hys);
roll_T_hys_sdev = std(roll_T_hys);
pitch_T_hys = abs(T_hys(2,:));
pitch_T_hys_ave = mean(pitch_T_hys);
pitch_T_hys_sdev = std(pitch_T_hys);
yaw_T_hys = abs(T_hys(3,:));
yaw_T_hys_ave = mean(yaw_T_hys);
yaw_T_hys_sdev = std(yaw_T_hys);

Results_T_MAG = [roll_T_mag_ave,pitch_T_mag_ave,yaw_T_mag_ave ; ...
    roll_T_mag_sdev,pitch_T_mag_sdev,yaw_T_mag_sdev];
Results_T_HYS = [roll_T_hys_ave,pitch_T_hys_ave,yaw_T_hys_ave ; ...
    roll_T_hys_sdev,pitch_T_hys_sdev,yaw_T_hys_sdev];

Results_excel = [roll_a2mf_ave,pitch_a2mf_ave,yaw_a2mf_ave , ...
    roll_a2mf_stdev,pitch_a2mf_stdev,yaw_a2mf_stdev , ...
    roll_w_ave,pitch_w_ave,yaw_w_ave , ...
    roll_w_sdev,pitch_w_sdev,yaw_w_sdev , ...
    roll_w_min,pitch_w_min,yaw_w_min , ...
    roll_w_max,pitch_w_max,yaw_w_max , ...
    roll_w_abs_ave,pitch_w_abs_ave,yaw_w_abs_ave , ...
    roll_T_mag_ave,pitch_T_mag_ave,yaw_T_mag_ave , ...
    roll_T_mag_sdev,pitch_T_mag_sdev,yaw_T_mag_sdev , ...
    roll_T_hys_ave,pitch_T_hys_ave,yaw_T_hys_ave , ...
```

```
    roll_T_hys_sdev,pitch_T_hys_sdev,yaw_T_hys_sdev];

%%
%ANG2MF SUBPLOTTING
figure(1)
subplot(3,1,1);
plot(orbits,roll_a2mf,'r')
%yline(roll_a2mf_CLIP_ave,'.',num2str(roll_a2mf_CLIP_ave))
%text(7.71,60,(num2str(roll_a2mf_stdev)))
grid('on')
grid minor
title('Roll Axis')
xlabel('Days')
ylabel('AXIS2MF (Deg)')
ylim([0 180])

subplot(3,1,2);
plot(orbits,pitch_a2mf,'g')
%yline(pitch_a2mf_ave,'.',num2str(pitch_a2mf_ave))
%text(7.71,100,(num2str(pitch_a2mf_stdev)))
grid('on')
grid minor
title('Pitch Axis')
xlabel('Days')
ylabel('AXIS2MF (Deg)')
ylim([0 180])

subplot(3,1,3);
plot(orbits,yaw_a2mf,'b')
%yline(yaw_a2mf_ave,'.',num2str(yaw_a2mf_ave))
%text(7.71,120,(num2str(yaw_a2mf_stdev)))
grid('on')
grid minor
```

```
title('Yaw Axis')
xlabel('Days')
ylabel('AXIS2MF (Deg)')
ylim([0 180])
%%
%RATES SUBPLOTTING
figure(2)
subplot(3,1,1);
plot(td,roll_w,'r')
%yline(roll_w_ave,'.',num2str(roll_w_ave))
grid('on')
grid minor
title('Roll Axis')
xlabel('Days')
ylabel('RATE(Deg/s)')
%ylim([-2 2])

subplot(3,1,2);
plot(td,pitch_w,'g')
%yline(pitch_w_ave,'.',num2str(pitch_w_ave))
grid('on')
grid minor
title('Pitch Axis')
xlabel('Days')
ylabel('RATE(Deg/s)')
%ylim([-2 2])

subplot(3,1,3);
plot(td,yaw_w,'b')
%yline(yaw_w_ave,'.',num2str(yaw_w_ave))
grid('on')
grid minor
title('Yaw Axis')
```

```
xlabel('Days')
ylabel('RATE(Deg/s)')
%ylim([-2 2])


%
%Imaging Locations (within acceptable error range)
figure(9)
hold on
load coastlines
geoshow(coastlat,coastlon, 'Color', 'black')
scatter(data_lon_1, data_lat_1,200, 'blue', '.');
grid on
grid minor
axis tight
title(['Day 1 - Time in Good Pointing = ...
    ',num2str(accpt_pointing_day1), ' min , +/-',num2str(e),' ...
    deg. error tolerance']);
ylabel('Latitude')
xlabel('Longitude')
xticks(-180:20:180)
yticks(-80:10:80)
hold off

figure(10)
hold on
load coastlines
geoshow(coastlat,coastlon, 'Color', 'black')
scatter(data_lon_2, data_lat_2,200, 'blue', '.');
grid on
grid minor
axis tight
title(['Day 2 - Time in Good Pointing = ...
```

```
    ',num2str(accpt_pointing_day2), ' min , +/-',num2str(e),' ...
    deg. error tolerance']);
ylabel('Latitude')
xlabel('Longitude')
xticks(-180:20:180)
yticks(-80:10:80)
hold off

figure(11)
hold on
load coastlines
geoshow(coastlat,coastlon, 'Color', 'black')
scatter(data_lon_3, data_lat_3,200, 'blue', '.');
grid on
grid minor
axis tight
title(['Day 3 - Time in Good Pointing = ...
    ',num2str(accpt_pointing_day3), ' min , +/-',num2str(e),' ...
    deg. error tolerance']);
ylabel('Latitude')
xlabel('Longitude')
xticks(-180:20:180)
yticks(-80:10:80)
hold off

figure(12)
hold on
load coastlines
geoshow(coastlat,coastlon, 'Color', 'black')
scatter(data_lon_4, data_lat_4,200, 'blue', '.');
grid on
grid minor
axis tight
```

```
title(['Day 4 - Time in Good Pointing = ...
    ',num2str(accpt_pointing_day4), ' min , +/-',num2str(e),' ...
    deg. error tolerance']);
ylabel('Latitude')
xlabel('Longitude')
xticks(-180:20:180)
yticks(-80:10:80)
hold off

figure(13)
histogram(TGP_AT_LAT_RANGE,10,'FaceColor','k')
grid on
title('Distribution of Times in Good Pointing Attitude');
ylabel('# of Instances')
xlabel('Time (sec)')
```

Curriculum Vitae

Name of Candidate: Alexander Maurice Pietro DiTommaso

University attended:

Bachelor of Science in Mechanical Engineering, Mechatronics Option
University of New Brunswick, 2019
Fredericton, New Brunswick, Canada

Master of Science in Mechanical Engineering
University of New Brunswick, 2019 - Present
Fredericton, New Brunswick, Canada

Academic Employment

- Undergraduate Teaching Assistant, Department of Mechanical Engineering, University of New Brunswick, September 2018 - May 2020. Responsibilities include: Assisting professors with course delivery, hosting tutorial sessions, and grading.

Conference Presentations

- A. DiTommaso Et al, "VIOLET, A Student CubeSat for Space Weather", 43rd Committee on Space Research Scientific Assembly, Remote format, 28 January 2021.

- A. DiTommaso, T. Jeans, B. Petersen, "Development of the Hybrid Magnetic Attitude Control System for the VIOLET Nanosatellite Mission", 72nd International Astronautical Congress, Dubai, UAE, 26 October 2021.